ADVANCEMENT OF SATELLITE-BASED RAINFALL APPLICATIONS FOR BASIN-SCALE HYDROLOGIC MODELING

A THESIS SUBMITTED TO
THE GRADUATE SCHOOL OF NATURAL AND APPLIED SCIENCES
OF
MIDDLE EAST TECHNICAL UNIVERSITY

BY

YAĞMUR DERİN

IN PARTIAL FULFILLMENT OF THE REQUIREMENTS
FOR
THE DEGREE OF MASTER OF SCIENCE
IN
GEOLOGICAL ENGINEERING

JUNE 2014

Approval of the thesis:

ADVANCEMENT OF SATELLITE-BASED RAINFALL APPLICATIONS FOR BASIN-SCALE HYDROLOGIC MODELING

submitted by **YAĞMUR DERİN** in partial fulfillment of the requirements for the degree of **Master of Science in Geological Engineering Department, Middle East Technical University** by,

Prof. Dr. Canan Özgen _____
Dean, Graduate School of **Natural and Applied Sciences**

Prof. Dr. Erdin Bozkurt _____
Head of Department, **Geological Engineering Dept., METU**

Assist. Prof. Dr. Koray Kamil Yilmaz _____
Supervisor, **Geological Engineering Dept., METU**

Examining Committee Members:

Prof. Dr. Sevda Zuhal Akyürek _____
Civil Engineering Dept., METU

Prof. Dr. Hasan Yazıcıgil _____
Geological Engineering Dept., METU

Prof. Dr. Mehmet Lütfi Süzen _____
Geological Engineering Dept., METU

Assoc. Prof. Dr. İsmail Yücel _____
Civil Engineering Dept., METU

Assist. Prof. Dr. Koray Kamil Yılmaz _____
Geological Engineering Dept., METU

Date: 09.06.2014

I hereby declare that all information in this document has been obtained and presented in accordance with academic rules and ethical conduct. I also declare that, as required by these rules and conduct, I have fully cited and referenced all material and results that are not original to this work.

Name, Last Name: YAĞMUR DERİN

Signature :

ABSTRACT

ADVANCEMENT OF SATELLITE-BASED RAINFALL APPLICATIONS FOR BASIN-SCALE HYDROLOGIC MODELING

Derin, Yağmur
M. Sc., Department of Geological Engineering
Supervisor: Assist. Prof. Dr. Koray K. Yilmaz

June 2014, 181 pages

Accuracy and reliability of hydrological modeling studies heavily depends on quality and availability of precipitation estimates. However hydrological studies in developing countries, especially over complex topography, are limited due to unavailability and scarcity of ground-based networks. This study evaluates three different satellite-based rainfall retrieval algorithms namely, Tropical Rainfall Measuring Mission Multi-satellite Precipitation Analysis (TMPA), NOAA/Climate Prediction Center Morphing Method (CMORPH) and EUMETSAT's Multi-Sensor Precipitation Estimate (MPE) over topographically complex Western Black Sea Basin in Turkey, using a relatively dense rain gauge network. The results indicated that satellite-based rainfall products significantly underestimated the rainfall in regions characterized by orographic rainfall and overestimated the rainfall in the drier regions with seasonal dependency. Further, a

new bias adjustment algorithm has been devised for the satellite-based rainfall products based on the “physiographic similarity” concept. The results showed that proposed bias adjustment algorithm is better suited to regions with complex topography and provided improved results compared to the baseline “inverse distance weighting” method. To evaluate the utility of satellite-based products in hydrologic modeling studies, the MIKE SHE-MIKE 11 integrated fully distributed physically based hydrological model was implemented in the Araç Basin and driven by ground-based and satellite-based precipitation estimates. Model calibration was performed by a constrained calibration approach that is guided by multiple “signature measures” to estimate model parameters in a hydrologically meaningful way rather than using the traditional “statistical” objective functions that largely mask valuable hydrologic information during calibration process. Diagnostic evaluation has the potential to provide a consistent estimates of the parameters of watershed models.

Keywords: Satellite-based rainfall algorithms, bias adjustment, MIKE SHE-MIKE 11, calibration, diagnostic evaluation

ÖZ

UYDU-TABANLI YAĞIŞ ÖLÇÜMLERİNİN HAVZA ÖLÇEKLİ HİDROLOJİK MODELLEMELERDEKİ GELİŞİMİ

Derin, Yağmur
Yüksek Lisans, Jeoloji Mühendisliği
Tez Yöneticisi: Dr. Koray K. Yilmaz

Haziran, 2014, 181 sayfa

Hidrolojik modelleme çalışmalarının kesinlik ve güvenilirlikleri büyük ölçüde yağışın alansal ve zamansal dağılımının güvenilir şekilde ölçümüne dayanır. Yağış ölçerlerin yeterli sayıda veya hiç bulunmaması nedeniyle gelişmekte olan ülkelerde özellikle karmaşık topoğrafya üzerinde yapılan çalışmalar kısıtlıdır. Bu çalışmada üç farklı uydu tabanlı yağış tahmin algoritması, Tropical Rainfall Measuring Mission Multi-satellite Precipitation Analysis (TMPA), NOAA/Climate Prediction Center Morphing Method (CMORPH) ve EUMETSAT's Multi-Sensor Precipitation Estimate (MPE), topoğrafik olarak karmaşık özellik gösteren Batı Karadeniz Havzası, Türkiye üzerinde sık bir yağış ölçer ağı ile değerlendirilmektedir. Çalışmanın sonuçlarına göre, uydu tabanlı yağış

ürünleri, orografik yağışa sahip bölgelerdeki yağışı olduğundan az, iç kısımlardaki kurak bölgelerde ise olduğundan fazla göstermekle birlikte mevsimsel olarak da farklılıklar göstermektedir. Ayrıca, uydu tabanlı yağış algoritmaları için "coğrafi benzerlik" prensibine dayalı bir hata düzeltme algoritması önerilmektedir. Çalışmanın sonuçlarına göre, önerilen hata düzeltme algoritması topoğrafik olarak karmaşık özellik gösteren çalışma alanları için uygunluk göstermektedir ve uzaklık-bazlı algoritmalara kıyasla daha iyi performans sergilemektedir. Uydu tabanlı yağışların hidrolojik modellemelerdeki performansını ölçmek amacıyla Araç Havzası'nda fiziksel bütünleşik bir hidrolojik model olan MIKE SHE-MIKE 11 hem yağış ölçerler hemde uydu tabanlı yağış algoritmaları ile çalıştırılmıştır. Model kalibrasyon/değerlendirmesi, istatistiksel fonksiyonlar yerine hidrolojik anlamı olan özet fonksiyonlar kullanılarak daraltma kalibrasyon yöntemi ile gerçekleştirilmiştir. Havza modelleme çalışmalarında daraltma kalibrasyon yönteminin kavramsal olarak uyumlu parametre değerleri tahmin edebilmektedir.

Anahtar Kelimeler: Uydu tabanlı yağış algoritmaları, hata düzeltme, MIKE SHE-MIKE 11, kalibrasyon, tanılayıcı değerlendirme

To My Beloved Parents

"Life is an unfoldment, and the further we travel the more truth we can comprehend. To understand the things that are at our door is the best preparation for understanding those that lie beyond."

Hypatia of Alexandria

ACKNOWLEDGMENTS

"It is good to have an end to journey toward, but it is the journey that matters in the end."

Ursula K. Le Guin

I would like to express my gratitude to my supervisor Dr. Koray K. Yilmaz for his guidance, advice, criticism and most importantly his patience. He has shown great patience, kindness and with his excellent motivation I was able to complete my research. I cannot thank enough for what he provide to me and guide me the way to the academia.

I would like to thank Prof. Dr. Hasan Yazıcıgil for providing a place to conduct my studies and treating me like one of his graduate students. His pleasant attitude and willingness to help and contribute at all times of need has provided me the support throughout my research. I also like to express my gratitude to Prof Dr. Lütfi Süzen in any occasion he was always ready to help without question. Last but not least I would like to thank Dr. İsmail Yücel and Dr. Kaan Sayıt for their support.

My gratitude also goes to 7th European Community Framework Programme because this research is supported by a Marie Curie International Reintegration Grant (Project No: 277183, FLOODSAT). I am grateful for the provided opportunity that enabled me to engage in research and attend to international conferences every year of my master degree. It is very good opportunity and I would like to thank European Union for providing such opportunity.

I would also like to thank to the Turkish State Meteorological Service and General Directorate of State Hydraulic Works for providing meteorological and flow datasets for the research.

Much appreciation is expressed to my colleagues at the hydrogeology laboratory, Çidem Argunhan, Cansu Kahraman, Burcu Ünsal, Egemen Fırat, Onursal Çatak and especially

to my dearest friend Ayse Peksezer Sayit. I couldn’t survive the last year without your support and our long chats. Thank you so much for your encouragements.

My deepest gratitude to my dearest friend Kutlu Kutluer who was always there to support me. His perspective to academia and art inspired me in many ways. We have an endless list to do and limited time, hope to accomplish them as soon as possible.

I would also like to thank my dear friends Burak Parlaktuna and A. Merve Turanli, I will miss our lunch times. Thank you two for your support and encouragements.

I am deeply grateful and thankful to my loving family. I would like to thank my mother Nejla Derin, my father Bayram Derin and my troublesome brother Emre Derin for their never-ending support and love. Thank you for enduring all the harsh moments and enjoying happy moments together during this period, without your support this could not be achieved.

Finally I would like to thank my old friends whom I grow up with and parted away.

TABLE OF CONTENTS

LIST OF TABLES

TABLES

LIST OF FIGURES

FIGURES

CHAPTER 1

INTRODUCTION

1.1. Purpose and Scope

Water is fundamental to all known forms of life on Earth as well as many activities such as agriculture, industry, power generation, transportation and waste management. Hence protection of its quality and quantity is critical for the sustainable development of any society. Water on Earth cycle continually between land, sea and air. Changes in the cycling of water could have significant impacts on environment and society. The changes in climate are expected to severely affect hydrologic cycle which in return can be observed as extreme weather conditions, for example, scarcity of water resulting drought and excess of water resulting flood.

Floods are one of the most devastating and frequent natural disaster giving to the significant loss of lives and property each year. According to the IFNet Action Report (2006) number of people affected by floods has been rising rapidly not only due to extreme weather conditions but also increasing unplanned urbanization. In Western Black Sea Basin of Turkey situation is the same if not worse. Due to lack of suitable construction sites at hilly formations and political constraints, settlements are located on floodplains (Yanmaz and Usul, 1999). One of the most effective way to minimize this loss of life and property is flood early warning systems.

To understand and manage water systems under the changing climate and meet the increasing demand for water, quantitative understanding of the hydrological cycle is important which has two important aspect. Firstly processes elaborated in hydrological

cycle cannot be separated, for example surface water and groundwater are integrated and should be modeled together. Secondly understanding of the physics of the hydrological processes which controls the catchment response should be represented by physically based equations. Therefore integrated physically based distributed hydrological models can represent hydrological cycle thoroughly and can be applied to any kind of hydrological problem. Physically based hydrological models requires detailed input data which can be provided by remote sensing data and application of Geographical Information Systems to some extent. The application of remote sensing and GIS to hydrological models facilitates hydrologists to study large scale, complex and spatially distributed hydrological processes.

The accuracy and reliability of any hydrologic study whether related to flood forecasting, drought monitoring, water resources management or climate change impact assessment depend heavily on the availability of good quality precipitation estimates. Rain gauges provide direct physical measurement of the surface precipitation, however they are susceptible to certain errors arising from location, spatial scale (point), wind, mechanical errors and density (Groisman and Legates 1994). Especially in remote parts of the world and in developing countries ground-based precipitation measurements, such as rain gauge and radar networks, are either sparse or non-existent mainly due to high cost of establishing and maintaining the infrastructure. This situation is further exacerbated in regions with complex topography, where precipitation is characterized by high spatio-temporal variability. In these regions, rain gauges are generally located in lowland due to accessibility considerations, thus under-representing the precipitation occurring in highland. Satellite-based precipitation (SBP) products are perhaps the only source to fill this important gap.

Recent improvements in SBP retrieval algorithms enabled representation of high space-time variability of precipitation field with quasi-global coverage which make them potentially attractive for hydrologic modeling studies in data sparse regions. Even though satellite-based rainfall measurements are quasi global and high resolution, these products has limitations that necessitates a bias adjustment or merging procedure using more accurate rainfall products.

Analysis of satellite-based precipitation products in flood simulation is an important step to investigate whether these products are potentially attractive for hydrological modeling or not. Distributed physically based hydrological models has many parameters therefore calibration procedure has to be completed carefully. Automated model calibration/evaluation procedures rely on a single statistical measure (e.g. RMSE) often lead to ill-posed parameter values due to projection of the high dimension of the data set down to single dimension of the residual-based summary statistics. Statistical metrics only measure the (weighted) distance between observed and simulated runoff and fail to incorporate diagnostic information regarding to causes of poor model performance. In addition to classical single objective calibration, model evaluation is also conducted by diagnostic approach since it uses hydrological context and theory while defining the watershed model inadequacies. Aforementioned hydrological context is derivation of hydrologically-relevant summary metrics and/or signature patterns in the observed/simulated data derived, for example, from flow duration curve (FDC). FDC summarizes catchments ability to produce discharge values of different magnitudes, and is therefore strongly sensitive to the vertical distribution of soil moisture within a basin.

The primary objective of this study is to advance the utility of satellite-based rainfall estimates for hydrologic modeling over Araç Basin, a sub-basin of Filyos Basin, in the West Black Sea catchment of Turkey, which is characterized by complex topography. The conceptual framework is provided in Figure 1. To achieve this end goal main objectives of the thesis are defined as follows.

[1] Application of Precipitation-elevation Regression on Independent Slopes Model (PRISM) to the study area to obtain rain gauge gridded precipitation dataset

[2] Performance evaluation of SBP products over complex topography and understand the advantages/disadvantages of the satellite-based precipitation estimation algorithms

[3] To assess how SBP products can be improved for complex topography, bias adjustment algorithm is proposed based on “physiographic similarity” concept

[4] Application of MIKE SHE-MIKE 11 hydrologic model driven by RGP, SBP products and bias adjusted SBP products.

[5] Application of diagnostic evaluation of physically based distributed integrated hydrological modeling in complex topography to conduct sensitivity analysis.

[6] Application of calibration methodology by step wise model parameter constraining approach.

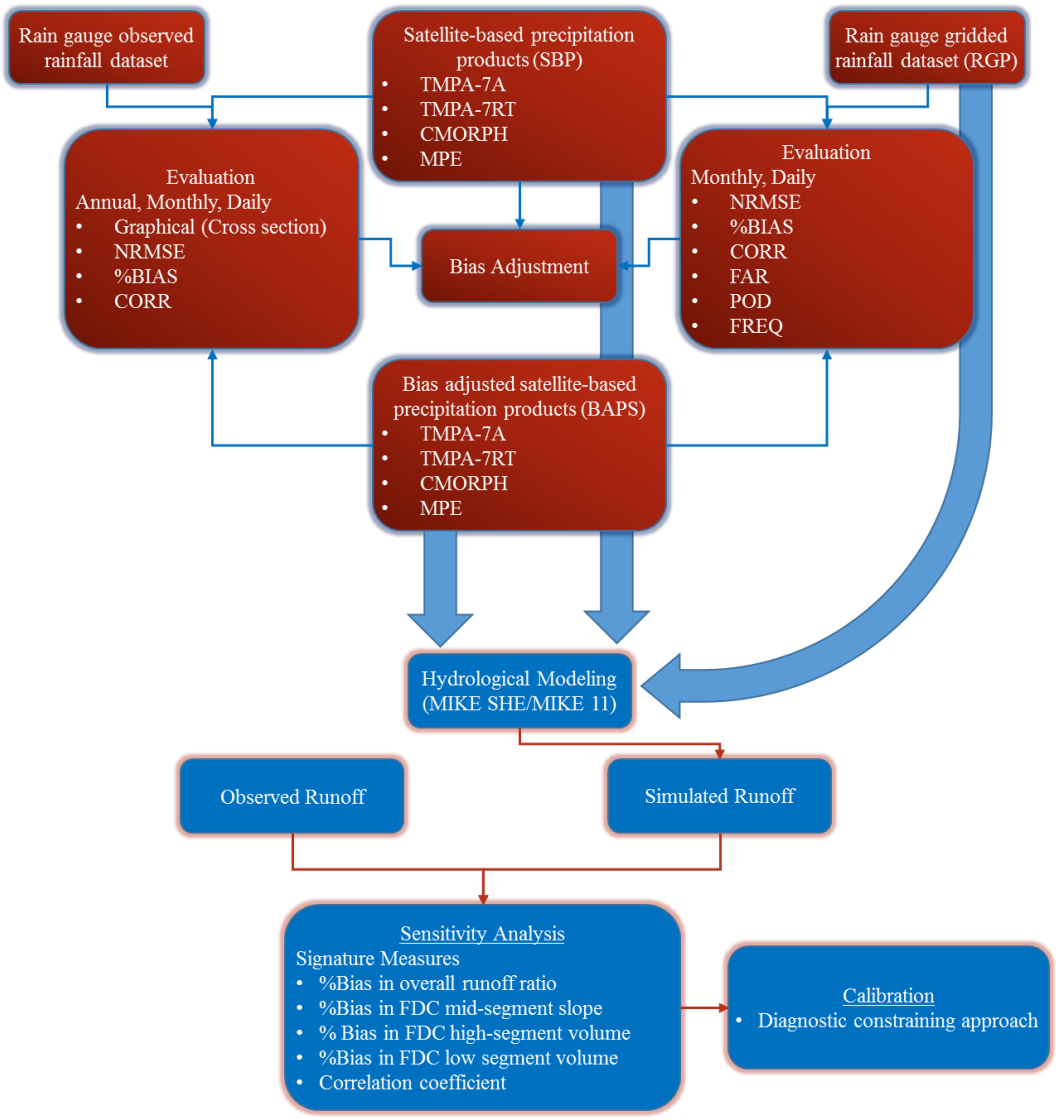

Figure 1 Conceptual framework of research

1.2. Study Area

The study area is located in the Western Black Sea Region of Turkey covering an area between 30.75^0-34.5^0 E longitude bands and 40^0-42.25^0 N latitude bands for evaluation and bias adjustment of satellite-based precipitation products. The hydrological modelling study was performed on Araç Basin, a sub-basin of Filyos Basin (Fig. 2).

The study area is surrounded by the Black Sea on the north, and steep mountain ranges on the south. Zonguldak, Bartın, Düzce, Bolu, Kastamonu, Karabük and Araç are the main settlements in the study area. The region is characterized by a complex topography, marked by Northeast-Southwest aligned mountain ranges running parallel to the shoreline. The altitude in the study area ranges in between 0 m in the north to 2500 m in the south where mountains start immediately after the shoreline (distance to shoreline between 5 km to 50 km). The study region covers an area of 52272.54 km^2 and the catchment area of the Araç basin is calculated as 854.92 km^2.

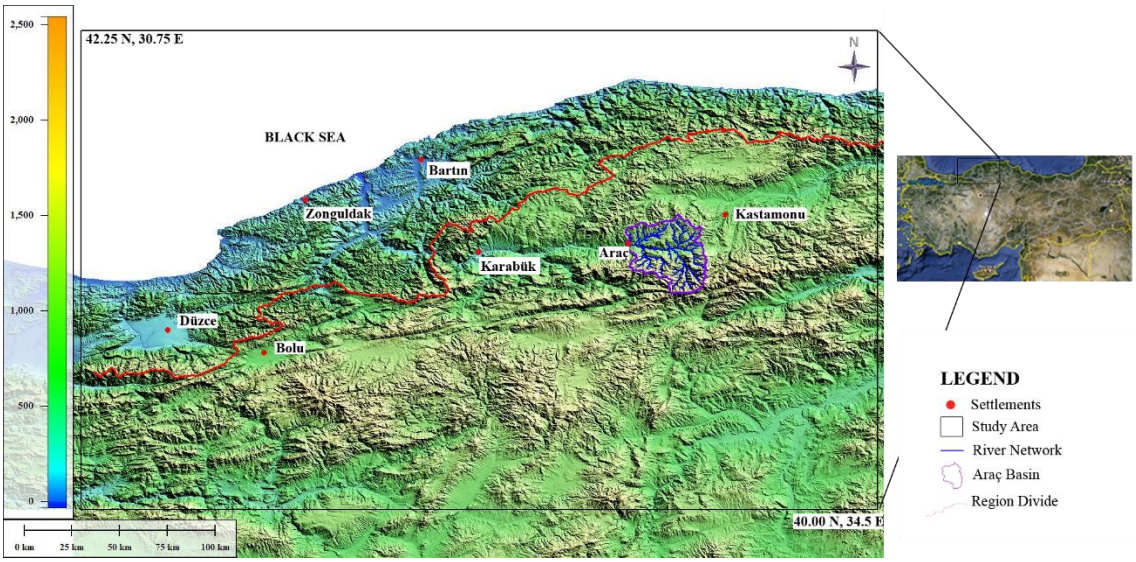

Figure 2 Study area

The main river of the region namely Araç River flows along East to West and cuts narrow, deep valley with the lowest elevation of around 750 m. At the South part of the region

elevation exceeds 2000 m. Araç River's upstream is situated to the South of the Ilgaz Mountain and downstream of the river is at Iğdır. Land cover of the region is mainly forest. Along the flood plain and near the river agriculture can be observed. Beet, vegetable and fruit trees are common agricultural products.

Study area is divided into two regions based on the climatic and topographic characteristics, both of which are predominantly influenced by the mountains; hence the region boundary closely follows the orographic divide (Fig. 2). Region 1, located to the north of the mountains (windward) receives significant orographic precipitation and characterized by Mid-latitude Humid Temperate Climate, whereas Region 2 is located to the south of the mountains (leeward) and hence is characterized by a Dry/Sub-humid Continental Climate. Mean monthly precipitation distribution (2007-2011 period) obtained from rain gauges located in Region 1 and Region 2 are provided in Figure 3. It can be seen from Figure 3 that Region 1 receives more precipitation throughout the year, more significantly during winter.

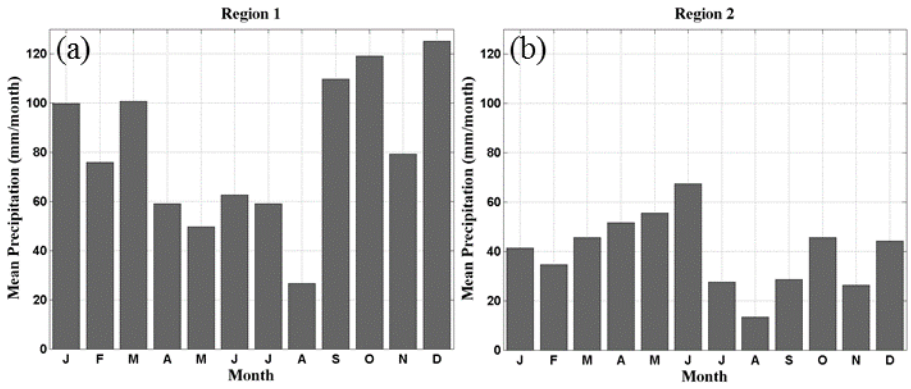

Figure 3 Mean monthly precipitation distribution (2007-2011 period) obtained from rain gauges in (a) Region 1 and (b) Region 2

1.3. Earlier Studies Performed in the Study Area

Within and around the Western Black Sea Basin of Turkey, geological, hydrogeological and hydrological studies have been carried out by other researchers. Brief explanation about these studies is given below.

Hydrogeological characterization of the Araç Basin was conducted by DSİ (1968). DSİ (1968) investigated the geological and lithological characters and water bearing properties of the formations in the Araç Basin. Region is characterized as forested mountains which receives 512.2 mm annual precipitation. Paleozoic schist is characterized as base-rock of the region and overlain by Mesozoic, tertiary and quaternary formations. Tertiary andesite, tuff and agglomerates are observed on top of Eocene flysch and limestone alterations at the Eastern part of the region. They concluded that due to geologic character of the region, lithology and water retention ability of the formations, there is no significant aquifer within the basin.

Turan (2002) integrated Geographic Information Systems (GIS) and MIKE 11 hydrologic model for Ulus Basin, a sub-basin of Bartın Basin, in the Western Black Sea Basin of Turkey. In his Master Thesis Turan (2002) analyzed flood events by integrating GIS and MIKE 11 and obtained inundation maps of the study region for 1991, 25 year, 50 year and 100 year flood events separately.

Turkey Emergency Flood and Earthquake Recovery (TEFER), Flood Forecasting Model Development project in 2002 developed a flood forecasting model for Western Black Sea Basin. The forecasting system incorporated the three major river systems in the catchment: the Filyos, Melen and Bartin. Decision support system for flood management (FLOOD WATCH), developed by DHI Water and Environment was implemented during this project. FLOOD WATCH combines the compilation of real time data with rainfall and flood forecasting and presentations of the information and results. It operates within GIS environment, the hydrologic model MIKE 11 is at the core of this system.

Tombul et al (2004) determined soil hydraulic properties using pedotransfer functions in Kurukavak Creek, a sub-basin of the Sakarya Basin, in the Western Black Sea Basin. In this study field measurements of soil hydraulic properties are evaluated against the

indirect methods including various pedotransfer functions. As a result they concluded that since soil hydraulic property values may affect the performance of hydrologic model, accurate site-specific measurements of these values are the only and probably the most accurate method.

Soytekin (2010) modelled the Çoruh Basin (close to the study region) by using HEC-HMS. In her MSc thesis model is driven by TMPA 3B42 and 3B43 for 2003 and 2005 water years. As a result she found out that TMPA 3B42 and 3B43 are promising while estimating the flow values.

Geological map of scales 1/500000, 1/100000 and 1/25000 of the study area were prepared by the General Directorate of Mineral Research and Exploration (MTA). Latest studies about geology of the study area were performed by Uğuz and Sevin (2011). Hydrogeological map of scales 1/500000 of the study area were prepared by the District Office of State Hydraulic Works (DSİ).

Moreover, Yücel and Onen (2014) evaluated the performance of Weather Research and Forecasting (WRF) model and MPE algorithm for chosen heavy rainfall events with rain gauges over Western Black Sea region of Turkey. Heavy rainfall events in general generated by deep convection system. They concluded that while WRF can capture the timing of extreme events and to some extent its spatial distribution and magnitude, MPE showed poor performance. Further they stated that MPE requires adjustments for its substantial underestimation behavior. Yücel and Onen (2014) suggest that significant underestimation of the MPE might be due to MPE's insensitivity to deep convection and look-up table of MPE should be tuned.

CHAPTER 2

SATELLITE-BASED PRECIPITATION PRODUCTS

2.1. Introduction

The accuracy and reliability of hydrologic studies heavily depends on the availability of good quality precipitation estimates. Precipitation measurement can be conducted as ground-based precipitation measurements (such as rain gauge and radar networks) and satellite-based precipitation measurements. Rain gauges provide direct physical measurement of the surface precipitation, however they are susceptible to certain errors such as, size of collector, evaporative loss, out-splash, levelling, siting of gauges, the effect of wind, etc. (Strangeways, 2011). Moreover, establishing and maintaining infrastructure of the rain gauge and radar network are costly. Further these networks are either sparse or non-existent in remote parts of the world and in developing countries. This situation is further exacerbated in regions with complex topography, where precipitation is characterized by high spatio-temporal variability. In these regions, rain gauges are generally located in lowland due to accessibility considerations, thus under-representing the precipitation occurring in highland. SBP products are perhaps the only source to fill this important gap. SBP retrieval algorithms enables representation of high space-time variability of precipitation field with quasi-global coverage hence they are potentially attractive for hydrologic modeling studies in data sparse regions.

2.2. Satellite-based Precipitation Estimation Methods

Physical measurement of precipitation by satellite is not possible. Satellites measure electromagnetic radiation which is indirectly converted to precipitation rate by algorithms. Electromagnetic radiation is solar radiation in the

- Visible (VIS) and near infrared (IR) bands reflected or scattered without any change of wavelength by the earth's surface and atmosphere.
- Thermal infrared and microwave (MW) bands, radiated by feature of the surface and atmosphere having been heated by solar radiation, re-emitting the energy at longer wavelengths (measure radiation of natural origin). Also active microwave which emits radiation actively from the platform and measure the returned scattered signal.

These wavelengths are measured by different sensors on board different types of satellites which are grouped according to their orbital placements (Strangeways, 2011). They can be grouped into three as geostationary, polar and skewed.

- If satellite is placed an orbital distance of 35786 km from the earth and orbits in the same direction as the earth rotates, satellite appears stationary in the sky, hence named geostationary.
- If satellite track is placed over the poles. For example, meteorological satellites usually fly an altitude of 850 km with an orbital period of around 100 minutes. The plane of these orbits is usually kept facing the sun keeping the same angle to sun at each pass. Therefore these satellites provide same view of the earth at different times of the day which is a disadvantage for precipitation detection when we consider their diurnal variations. These satellites can also be skewed where satellite orbiting by any angle relative to the poles (Strangeways, 2011).

Geostationary satellites provide same view of the earth all the time, earth's surface is seen square-on, with pixel resolution typically for visible wavelength as 2.5 km x 2.5 km while for IR wavelength as 5 km x 5 km. These satellites mainly collect information on clouds once every 30 minutes. Off-nadir view is oblique to a point where there is no view at all

therefore restricting the measurement from high polar regions. Even though they provide continuous coverage range and resolution of the images are limited. There are several operational geostationary meteorological satellites in orbit such as Geostationary Operational Environmental Satellites, Meteosat, Elektro-L 1and MTSAT-1R.

In contrast polar orbiting satellites sweep out swap up and down the earth and over the poles to higher spatial resolution and use MW with other channels. These satellites can pass over the poles at any point several times a day on the other hand at any point on the equator satellite provides only two overpasses a day. Satellites in skewed orbits cannot pass over the poles though they can provide measurement at different times of the day at each overpass. There are several operational polar orbiting satellites in orbit such as NOAA, METEOR, US Defense Meteorological Satellite Program (DMSP) and TRMM.

Satellite sensors provide images composed of numerous individual pixels which should be converted to numerical information. Radiometers measure the radiance and the strength of the received signal in the IR and MW bands which are then converted to temperature by using the concept of brightness temperature. By Planck's radiation law for perfect absorbers or emitters brightness temperature is expressed as:

$$Brightness\ temperature, T_B = I(\frac{\lambda^2}{2k}) \qquad (2.1)$$

where, I: radiance

λ: wavelength

k: Boltzmann's constant

Brightness temperature then converted to precipitation by the algorithms. Therefore we can say that accuracy of the precipitation measurement is limited by the skill of the algorithms. Limitations can be the physical complexity that need to be modeled and the resolution provided by the sensors. SBP algorithms estimate precipitation rate based on one or more remotely-sensed characteristics of clouds, such as: reflectivity of clouds

(VIS), cloud-top temperature (IR) and scattering effects of raindrops or ice particles (passive microwave, PMW) (Kidd and Levizzani 2011).

Visible and IR bands measurements starts from 1970s which are the first satellite measurements to measure precipitation (Strangeways, 2011). Even though today these datasets are the longest run of data, their precipitation measurements are not so accurate. Visible and IR sensors are available on geo-stationary orbiting satellites; these sensors provide data at fine and continuous temporal scales. However, the link between cloud top temperature and precipitation is indirect and often weak, hence these sensors provide crude estimates. There are three main approaches to measure precipitation from visible and IR band measurements: cloud indexing, bispectral methods and life-history methods. It should be noted that these methods usually restricted to the tropics.

Cloud indexing

Thermal IR measurements (10.5 to 12.5 μm) of cloud-top temperature (typically around -40 ^{0}C) are used to estimate precipitation. These measurements can be coupled with the ground network to obtain more accurate results since measurements are conducted by observing clouds from above rather than rain falling from cloud to ground and within cloud. The widely used cloud indexing algorithm is developed by Arkin (1979) and improved by Arkin and Meisner (1987) named as GOES Precipitation Index (GPI). Algorithm uses cloud area that is colder than -38 ^{0}C and radar ground network. By using their correlation, clouds with this temperature are assigned a constant rain rate at 3 mm/h (suitable for tropical precipitation) over an area of 2.5^0 x 2.5^0. Further this algorithm is improved by local rain gauges and MW datasets. To take advantage of spatial resolution and coverage, this algorithm is also used with polar orbiting satellites (Strangeways, 2011). Algorithms advantage is that its dataset has the longest run.

Bispectral methods

The RAINSAT algorithm (Lovejoy and Austin 1979, Bellon et al. 1980) combines IR band with visible channel. This algorithm cannot be used at night. They combine the information from visible band such as cold clouds (thin cirrus) which lack water vapor within and warm clouds (stratiform) which cannot produce precipitation.

Life-history methods

By examining the convective clouds life cycle, probability and intensity of the precipitation can be estimated (Strangeways, 2011). This examination can be conducted by geostationary satellites since temporal resolution is finer. This method works well in the regions dominated by convective clouds such as tropics and not work well in higher latitudes dominated by stratus clouds (Levizzani et al. 2002).

PMW sensors are available on polar-orbiting satellites; although these sensors provide accurate estimates of precipitation their temporal resolution is coarse. They provide the direct interaction between the hydrometeors and the radiation field by monitoring precipitation structure inside the clouds. Since these sensors are on polar orbiting satellites they can overpass the same location twice a day resulting in significant gaps in time series data. With the launch of SSM/I in 1987 several algorithms developed to determine precipitation rate from MW bands.

MW is either scattered, radiated or absorbed by ground and hydrometeors as can be seen from Figure 4. MW reaches to satellite after multiple integration of emission, absorption and scattering form ground, cloud, snow, sea and rain drops. Since signal received by satellite is not from a single source, signal should be differentiated. However neither ground nor hydrometeors has strong polarization signature therefore differentiation is complex procedure.

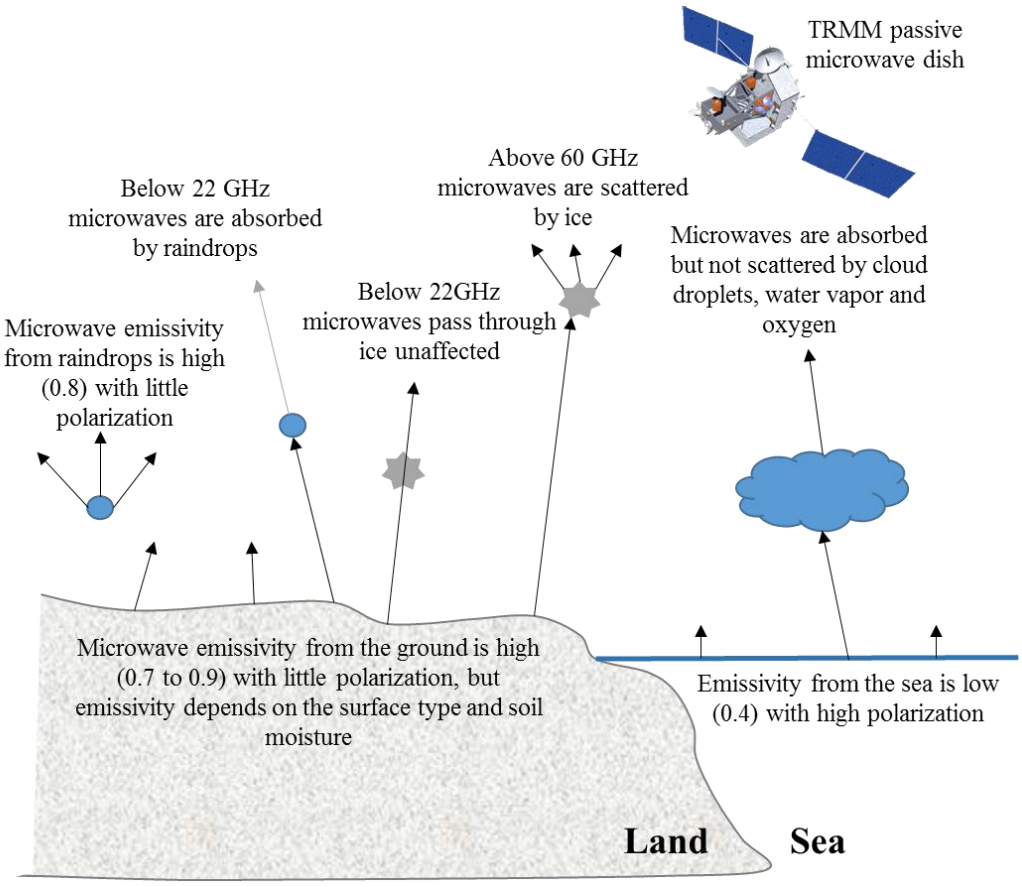

Figure 4 Microwave interaction with land, sea and hydrometeors (modified from Strangeways (2011)).

The most used algorithm to determine precipitation rate from MW bands is developed by Kummerow and Giglio (1994a, 1994b) the Goddard Profiling (GPROF) algorithm. To retrieve instantaneous rainfall this algorithm uses Bayesian based approach through a radiative transfer model to match observed and simulated brightness temperature databases (Kummerow et al. 2001, Wang et al. 2009).

More recent algorithms combine measurements from multiple sources, such as IR, PMW and rain gauges, to take advantage of the strengths of each source and provide more accurate and reliable precipitation estimates (Huffman et al. 2007; 2010; Huffman 2013; Joyce et al. 2004; Aonashi et al. 2009; Sorooshian et al. 2000). Even though SBP estimates contain considerable error, the ongoing improvements and future planned

satellite missions (Global Precipitation Measurement, GPM) make them potentially useful for hydrologic modeling studies in large basins (Yilmaz et al. 2005; Su et al. 2008; Thiemig et al. 2013).

2.3. Satellite-based Precipitation Products

2.3.1. TRMM Multi-satellite Precipitation Analysis (TMPA)

TMPA provides precipitation estimates by combining information from multiple satellites as well as rain gauges where feasible, and is available at 3-hourly, 0.25^{o}x0.25^{o} latitude–longitude spatial resolution. There are two TMPA products: (1) an experimental real-time monitoring product which is available approximately 9 hours after real-time and covering the globe between the 60^{o} N–S latitude bands; (2) a post-real-time research quality product available nearly 10-15 days after the end of each month and covering the globe between the 50^{o} N–S latitude bands. The real-time product makes use of TRMM's highest quality observations, along with a high quality PMW-based rain estimates from three to seven polar-orbiting satellites and IR estimates from the international constellation of geosynchronous earth orbit satellites, all calibrated by information from TRMM. Post-real-time research quality product differs from experimental real time monitoring product mainly in two ways: (1) it incorporates monthly rain gauge analysis for bias correction; (2) it uses the TRMM Combined Instrument (TCI) precipitation product for calibration, as opposed to the TRMM Microwave Imager (TMI) used in experimental real time monitoring product. TRMM provide a coverage from 40^{o}N-S latitudes, thus present study will highlight the performance of the TMPA products at latitudes higher than the TRMM coverage.

The latest version of the TMPA products (Version 7; Huffman, 2013) were used in this study. In this new version, both TMPA products have been retrospectively processed by algorithm developers with an aim to improve the fine-scale patterns of precipitation during 2000-2010 for post-real-time research quality product and 2000 to late 2012 for experimental real time monitoring product (Huffman, 2013). Hereafter, experimental real time monitoring product will be referred as TMPA-7RT and post-real-time research

quality product will be referred as TMPA-7A. TMPA-7A product include reprocessed datasets used in previous version (Version 6) and has the following upgrades relevant to the current study: Additional datasets were incorporated (e.g. Special Sensor Microwave/Imager ,SSM/I); Microwave Humidity Sounder, MHS; Meteorological Operational satellite programme and the 0.07^0 Gridsat-B1 infrared data),; single, uniformly processed surface precipitation gauge analysis were used as computed by the Global Precipitation Climatology Centre (GPCC), latitude-band calibration scheme were used for all satellites. Note that four rain gauge stations used in this study, namely ZNG, INB, BOL, KST, report to the GPCC and hence already incorporated into the TMPA-7A product. Input data for both TMPA-7A and TMPA-7RT products were uniformly reprocessed in time for consistency (Huffman 2013).

2.3.2. Climate Prediction Center Morphing Technique (CMORPH)

CMORPH estimates precipitation from high quality passive microwave satellite sensors (AMSU-B, SSM/I, TMI), which are than propagated by motion vectors derived from more frequent geostationary satellite IR data (GOES-8, GOES10, Meteosat-7, Meteosat-5 and GMS-5). Advection vectors of cloud and precipitation systems over the globe are computed by successive IR observations. With the help of these advection vectors, infrequent MW observations are interpolated by "moving" the precipitation systems along the advection vectors in the combined time-space domain. The resulting product is a spatially and temporally complete microwave-derived precipitation analyses that is independent of the infrared temperature field (Joyce et al. 2004). In this study 3 hourly, 0.25^0 x 0.25^0 spatial resolution CMORPH data spanning 60^0 N-S latitude bands were used.

2.3.3. Multi-Sensor Precipitation Estimate (MPE)

MPE algorithm (Heinemann, 2003) estimates near-real time precipitation rates by blending measurements from Special Sensor Microwave/Imager (SSM/I) with brightness temperatures from IR channel of the METEOSAT geostationary satellites (METEOSAT-7, METEOSAT-8 and METEOSAT-9). SSM/I and METEOSAT measurements are temporally and spatially co-registered to derive look-up tables (LUTs). LUTs describe the rain rate as a function of the METEOSAT IR brightness temperature. Product is

generated over the regions up to 60^0 longitude and latitude from the nominal sub-satellite points of three satellites. Since MPE is produced on the assumption that cold clouds produce most rain, product estimation is most effective for convective precipitation. For this study, MPE product having a 15-minute temporal and 4km x 4km spatial resolution is used.

2.4. Literature Review of Evaluation of Satellite-based Precipitation Products

SBP products are available with quasi-global coverage however their performance largely depends on the hydro-climatic characteristics of the region (Yilmaz et al. 2005). Hence evaluation of these products in different regions will provide the expected error characteristics to the end-users and feedback to the algorithm developers. There is an increasing number of studies focusing on the evaluation of the performance of SBP products (Ebert et al. 2007; Sapiano and Arkin 2009; Tian et al. 2007; Kidd et al. 2012). However, studies evaluating the performance of these algorithms over complex topography is still very limited.

The regions characterized by complex topography are among the most challenging environments for SBP estimation due to high spatio-temporal variability of precipitation controlled by the orography. Orographic precipitation is generated by the cooling of the air as the mountains block and force the wind to rise in order to pass over them. This phenomenon is evident worldwide (Hutchinson 1968, Vuglinski 1972). Since mountains block the wind and forces the air to rise, windward side of the mountain receives more precipitation and leeward side remains drier. As a result of this rain shadow effect sharp climate transition is observed.

SBP products that utilize information from combination of IR and PMW sensors are faced with challenges over complex topography. The challenge for IR retrievals is mainly attributed to warm orographic rain which cannot be detected by the IR retrievals that use cloud top temperature hence lead to underestimation of orographic rains (Dinku et al. 2008) and miss light-precipitation events (Hong et al. 2007). The underestimation by PMW retrievals over mountainous region is attributed to warm orographic clouds without

ice particles that produce heavy rain (Dinku et al. 2010). The overestimation by PMW retrievals over mountains can be related to classification of cold surface and ice covers as rain clouds (Dinku et al. 2007; Gebregiorgis and Hossain 2013). SBP algorithms are prone to all these errors in mountainous regions and should therefore be evaluated in detail. Despite the importance of SBP products over complex topography, there are only a few studies that focus on evaluation of these products over mountainous regions. Hirpa et al. (2010) found out that TMPA 3B42RT and CMORPH SBP products have similar performances at lower elevations, however over higher elevations both products suffer from elevation dependent bias. Dinku et al. (2010) compared CMORPH, TMPA-3B42 and TMPA-3B42RT over two mountainous regions which are characterized by complex topography. They found out that both products have low correlation and underestimated occurrence and amount of precipitation. Another study by Stampoulis and Anagnostou (2012) indicated that over mountainous regions in Europe both CMORPH and TMPA-3B42V6 products significantly overestimate precipitation in cold season due to snow/cold surface contamination and that CMORPH shows higher accuracy in winter relative to TMPA 3B42V6. Moreover, they noted that the error variance of the SBP products is season dependent and generally higher over mountains. In summary performances of SBP products vary significantly over topographically complex regions and complicated by significant elevation change, seasonality and snow cover. Yücel et al. (2011) used hydro-estimator algorithm to evaluate its performance over mountainous region against point based rain gauges. The product is already orographically corrected however elevation-dependent biases still exists which were observed as underestimate in the occurence of light precipitation at high elevations and overestimate in the occurrence of precipitation at low elevations.

CHAPTER 3

EVALUATION OF SATELLITE-BASED PRECIPITATION PRODUCTS

The objective of this chapter is to evaluate multiple SBP products over Western Black Sea Region of Turkey, which is characterized by complex topography. The effect of the complex topography on the performance of these products is studied using a rain gauge network and a rain gauge-based gridded dataset interpolated via a procedure considering physiographic controls on precipitation. Four different SBP products are evaluated: TMPA including experimental real time monitoring product and post real time research quality product; CMORPH and the MPE.

Present study differs from and complements previous studies in several aspects. First the study area is characterized by a complex topography with significant orographic precipitation and a distinct rain-shadow effect. Second the evaluation is based on a gridded rain gauge dataset constructed using the "physiographic similarity" concept which is well-suited to regions with complex topography. Third, the TMPA products (TMPA-7RT and TMPA-7A) are retrospectively processed with the latest algorithm hence the performance of these new products having uniform temporal error characteristics are presented. In addition, the source of the error in SBP products were further investigated via an analysis of the input data (IR and MW data) utilized in the development of these products.

3.1. Study Area

The study area is explained in detail in Chapter 1.2.

3.2. Datasets

3.2.1. Rain Gauge Dataset

Rain gauge dataset was provided by the Turkish State Meteorological Service (TSMS). There are 39 rain gauges in the study region (Fig. 5) where TSMS operates two types of meteorological stations in the study region; Automated Weather Observing Systems (AWOS, 25 station in study region) and pluviometer type stations (14 station in study region) (Table 1).

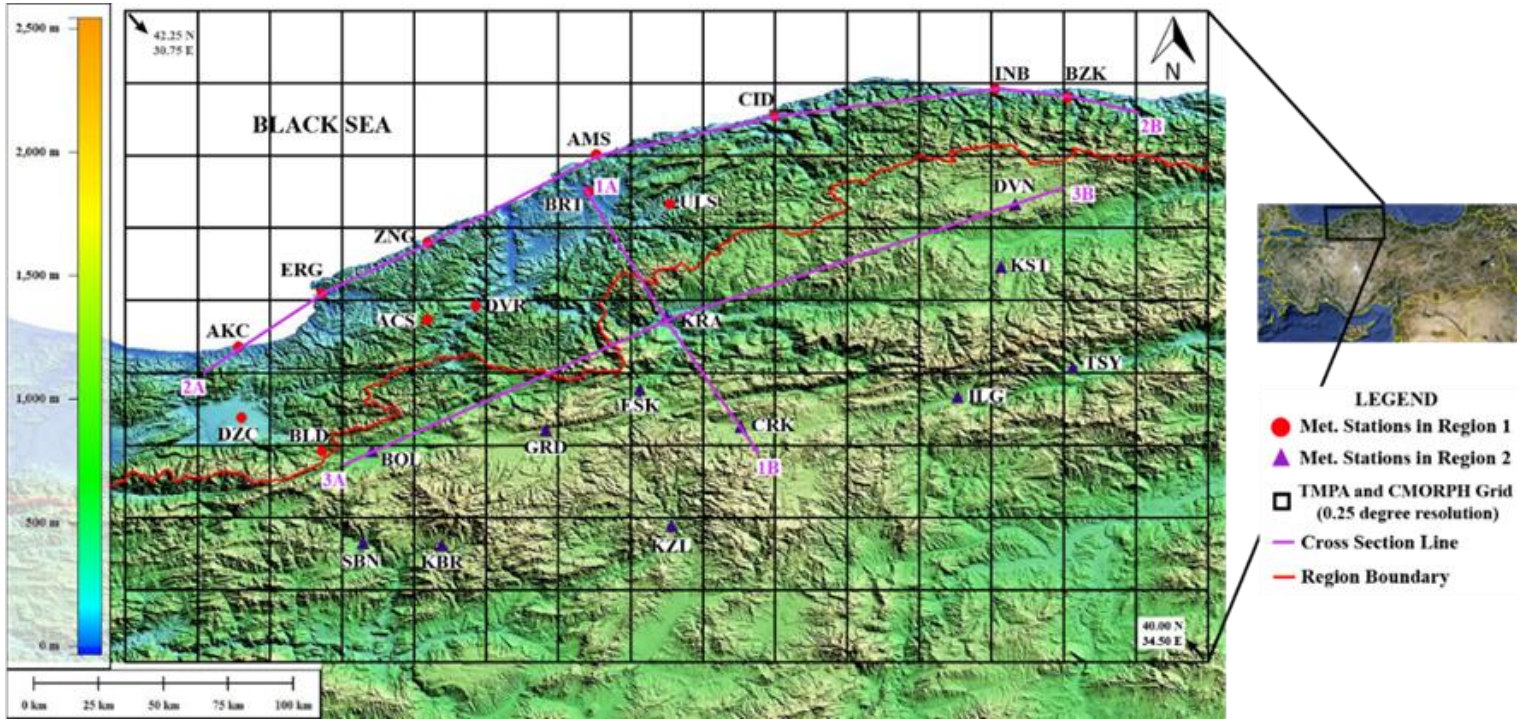

Figure 5 Geographic location of the study region. Meteorological stations within Region 1 are marked by a “dot marker” and those within Region 2 are marked by a “triangle marker”.

Data from the AWOS stations were available at the hourly timescale, whereas the pluviometer type stations report three times a-day. Since the number of pluviometer stations are less than the AWOS stations, AWOS stations are chosen for this study. Pluviometer stations datasets are quality controlled by the TSMS however AWOS are not thus requiring quality control of the dataset. All pluviometer stations are co-located with an AWOS station hence providing an opportunity for the quality control of the data.

Table 1 General information about the meteorological stations

Station Name	**Station ID[Region]**	**Elevation (m)**	**Mean Annual Precipitation (mm/year)***	**Type**
AKCAKOCA	AKC[1]	1	1069.08	AWOS, Pluviometer
BARTIN	BRT[1]	33	907.26	AWOS, Pluviometer
DUZCE	DZC[1]	146	715.32	AWOS, Pluviometer
AMASRA	AMS[1]	33	833.16	AWOS, Pluviometer
CIDE	CID[1]	25	1046.8	AWOS, Pluviometer
BOZKURT	BZK[1]	82	1149.26	AWOS, Pluviometer
ACISU RADAR	ACS[1]	1096	952.32	AWOS
EREGLI	ERG[1]	6	1142.73	AWOS
ULUS	ULS[1]	179	824.22	AWOS
BOLUDAGI	BLD[1]	883	1000.08	AWOS
DEVREK	DVR[1]	70	809.00	AWOS
INEBOLU	INB[1]	36	1039.84	AWOS, Pluviometer
ZONGULDAK	ZNG[1]	74	1077.42	AWOS, Pluviometer
KARABUK	KRA[2]	242	444.16	AWOS, Pluviometer
DEVREKANI	DVN[2]	1142	565.58	AWOS, Pluviometer
CERKES	CRK[2]	1111	386.42	AWOS, Pluviometer
ILGAZ	ILG[2]	859	433.46	AWOS, Pluviometer
KIZILCAHAMAM	KZL[2]	1023	560.64	AWOS, Pluviometer
ESKIPAZAR	ESK[2]	740	413.41	AWOS
GEREDE	GRD[2]	1305	536.34	AWOS
SEBEN	SBN[2]	767	447.44	AWOS
KIBRISCIK	KBR[2]	1129	432.75	AWOS
TOSYA	TSY[2]	869	466.42	AWOS
KASTAMONU	KST[2]	906	560.2	AWOS
BOLU	BOL[2]	728	533.86	AWOS, Pluviometer

*based on quality controlled AWOS data for the 2007 – 2011 time period.

Pluviometer stations measure rainfall within 07:00-13:59 (time stamp as 07:00) / 14:00-20:59 (time stamp as 14:00) / 21:00-06:59 (time stamp as 21)) hour intervals on the other hand AWOS record hourly rainfall. It should be noted that time stamps for both stations are accumulated time intervals and pluviometer measurement time zone is defined as UTC+2 time zone on the other hand AWOS time zone is defined as UTC. TSMS defined daily rainfall by adding yesterday's 14:00 and 21:00 and today's 07:00 time stamps. Since quality control is going to be conducted according to the pluviometer stations we defined the daily rainfall same with TSMS. While obtaining daily precipitation daylight saving is considered also.

In the quality control step, first metadata errors are checked. Mislocated stations are identified via Google Earth software and discussions with Dr. Kurtuluş Öztürk of TSMS. The corrected coordinates elevations of the stations are provided from the DEM with a 3-arc second (0.00083^0) resolution (obtained from the HYDROSHEDS dataset (Lehner et al. 2006)). All these corrections are provided in the Table 2.

Table 2 Quality control of the metadata errors of AWOS stations

Station	Lat from TSMS	Long from TSMS	Elevation from TSMS (m)	Lat corrected	Long corrected	Elevation from DEM	Lat Differences	Long Differences	Elevation Differences
AKCAKOCA/17015	41.083	31.167	10	41.089	31.143	1	-0.006	0.024	9.0000
BARTIN/17020	41.633	32.333	32.	41.625	32.357	32.8	0.008	-0.024	-0.3160
ZONGULDAK/17022	41.450	31.800	135.	41.449	31.799	73.5	0.001	0.001	61.8180
INEBOLU/17024	41.983	33.783	63.8	41.979	33.764	35.8	0.004	0.019	27.9230
BOLU/17070	40.733	31.600	743	40.732	31.605	728	0.001	-0.005	14.9170
DUZCE/17072	40.833	31.167	145.6	40.843	31.154	146.3	-0.010	0.013	-0.6340
KARABUK/17078	41.200	32.633	259.3	41.194	32.624	242.2	0.006	0.009	17.1390
AMASRA/17602	41.750	32.383	73	41.753	32.383	33.3	-0.002	0.000	39.6660
CIDE/17604	41.883	33.000	36	41.883	33.000	24.7	0.000	0.000	11.2860
BOZKURT/17606	41.950	34.017	167	41.950	34.017	81.6	0.000	0.000	85.3400
DEVREKANI/17618	41.583	33.833	1050	41.583	33.833	1141.7	0.000	0.000	-91.7980
CERKES/17646	40.817	32.900	1126	40.815	32.883	1111.5	0.002	0.017	14.5290
ILGAZ/17648	40.917	33.633	885	40.917	33.633	859.1	0.000	0.000	25.8660
KIZILCAHAMAM/17664	40.467	32.650	1033	40.473	32.644	1023.3	-0.006	0.006	9.6970
ACISU RADAR/17018	41.181	31.799	1112	41.182	31.798	1096	-0.001	0.001	16.0000
EREGLI/17611	41.267	31.417	191	41.271	31.433	5.5	-0.004	-0.015	185.5330
ULUS/17615	41.582	32.637	162	41.582	32.637	178.5	0.000	0.000	-16.4750
BOLUDAGI/17637	40.740	31.419	948	40.729	31.433	882.9	0.011	-0.014	65.0970
ESKIPAZAR/17641	40.967	32.533	757	40.944	32.533	740.5	0.023	0.000	16.4920
GEREDE/17642	40.800	32.200	1270	40.803	32.206	1304.5	-0.003	-0.006	-34.5290
SEBEN/17693	40.417	31.583	757	40.413	31.573	766.6	0.004	0.010	-9.5740
KIBRISCIK/17694	40.417	31.850	1025	40.406	31.848	1128.9	0.011	0.002	-103.9600
KASTAMONU/ 17074	41.367	33.783	799.9	41.367	33.783	905.8	0.000	0.000	-105.9750
DEVREK/ 17613	41.217	31.950	100	41.229	31.965	70.5	-0.011	-0.015	29.4340
TOSYA/ 17650	41.017	34.033	870	41.017	34.033	869.4	0.000	0.000	0.5820

Further consistency between the daily records of the co-located stations was checked through graphical (double mass curves, time-series and scatterplot) and statistical methods such as bias and correlation coefficient. Double mass curves, time-series and scatterplots are used to identify outliers and flat lines. Identification of outliers are conducted by determining threshold by using exceedence probability and outliers are flagged. Flagged data are later filled by pluviometer dataset if both stations are co-located. In the following Station Bozkurt is given as an example to this quality control.

Firstly flat lines are identified by double mass curves. It is clear from Figure 6 starting from 01/07/2011 there is a distinct flat line that needs to be quality controlled where AWOS rainfall measurements are around zero.

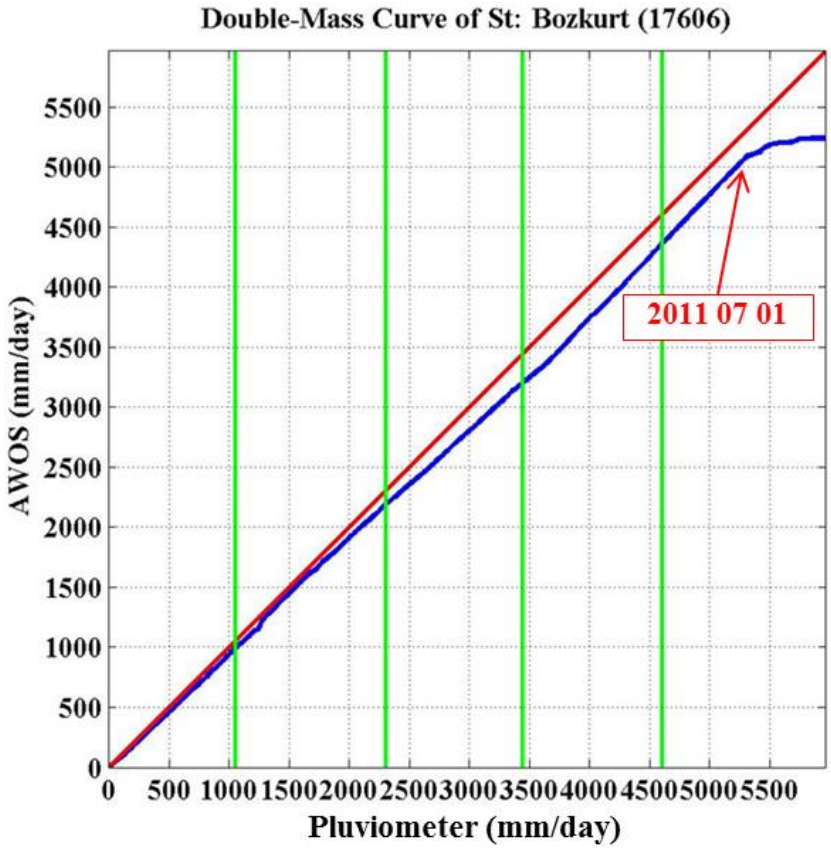

Figure 6 Double mass curve for Station Bozkurt (green lines represents the years (2007-2011) red line is diagonal 1-1 line and blue line is the double mass curve of Bozkurt AWOS & Pluviometer stations.

Secondly outliers are obtained by exceedence probability of bias in which threshold is defined as 95% exceedence probability of bias for every year. In order not to deteriorate the AWOS characteristics we did not flag every data which passes the threshold. For example biases in 2008 year are not flagged (Fig. 7a, b, and c). Flat line was observed in double mass curve after 01/07/2011, we are able to see the same problem in time series also. There are no precipitation record for this time period and biases are flagged for the same time period (Fig. 7d, e, and f). In the end the flagged dates are filled by collocated pluviometer station.

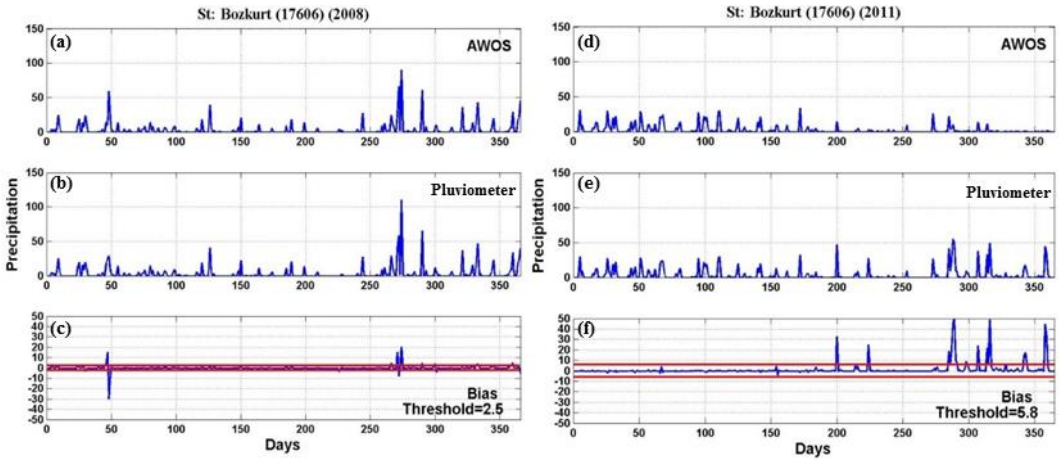

Figure 7 Time series to identify outlier for Station Bozkurt for two years one (2008) without flag and one (2011) with flag. (a, d) AWOS stations, (b, e) Pluviometer stations, (c, f) biases from AWOS and pluviometer stations and red line is threshold determined by exceedence probability.

After flagged dates are filled we checked scatter plot and double mass curve of the stations as can be seen from the Figure 8. It is clear that after the quality control station does not observe any false or missed reading (Fig. 8a) and there is no flat line after quality control (Fig. 8b).

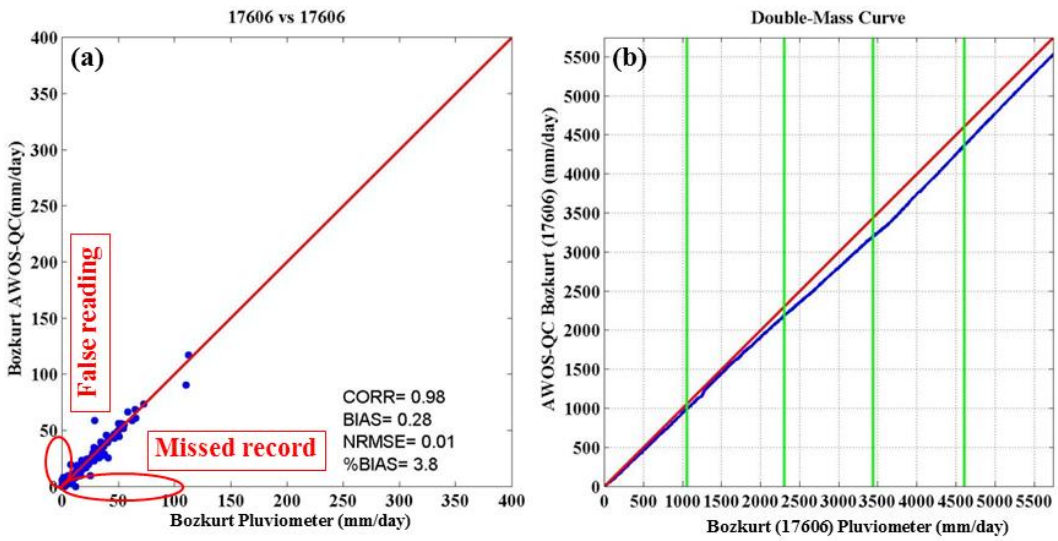

Figure 8 (a) Scatter plot of AWOS & pluviometer stations of Bozkurt to identify missed records and false readings after quality control, (b) Double-mass curve of AWOS & pluviometer stations of Bozkurt after quality control

If there is no collocated pluviometer stations with AWOS station we followed different approach. Double mass curves, time-series and scatterplots between similar stations (similarity is based on elevation and rainfall occurrence) are used to identify outliers and flat lines. Identification of outliers are conducted by determining threshold by using exceedence probability and outliers are flagged. Flagged data are later filled by using correlation weighting method (CCWM, Westerberg et al. 2009). CCWM has same principle with inverse distance weighting (IDW) method but correlation coefficient used instead of distance to calculate the weight of the surrounding stations.

$$Q_m = \frac{\sum_{i=1}^{n} Q_i R_{mi}}{\sum_{i=1}^{n} R_{mi}} \qquad (3.1)$$

where, Q_m: missing value to be patched,

R_{mi}: coefficient of correlation.

It should be noted that stations are grouped according to the defined regions since rainfall regimes of the two regions are different. In the following Station Eskipazar is given as an example to this quality control. Since there is no collocated pluviometer station in this location Station Çerkes is used to define outliers and flat lines, further, surrounding stations are used to correct flagged dates of Station Eskipazar by using CCWM. Station Eskipazar and Çerkes correlates very well and as can be seen from Figure 9 there are no flat lines, therefore there are no flagged dates related with flat line.

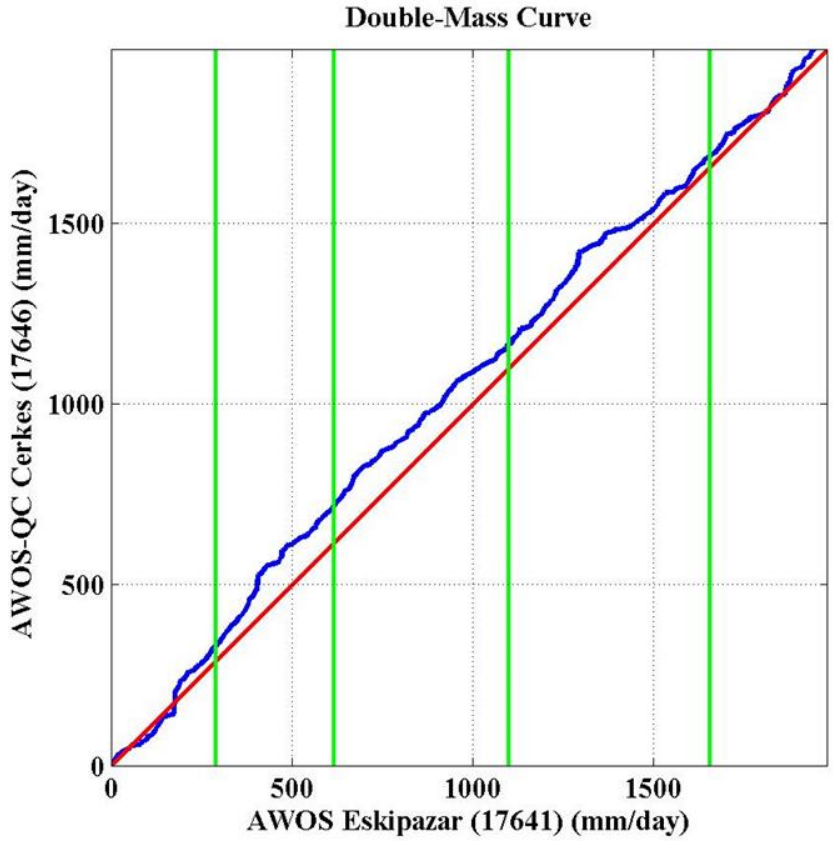

Figure 9 Double mass curve for Station Eskipazar and quality controlled Station Çerkes (green lines represents the years (2007-2011) red line is diagonal 1-1 line and blue line is the double mass curve stations.

Outliers are defined by exceedence probability in which threshold is defined as bias at 95% of the data for every year. In order not to deteriorate the AWOS characteristics we

did not flag every data which passes the threshold. For example biases in 2009 year are not flagged (Fig. 10a, b, and c) since their trends are similar. On the other hand biases in 2010 are flagged (Fig. 10d, e, and f). Outliers in between day 150-200 points out that precipitation recording in between these days are not correlated with the general trend of the station. Therefore days in between 20/05/2010-13/06/2010 are flagged. Flagged dates are filled by CCWM method by using the surrounding stations Karabük, Gerede and Çerkes.

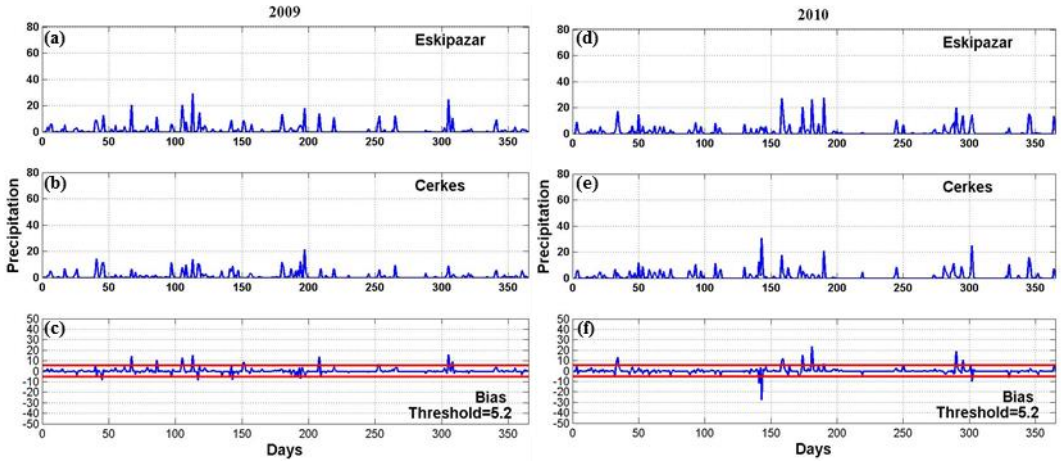

Figure 10 Time series to identify outlier for Station Eskipazar & Çerkes for two years one (2009) without flag and one (2010) with flag. (a, d) station Eskipazar, (b, e) station Çerkes, (c, f) biases from Eskipazar and Çerkes stations and red line is threshold determined by exceedence probability.

After flagged dates are filled we checked scatter plot and double mass curve of the stations as can be seen from the Figure 11. It is clear that after the quality control station does not observe any false or missed reading (Fig. 11a) and there is no flat line after quality control (Fig. 11b).

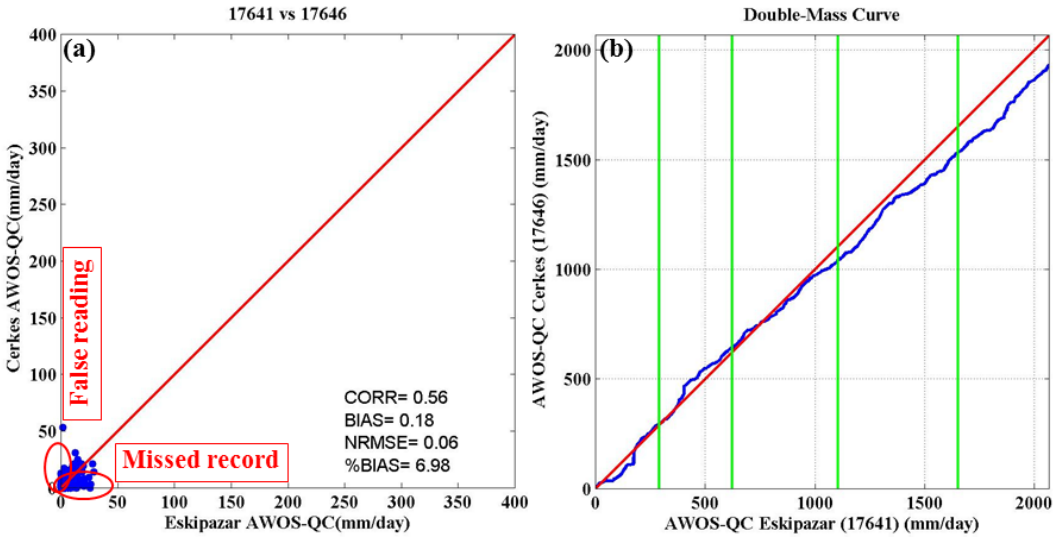

Figure 11 (a) Scatter plot of Eskipazar & Çerkes stations to identify missed records and false readings after quality control, (b) Double-mass curve of Eskipazar & Çerkes stations after quality control

The daily precipitation data from the quality controlled AWOS type stations were used in this study (Fig. 5). Hypsometric curve for the study region is provided in the next Figure. It is clear that there is no station located higher than 1500 m. Red dots in Figure 12 represent the stations in Region 1 and generally located in lowland and purple triangles represent the stations in Region 2 and generally located in highland.

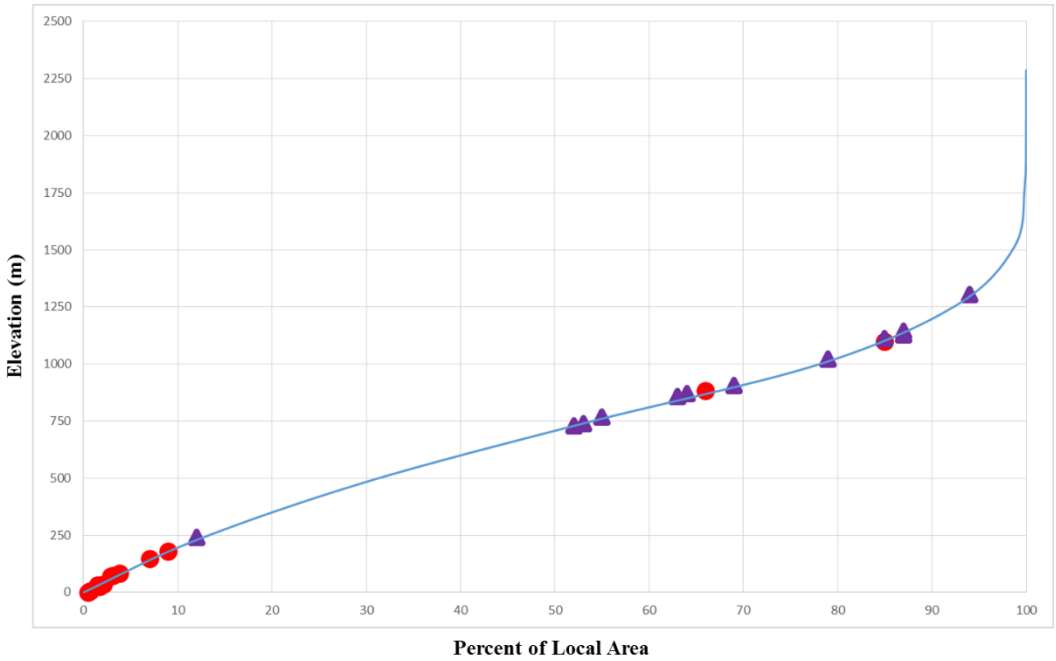

Figure 12 Hypsometric curve of the study region. Red dots represent the rain gauges in Region 1 and purple triangles represent the rain gauges in Region 2.

3.2.2. Rain gauge-based Gridded Precipitation dataset

Studies focusing on the evaluation of SBP estimates using rain gauge networks are hampered by the scale differences (grid vs. point) between the two products. In an effort to reduce this scale dependent inconsistency and to have a continuous rain gauge-based precipitation field, a rain gauge-based gridded precipitation product has been constructed. The procedure for gridded precipitation estimation is based on the Precipitation-elevation Regressions on Independent Slopes Model (PRISM; Daly et al. 2002; 2008; Daly 2006). The advantage of the PRISM approach is that it incorporates physiographic descriptors in the precipitation estimation, thus providing a knowledge-based system in which statistical approaches and human expertise are combined in a semi-automated fashion (Daly et al. 2002). Our ultimate goal is to incorporate the influence of the complex topography on the precipitation estimation process. The PRISM approach is specifically developed for regions having low/moderate density of rain gauges and under the influence

of significant topographic features, coastal effects and rain shadows (Daly 2006); such as the study area selected for this study.

PRISM calculates a linear precipitation-elevation relationship for each grid cell, the slope of which changes locally by the physiographic similarity between observed and estimated point/grid. A moving window procedure is used to calculate a unique climate-elevation regression function for each grid cell (Daly et al. 2008):

$$Y = \beta_1 * X + \beta_0 \qquad (3.2)$$

where, Y: predicted precipitation

β_1: slope of the regression line

β_0: intercept of the regression line

X: elevation at target cell obtained from the digital elevation model (DEM).

The DEM with a 3-arc second (0.00083^0) resolution is obtained from the HYDROSHEDS dataset (Lehner et al. 2006) and further rescaled to 0.05^o resolution via nearest neighbor interpolation; this is the grid scale that is used for the PRISM-based precipitation estimation.

In the PRISM approach precipitation estimation, a locally-weighted regression function (Fig. 13) is constructed for each grid.

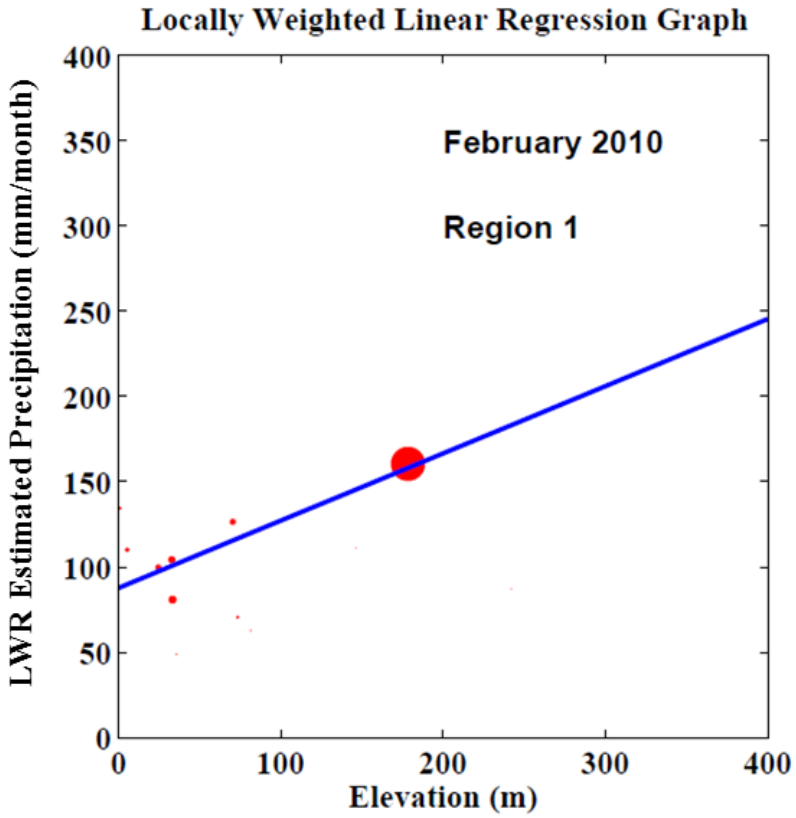

Figure 13 Linear regression graph of station KRA for February 2010. Red dots are surrounding stations, their size is related with the combined weight of that station.

In the procedure, each station is assigned weights based on the physiographic similarity between the observed and estimated station/grid. The similarity or the combined weight (W), of a station/grid is a function of the following set of physiographic descriptors:

$$W = ([F_d * W_d^2 + F_z * W_z^2]^{1/2} * W_p * W_f * W_e) \quad (3.3)$$

where, F_d: distance weighting importance factor

F_z: elevation weighting importance factor

W_d: the distance weight

W_z: elevation weight

W_p: coastal proximity weight

W_f: facet weight

W_e: effective terrain weight

These descriptors were selected based on the physiographic setting of the study area and the guidelines provided by Daly (2006). Note that all weights and importance factors, individually and combined are normalized to sum to unity (Daly et al. 2008).

- Distance weight (W_d): Stations influence in regression function is assumed to decrease as its distance from the target grid cell increases. The distance weight is given in Equation 3.4.

$$W_d = \begin{Bmatrix} 1;\ d = 0 \\ \frac{1}{d^a};\ d > 0 \end{Bmatrix} \qquad (3.4)$$

where, d: horizontal distance between station and the target grid cell

a: distance weighting exponent typically set to 2 (Daly et al. 2008)

- Elevation weight (W_z): Elevation weighting allows the model to focus on a vertical range that is specific to the target grid cell. A station's influence decrease as vertical, or elevation, distance from the target grid cell increases. Elevation weight is calculated as in Equation 3.5.

$$W_z = \begin{Bmatrix} \frac{1}{\Delta z_m^b}; & \Delta z \le \Delta z_m \\ \frac{1}{\Delta z^b}; & \Delta z_m < \Delta z < \Delta z_x \\ 0; & \Delta z \ge \Delta z_x \end{Bmatrix} \qquad (3.5)$$

where, Δz: absolute elevation difference between the station and the target grid cell

b: elevation weighting exponent, generally set to 1

Δz_m: minimum elevation difference typically varies from about 100 to 300 m

Δz_x: maximum elevation difference typically varies from 500 to 2500 m (Daly et al. 2002).

- Facet weight (W_f): A topographic facet is contiguous terrain slope with a common orientation, delineated at a variety of scales, from major leeward and windward sides of large mountain ranges to north-south facing hill slopes. At each grid cell, the model chooses the topographic facet scale that best matches the data density and terrain complexity, and assigns the highest weights to stations on the same topographic facet.

  The smoothed DEM for each level is prepared by applying Gaussian filter to the original DEM. The filtering wavelength for each of the 6 levels is controlled by user-defined maximum wavelength (λ_s=60/80/100km). The DEM is filtered at equal intervals between wavelengths equal to the DEM resolution. The orientation of each cell is computed from elevation gradients between the 4 adjacent cells and assigned to an orientation bin on an 8-point compass. At higher wavelengths, a distribution of orientation bins is created for the target cell by calculating the orientations of all neighboring cells within a radius that matches the filter wavelength.

  Combination of station data density and local terrain complexity determines the appropriate facet smoothing level for a target grid cell. To find this level PRISM attempts to retrieve a user-specified number of stations (S_f=3/5/8 stations) that are on the same contiguous facet as the target cell. Starting with the smallest-wavelength facets at level 1 then proceeding to level 2 and beyond if necessary, PRISM accumulates stations until either S_f reached or all facet levels have been exhausted.

  The facet weight for a station is calculated as;

$$W_f = \begin{cases} 1; & \Delta f \leq 1 \; and \; B = 0 \\ \frac{1}{(\Delta f + B)^c}; & \Delta f > 1 \; or \; B > 0 \end{cases} \qquad (3.6)$$

where, Δf: absolute orientation difference between the station and target grid cell (maximum possible difference is 4 compass points or 180^0)

B: number of intervening barrier cells with an orientation significantly different than that of the target grid cell. It is calculated by identifying a line of cells that follows the shortest distance between a station and the target grid cell, and counting the total number of cells that do not possess orientations within one compass point of that of the target grid cell ($\Delta f>1$), c is the facet weighting exponent (0/1.5/2) in mountainous coastal regions c is typically set at about 1.5 to 2 because of the sharp rain shadows that occur on leeward side of coastal mountains in inland and relatively flat regions, where rain shadow is less pronounced, a value of 1.5 or less will suffice.

A station is considered to be on the same facet as the target grid cell and receives full weight if it meets 2 conditions;

1) It resides on a cell that has a terrain orientation within one compass point of the target cell (checked by Δf)

2) The stations cell is located within the same group of similarly-oriented cells or facet as the target cell (checked by B)

The same mountain slope can be defined if $\Delta f=1$ and $B=0$ meaning stations are on the same facet as target cell. On the other hand different mountain ranges can be defined if $\Delta f=1$ and $B>0$ meaning same orientation but on completely different group of similarly oriented grid cells (Daly et al, 2002).

- Coastal Proximity Weight (W_p): It is used to define gradients in precipitation that may occur due to proximity to large water bodies. Stations with coastal proximities similar to that of the target grid cell are assigned relatively high weights.

  For smooth terrains, coastal proximity grid for precipitation was composed simply of distances form the generalized coastline grid. A simple distance is enough since lack of terrain features. The generalized coastline is used since bays and inlets were not considered to be as important moisture sources as open ocean for precipitation.

For complex terrain a simple trajectory model was designed to assess relative moisture availability to guide precipitation mapping. The trajectory model is similar to the coastal advection model in that it accounts for changes in moisture content due to path length and terrain effects. It differs in that the air parcel trajectories are straight line and invariant throughout the simulation, as might be the case within large-scale synoptic circulations that produce significant precipitation. The premise here is that mean potential for precipitation experienced at a site is the result of;

- Loss of moisture throughout rainout, which accumulates as the path length over land increases
- Enhancement and suppression of precipitation caused by adiabatic cooling and warming during flow over terrain obstacles.

To begin the simulation, ocean pixels along the coastline were assigned a 'precipitation index' (PI) score of zero. The original unfiltered DEM is used.

$$PI_n = PI_{n-1} + t_{up} + t_{down} + p \qquad (3.7)$$

where, n-1: adjacent upstream pixel

t_{up} and t_{down}: terrain penalties for uphill and downhill flow paths respectively

p: precipitation path length for each pixel travelled.

$$t_{up} = -0.1h \qquad (3.8)$$

$$t_{down} = 0.3h \qquad (3.9)$$

$$p = 0.5/pixel \qquad (3.10)$$

where, h: terrain height difference in meters between a pixel and its upstream neighbor. Positive h denotes upslope conditions.

$$W_p = \begin{Bmatrix} 1;\ \Delta p = 0 \\ 0;\ \Delta p > p_x \\ \frac{1}{\Delta p^v};\ 0 < \Delta p \leq p_x \end{Bmatrix} \qquad (3.11)$$

where, Δp: absolute difference between station and target grid cell coastal proximity index

v: coastal proximity weighting exponent typically set to 1

p_x: maximum coastal proximity difference (varies with application).

- Effective terrain weight (W_e): Using 2.5 min DEM an effective terrain height grid was prepared by
    - Finding the minimum elevation within a approximately 40-km radius of each grid cell
    - Spatially averaging the minimum elevations over a 40-km radius to smooth "base" elevation grid
    - Subtracting the base elevation grid from the original DEM grid to get an effective terrain height grid
    - Spatially averaging the effective terrain height grid across a 20-km radius to produce a smooth grid

    PRISM uses the effective terrain grid in a multi-step process. A 3D index for the target grid cell (I_{3c}) is determined by comparing the effective terrain height of the target cell with thresholds for 2D and 3D model operation. If the effective terrain height exceeds the 3D threshold, I_{3c} is set to 1. If effective terrain height is less than the 2D threshold, I_{3c} is set to 0.

$$I_{3c} = \begin{Bmatrix} 1; & h_c \geq h_3 \\ \frac{h_c - h_2}{h_3 - h_2}; & h_2 < h_c < h_3 \\ 0; & h_c \leq h_2 \end{Bmatrix} \qquad (3.12)$$

where, h_c: effective terrain height for the target grid cell,

h_2 and h_3: user defined thresholds for 2D and 3D operations

If I_{3c}<1 signaling 2D or 2D/3D mixed situation, I_{3a}, an areal 3D index, is calculated to assess whether the target grid cell is near a significant 3D terrain feature.

$$I_{3a} = \begin{cases} 1; & h_a \geq h_3 \\ \frac{h_a - h_2}{h_3 - h_2}; & h_2 < h_a < h_3 \\ 0; & h_a \leq h_2 \end{cases} \qquad (3.13)$$

where, h_a: distance-weighted effective terrain height

h_i: effective terrain height for grid cell i

n: number of grid cells within 100 km of target grid cell

d_i: horizontal distance between the center of the target grid cell and nearby grid cell i

$$h_a = \frac{\sum_{i=1}^{n} w_i h_i}{n} \qquad (3.14)$$

$$w_i = \frac{1}{d_i} \qquad (3.15)$$

The final 3D index is expresses as;

$$I_{3d} = \max[I_{3c}, I_{3a}] \qquad (3.16)$$

A scalar form 0 to 1, I_{3d} represents the degree of importance terrain should play in the estimation of precipitation. When I_{3d}=1, the PRISM regression function operates in its normal fashion. When I_{3d} is zero, the slope of the precipitation/elevation regression function is forced to zero and stations are weighted by distance and clustering only resulting 2D interpolation. Effective terrain weight requires that I_{3d} be calculated for each station. This is done by calculation I_{3d} for the pixel on which a station resides in exactly

the same manner as was described in the previously for the target grid cell. The effective terrain weight is then given as,

$$W_t = \begin{cases} 1; & I_{3dc} = 1 \\ \frac{1}{(100|I_{3dc} - I_{3ds}|)^{0.5(1-I_{3dc})}}; & 0 \le I_{3dc} \le 1 \end{cases} \qquad (3.17)$$

where, I_{3dc} and I_{3ds}: effective terrain indices of the target cell and station

When I_{3dc}=1 target grid cell is 3D W_t becomes 1 and all stations are weighted equally. When I_{3dc} falls towards zero (2D situation) 3D stations are down-weighted. The down-weighting exponent increases to 0.5 as I_{3dc} approaches zero. When I_{3dc}=0 3D stations are down-weighted by a factor of one hundred compared to 2D stations (Daly, 2002).

These physiographic descriptors are controlled by a set of parameters. Daly et al (2002) suggests default values for many of these parameters; however the values of a few parameters are highly region dependent. In this study the values of these region dependent parameters (F_d, Δ_{zm}, Δ_{zx}, c, p_x, h_2, h_3) were selected via an optimization procedure. In the optimization procedure, each rain gauge station is removed, one-at-a-time, from the dataset and the precipitation value for that station is estimated via the remaining stations using the PRISM approach. The Shuffled Complex Evolution (SCE) algorithm (Duan et al. 1992) is then used to minimize the mean square error between PRISM-estimated and observed monthly precipitation values for all stations. This procedure was used to estimate the seasonal (winter [DJF], spring [MAM], summer [JJA] and autumn [SON]) PRISM-parameters separately for Region 1 and Region 2.

A comparison of the performance of the optimized PRISM-parameters and the default PRISM-parameters indicated that the optimization procedure increased the agreement between the observed and PRISM-estimated precipitation. As mentioned earlier, TMPA-7A product incorporates four of the GPCC stations located in the study area in precipitation estimation. Hence to minimize this bias during the evaluation process, these four stations should not be used in the PRISM-parameter estimation process. However, two of these GPCC stations (KST and INB) are located in data sparse regions and their

observations are deemed critical for the reliability of the estimation procedure and hence included in the PRISM approach. The other two GPCC stations (BOL and ZNG) were not used in the estimation of gridded precipitation via PRISM approach and left for independent data for evaluation. Table 3 lists the correlation coefficient and mean absolute bias statistics calculated using monthly precipitation observations from independent rain gauges and PRISM-estimated monthly precipitation values using default and optimized parameters. It can be seen that the optimized PRISM parameters provided slightly improved statistics even for these independent rain gauges.

Table 3 Evaluation of the PRISM monthly precipitation estimates with default and optimized parameters using observed precipitation from independent rain gauges.

Station ID		**Season**	**Monthly Correlation Coefficient**	**Mean Absolute Bias (mm/month)**
ZNG (Region 1)	Default Parameters	Winter	0.95	16.2
		Spring	0.79	25.86
		Summer	0.69	33.66
		Autumn	0.97	19.29
	Optimized Parameters	***Winter***	***0.95***	***14.53***
		Spring	***0.80***	***24.83***
		Summer	***0.70***	***33.06***
		Autumn	***0.97***	***19.66***
BOL (Region 2)	Default Parameters	Winter	0.96	8.76
		Spring	0.59	14.72
		Summer	0.68	21.64
		Autumn	0.94	12.36
	Optimized Parameters	***Winter***	***0.96***	***8.77***
		Spring	***0.65***	***13.74***
		Summer	***0.70***	***20.54***
		Autumn	***0.95***	***10.25***

The optimized PRISM parameters were then used to interpolate the precipitation values for each 0.05^o x 0.05^o grid within the study area at the daily timescale assuming monthly PRISM parameters are also valid for the daily time scale. PRISM interpolated grids were further coarsened to 0.25^o resolution via box-averaging technique (Fig. 14). The Rain

gauge-based Gridded Precipitation dataset will be referred hereafter as “RGP”. Figure 14 shows the 5-year mean annual precipitation values obtained from the RGP dataset and the rain gauge network. RGP dataset captures the sharp precipitation gradient caused by the mountain ranges well, with high precipitation values along the windward side of the mountains and low precipitation values on the leeward side.

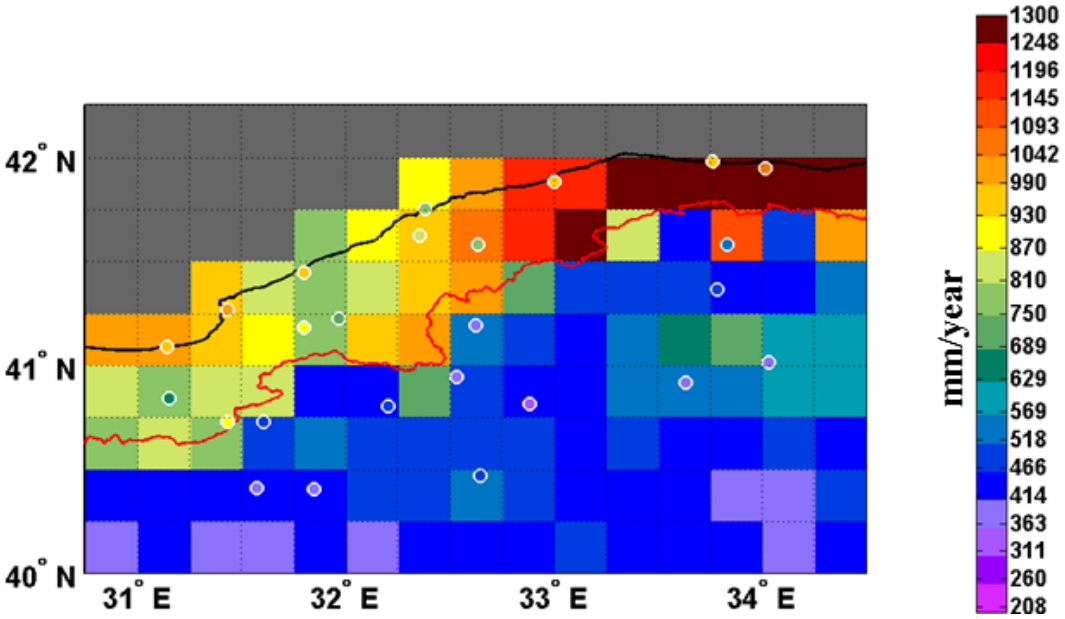

Figure 14 Rain gauge-based gridded precipitation dataset of mean annual precipitation for 2007-2011 period. Dots represent the rain gauges, their colors are representative of their mean annual precipitation for 2007-2011 period

3.2.3. Satellite-based Precipitation Products

SBP products that have been used in this study are explained in detail in Chapter 2.3.

3.3. Evaluation Methodology

The primary objective of this study was to evaluate the performance of various SBP products over complex topography using a rain gauge network. The evaluation was performed at various spatial scales. First, point-scale precipitation measurements from

the rain gauge network were compared with the co-located grid-scale precipitation estimates (0.25^{o}x0.25^{o}) from SBP algorithms. Second, the RGP product has been further utilized in the evaluation of the SBP products.

Based on data availability 2007-2011 period was selected. The evaluation methodology consisted of daily, monthly, seasonal and annual time scales. In the procedure, the daily time steps marked as "missing" for a single product has been removed from the analysis.

The agreement between different precipitation products were investigated using quantitative and categorical statistics as well as graphical tools such as scatter plots. The quantitative statistics include percentage bias (%BIAS), correlation coefficient (CORR) and normalized root-mean-squared error (NRMSE):

$$NRMSE = \left(\sqrt{\frac{\sum_{i=1}^{n}(SAT_i - RG_i)^2}{n}}\right) \Big/ \left(\frac{\sum_{i=1}^{n} RG_i}{n}\right) \quad (3.18)$$

$$\%BIAS = \left(\frac{\sum_{i=1}^{n} SAT_i - RG_i}{\sum_{i=1}^{n} RG_i}\right) * 100 \quad (3.19)$$

where, SAT: SBP products

RG: rain gauge gridded precipitation estimates

i=1, 2,…, n is the number of daily or monthly precipitation data pairs for each grid.

The contingency table-based categorical statistics measure the daily rain-detection capability and include false alarm ratio (FAR) and probability of detection (POD). These are based on a 2 x 2 contingency table (Table 4) [a: SAT yes, RG yes; b: SAT yes, RG no; c: SAT no, RG yes; and d: SAT no, RG no].

Table 4 2 x 2 contingency table

Gauge Observed Rainfall		Satellite-based precipitation products (SBP)	
		Rain (Yes)	No Rain (No)
	Rain (Yes)	(a) Hits	(c) Misses
	No Rain (No)	(b) False Alarms	(d) Correct negatives

The POD gives the fraction of rain events that were correctly detected and ranges from 0 to 1; 1 being the perfect score.

$$POD = \frac{a}{(a+c)} \qquad (3.20)$$

The FAR measures the fraction of rain events that were actually false alarms and ranges from 0 to 1; 0 being the perfect score.

$$FAR = \frac{b}{(a+b)} \qquad (3.21)$$

3.4. Results and Discussion

3.4.1. Comparison of Rain Gauge vs. Satellite-based Precipitation

To examine the influence of orography on the performance of the SBP products, cross section lines were taken along and perpendicular to the mountain ranges (Fig. 5). Figure 14 shows the annual precipitation from rain gauges and co-located SBP grids along cross section line 1 together with the topographic elevations. Note that cross section line 1 is perpendicular to the shore line; station BRT is in Region 1 (on the coast, windward side of the mountains) and other two stations are located in Region 2 (on the drier, leeward side of the mountains). Cross section lines 2 and 3 are taken along the coastal region (Region 1) and inland region (Region 2), respectively.

The influence of the orography on the precipitation distribution is clearly seen in Figure 15 with station BRT receiving significantly more mean annual precipitation (850.5 mm) compared to stations KRA (408.1mm) and CRK (344.2mm) located inland in Region 2. Along the coastal region (Region 1) all SBP products underestimate observed precipitation (Fig. 16a). In this region, TMPA-7A performs better than other products with slight underestimation possibly due to the monthly rain gauge correction procedure. CMORPH consistently and significantly underestimates the precipitation compared to rain gauges along the coast. MPE, on the other hand, shows underestimation with a wide range of scatter between years. TMPA-7RT underestimates along the coast, however with less annual bias compared to CMORPH.

In Region 2 (Fig. 15 & Fig. 16b) CMORPH provides consistent annual precipitation estimates compared to rain gauges with slight underestimation. Both TMPA-7A and TMPA-7RT products overestimate the observed precipitation in Region 2. The correction procedure employed within the TMPA-7A algorithm resulted in an improved product with less overestimation compared to the TMPA-7RT product.

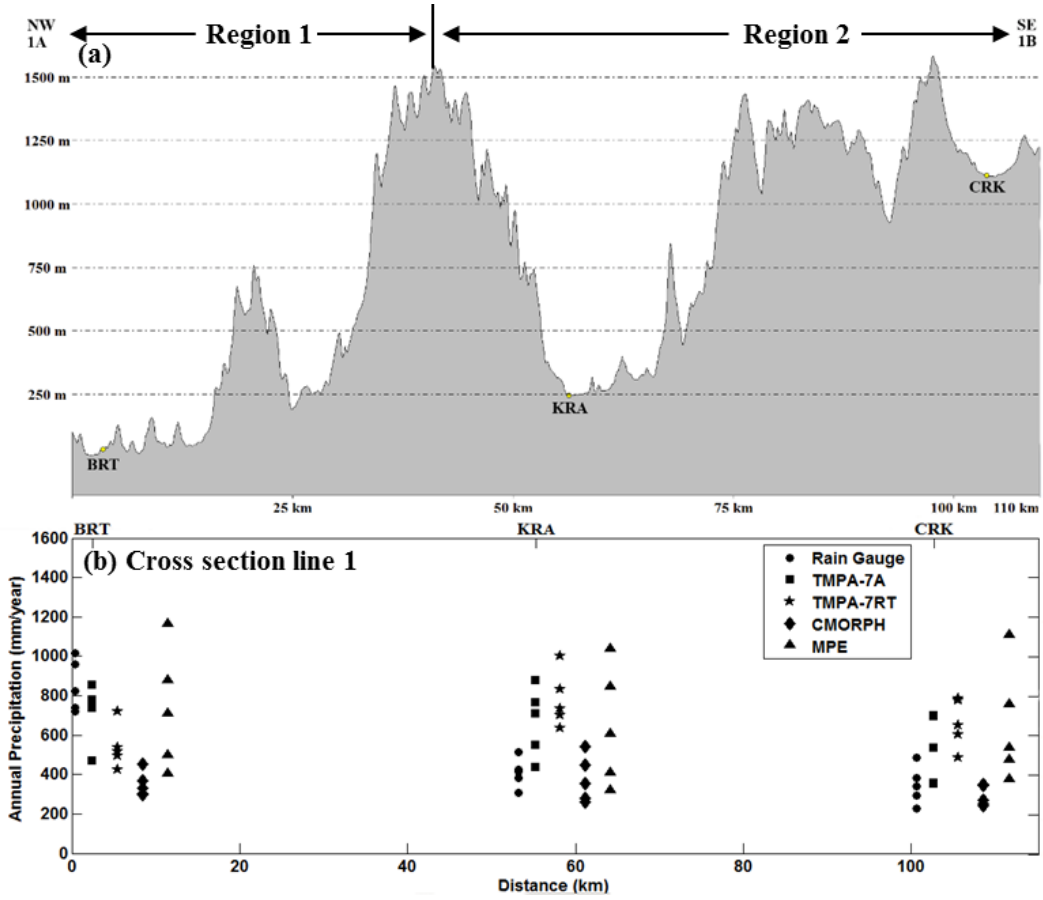

Figure 15 (a) Topographic elevations, (b) annual precipitation for each SBP product and rain gauge along cross section line 1.

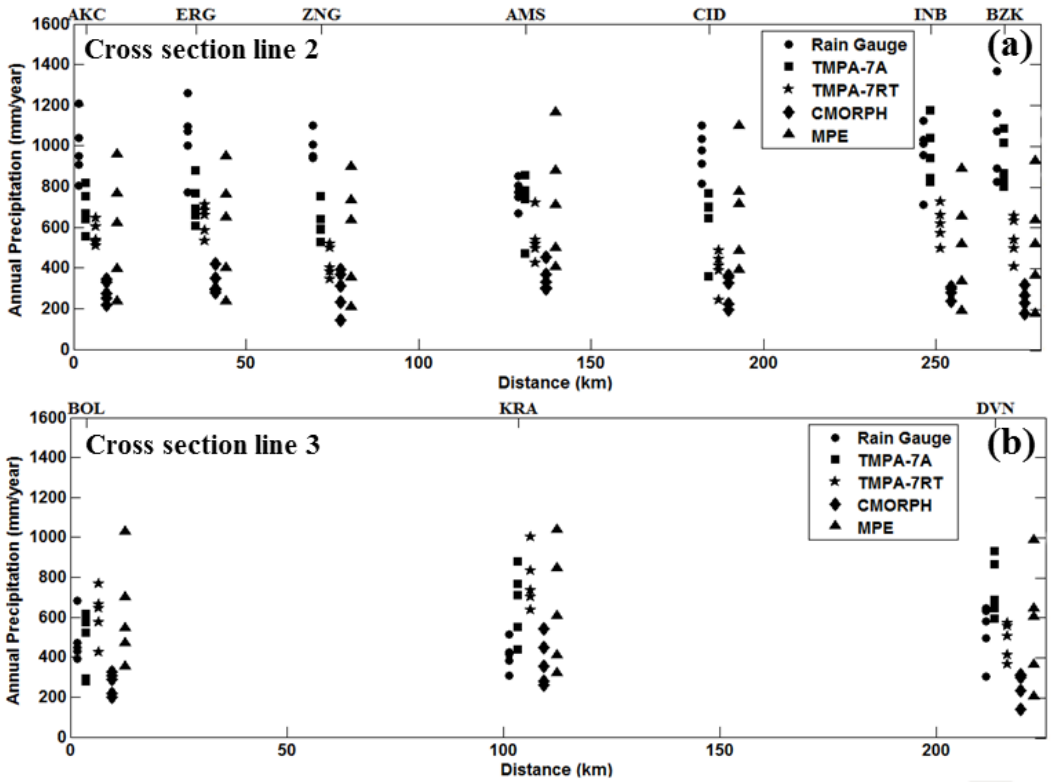

Figure 16 Annual precipitation for each SBP product and rain gauge along (a) cross section line 2 and (b) cross section line 3.

The maps in Figure 17 show the 5-year (2007-2011) mean annual precipitation values estimated by each SBP product at 0.25^0 spatial resolution together with the point-scale observations from the rain gauge network. Note that the region divide is shown by a red line. Starting with the TMPA-7RT product, it can be seen that the precipitation estimates are significantly less along the shoreline and significantly more inland compared to the rain gauges. Underestimation by TMPA-7RT and CMORPH along the shoreline is possibly due to the precipitation detection problems over water-land mixed cells (Huffman et al. 2007). TMPA-7RT produces heterogeneous precipitation estimates marked by sharp change in precipitation amounts in neighboring cells which may be caused by direct replacement of PMW-calibrated IR estimates with PMW estimates whenever the latter is available. This behavior will be investigated in more detail in section 3.4.3. In TMPA-7A product, the gauge-based correction procedure seems to work

well and improved the precipitation estimates with less significant underestimation along the shoreline and less significant overestimation inland. While it can be seen that the TMPA-7A precipitation estimates decrease as going from shoreline towards inland, as expected, the precipitation gradient is not as sharp as characterized by the rain gauges and marked by the region divide. CMORPH precipitation estimates are significantly lower and more uniform over the study area compared to other SBP products, thus underestimating the orographic precipitation along the shore more significantly compared to other products. In Region 2 the CMORPH precipitation estimates are more consistent with the rain gauge observations compared to other SBP products. While TMPA and CMORPH products show precipitation patterns with north-south gradients (although with varying magnitudes) over the study region at the mean annual time scale, spatial pattern of the MPE product differs with a decreasing precipitation trend from east to west. MPE product is characterized by underestimation in Region 1 and overestimation in Region 2.

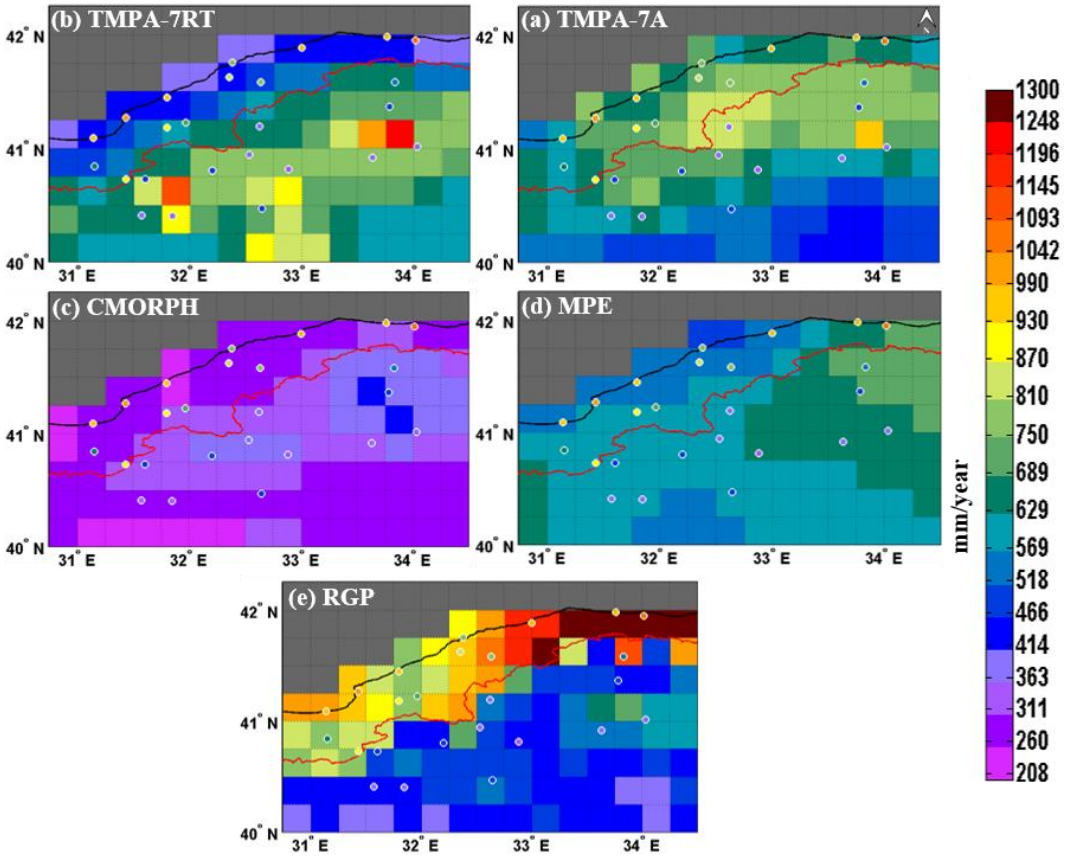

Figure 17 Spatial maps of 5 year (2007-2011) mean annual precipitation at 0.25^0 spatial resolution over study area (a) TMPA-7A, (b) TMPA-7RT, (c) CMORPH, (d) MPE, (e) RGP. Note that gray cells are over the sea.

To investigate the performance of the SBP products in a more detailed manner, Figure 18 shows comparison of monthly precipitation from two region-representative rain gauges and their co-located SBP grids using scatterplots and quantitative statistics for cold (September-February, black-circle markers) and warm (March-August, gray-triangle markers) seasons. Note that station AMS is located in Region 1 and station DVN is located in Region 2. These scatterplots show that CMORPH (more significantly) and MPE products suffer from a precipitation detection problem (points are scattered along the x-axis) in Region 1 during cold season. On the other hand TMPA-7RT and TMPA-7A provide better monthly precipitation estimates for both regions and seasons. TMPA-7RT resulted in underestimation in Region 1 and slight overestimation in Region 2 during

winter. TMPA-7A resulted in improved precipitation estimates compared to TMPA-7RT in both Regions, the only exception being the overestimation in Region 2 winter season.

In summary gauge-corrected TMPA-7A outperforms satellite-only SBP products at the monthly time scale as expected. Satellite-only SBP products generally suffer from precipitation detection problem in Region 1 during cold season, CMORPH being more and TMPA-7RT being less significant. In Region 2 all SBP products overestimate monthly precipitation regardless of the season (more significantly during winter), the only exception being CMORPH.

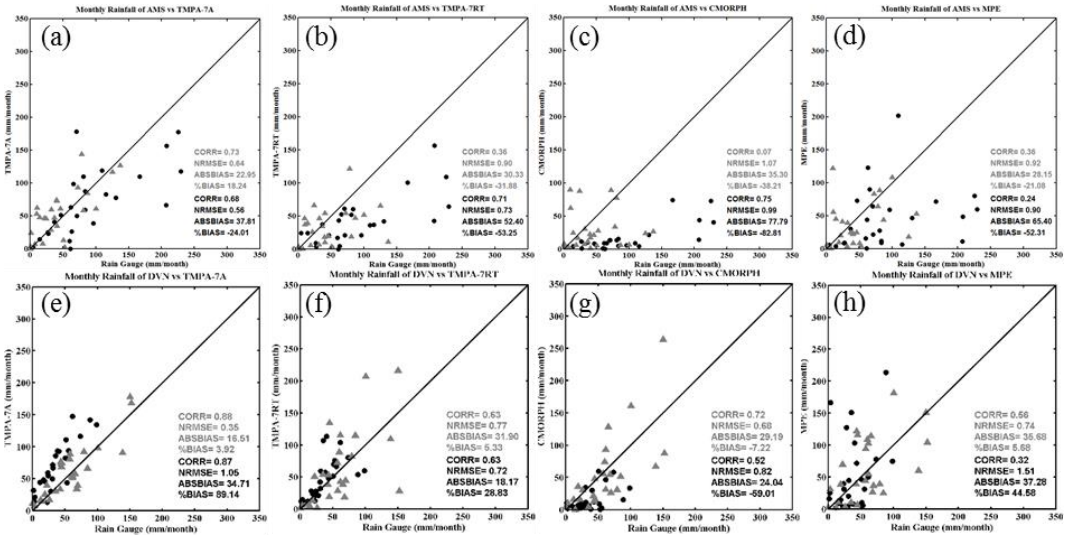

Figure 18 Monthly scatterplots of rain gauge observations vs. four SBP products over 2007-2011 during cold and warm seasons. Stations AMS (in Region 1) vs. (a) TMPA-7A, (b) TMPA-7RT, (c) CMORPH, (d) MPE, Station DVN (in Region 2) vs. (e) TMPA-7A, (f) TMPA-7RT, (g) CMORPH, (h) MPE. Note that the data points in triangle (circle) and statistics in gray (black) color are for warm (cold) season.

Comparison of daily precipitation from two region-representative rain gauges and their co-located SBP grids (Fig. 19) indicate deteriorated SBP performance (marked by a wide scatter) compared to monthly time-scale. The points located along x-axis and y-axis show missed and falsely detected daily precipitation events respectively, which are specifically important if these products will be used in modeling of floods. The underestimation of

precipitation by CMORPH in Region 1 (Fig. 19c) is mostly due to the consistently missed daily precipitation events especially during cold season. In Region 2, however, CMORPH shows improved performance as indicated by the statistics and by the points located closer to the diagonal 1:1 line. MPE product, although properly detected a few high daily precipitation events, suffers from significant false detection and missed events in both regions and seasons. TMPA-7RT product suffers from precipitation detection problem whereas TMPA-7A showed falsely detected high daily precipitation estimates in Region 1 during cold season. In Region 2 both TMPA products overestimate daily precipitation regardless of the season.

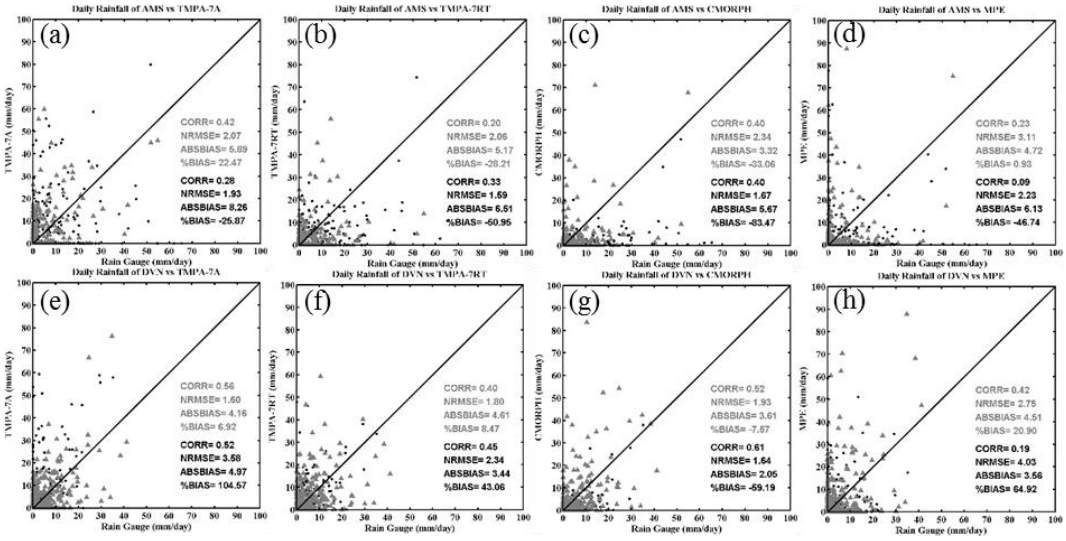

Figure 19 Daily scatterplots of rain gauge observations vs. four SBP products over 2007-2011 during cold and warm seasons. Station AMS (in Region 1) vs. (a) TMPA-7A, (b) TMPA-7RT, (c) CMORPH, (d) MPE, and Station DVN (in Region 2) vs. (e) TMPA-7A, (f) TMPA-7RT, (g) CMORPH, (h) MPE. Note that the data points triangle (circle) and statistics in gray (black) color are for warm (cold) season.

3.4.2. Comparison of Rain gauge-based Gridded Precipitation (RGP) vs. Satellite-based Precipitation

Figure 17e shows the 5-year mean annual precipitation values obtained from the RGP dataset (Section 3.2.2) and the rain gauge network. RGP dataset captures the sharp

precipitation gradient caused by the mountain ranges well, with high precipitation values along the windward side of the mountains and low precipitation values on the leeward side.

Box plot in Figure 20 shows summary statistics calculated by comparing monthly precipitation estimates from RGP grids and their co-located SBP grids located in Region 1 and Region 2 during cold and warm seasons. In these box plots horizontal lines are 25^{th} and 75^{th} percentiles and median of the distribution, vertical lines represent the extent of the rest of the data which is 1.5 times the 25^{th}-75^{th} percentile range and outliers are represented by '+' markers. In general TMPA-7A, TMPA-7RT and MPE products underestimate (negative %Bias) precipitation in Region 1 and overestimate (positive %Bias) precipitation in Region 2 regardless of the season. CMORPH results in more than 50% underestimation in both regions in cold season. In warm season CMORPH is characterized by underestimation in Region 1 and slight underestimation in Region 2. Among satellite-only SBP products TMPA-7RT shows better CORR with the RGP dataset in both regions and seasons. TMPA-7A performance is superior compared to satellite-only products in terms of CORR and NRMSE statistics possibly due to the monthly correction procedure.

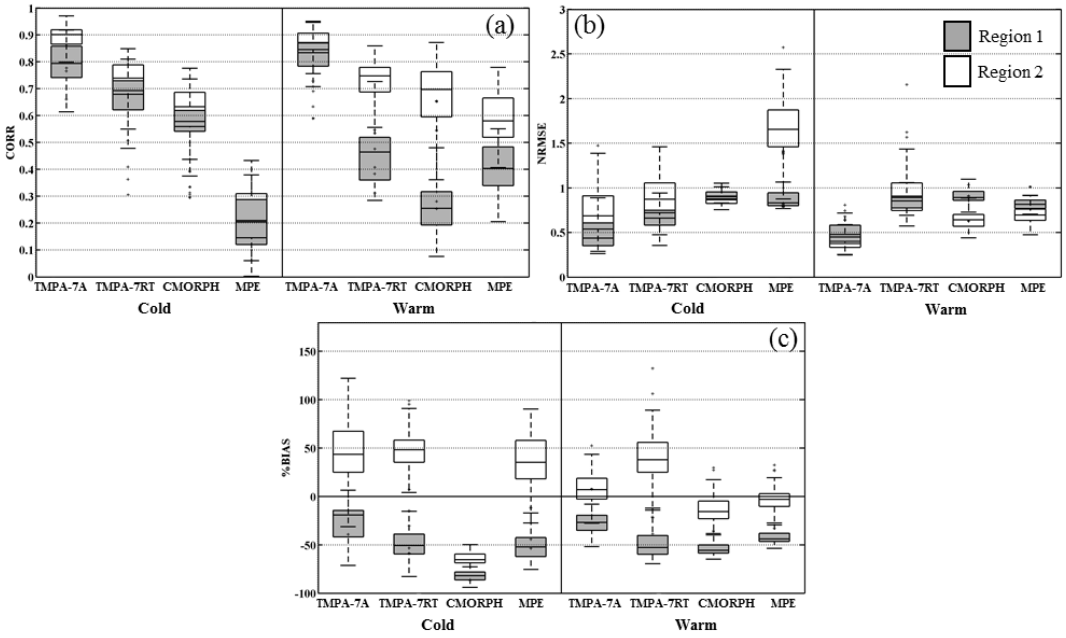

Figure 20 Monthly statistical results (a) CORR, (b) NRMSE and (c) %BIAS for RGP grids in Region 1 (Gray box) and Region 2 (White box) and their corresponding co-located SBP product grids during cold and warm seasons.

Focusing on the daily time scale (Fig. 21) it can be seen that the performance of the SBP products diminishes significantly. A general observation is that among all the SBP products MPE shows the lowest performance in terms of CORR and NRMSE statistics. TMPA-7A shows a general improvement in performance compared to TMPA-7RT. CMORPH produced highest CORR and lowest NRMSE statistics in Region 2 during cold season which is possibly due to the surface snow and ice screening process embedded in the algorithm (Joyce et al. 2004, Xie et al. 2007), however a significant negative %BIAS is evident. Overall, CMORPH shows the best daily statistics in Region 2 in both seasons with the exception of the significant negative bias in cold season. All SBP products underestimate RGP in Region 1 and overestimate RGP in Region 2 regardless of the season; CMORPH being an exception shows underestimation in both regions and seasons. The %Bias values during cold season ranges between -20% (TMPA-7A) and -82% (CMORPH) in Region 1, and between +60% (TMPA-7RT) and -64% (CMORPH) in Region 2. The %Bias values during warm season ranges between -22% (TMPA-7A)

and -54% (CMORPH) in Region 1, and between +40% (TMPA-7RT) and -15% (CMORPH) in Region 2. Note that the performance of the TMPA-7A, TMPA-7RT and MPE products over Region 2 is deteriorated more significantly in cold season compared to warm season possibly due to surface snow cover contamination.

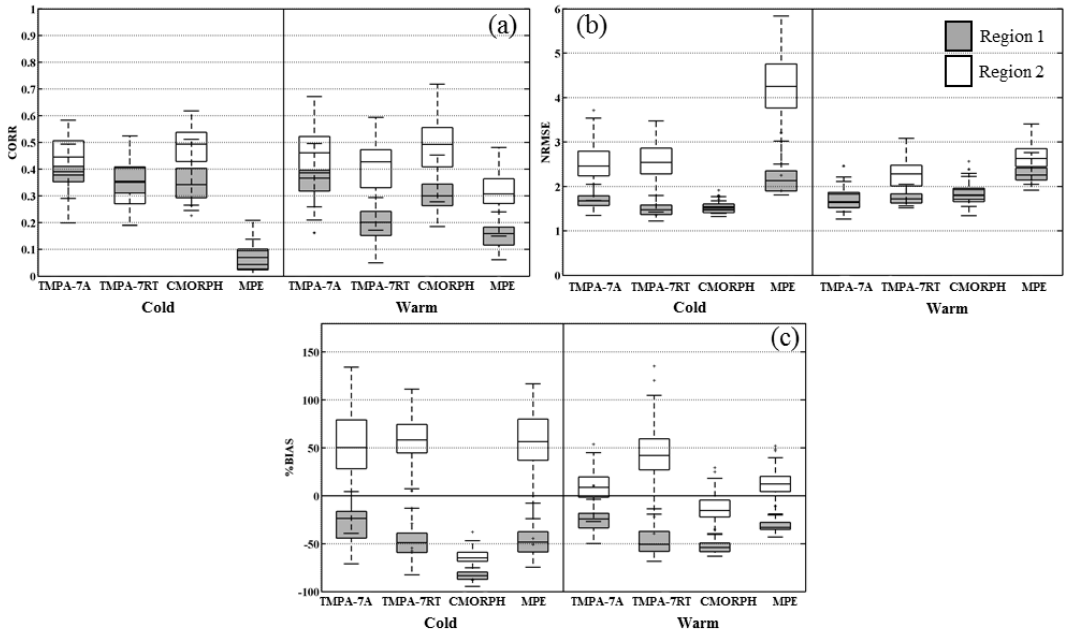

Figure 21 Daily statistical results (a) CORR, (b) NRMSE and (c) %BIAS for RGP grids in Region 1 (Gray box) and Region 2 (White box) and their corresponding co-located SBP product during cold and warm seasons.

Figure 22a and 22b compare respectively, the frequency of light precipitation (1-3mm/day) and heavy precipitation (10-20mm/day) reported by RGP and SBP products. These threshold values were selected based on an analysis of daily RGP precipitation distribution in both regions. While 1-3mm/day interval is a good representation of light precipitation in the study area, 10-20mm/day interval represents heavy precipitation events with significant number of occurrences. Focusing on the light precipitation detection capability, it can be seen that TMPA-7RT underestimates the number of days with light precipitation in Region 1 regardless of the season. The correction algorithm

employed in TMPA-7A further deteriorates this situation. In Region 2, TMPA-7RT slightly underestimates the number of days with light precipitation in both seasons. Again TMPA-7A further deteriorates this situation in cold season and had minor improvement in warm season. CMORPH product slightly underestimated the number of days with light precipitation in cold season regardless of region and resulted in similar light rain frequency with RGP dataset in warm season. The number of days with light rain reported by MPE product is consistent with the RGP dataset regardless of region and season.

Focusing on the heavy precipitation events (Fig. 22b), it can be seen that RGP dataset reported significantly more number of days with heavy precipitation in Region 1 compared to Region 2 in cold season whereas SBP products fail to discriminate this behavior. CMORPH reported significantly less number of days with heavy precipitation compared to RGP dataset and other SBP products regardless of the region and season. TMPA products significantly overestimated the number of days with heavy precipitation in Region 2 and underestimated the number of days with heavy precipitation in Region 1 regardless of the season. However, TMPA products showed the best performance among SBP products in detecting heavy precipitation in Region 1. In general MPE product reported similar number of days with heavy precipitation with RGP dataset in Region 2 while underestimated the number of days with heavy precipitation in Region 1.

It can be seen that CMORPH product suffers from heavy precipitation detection in Region 1 especially in cold season; this behavior can be partly attributed to the morphing algorithm; heavy precipitation events occurring in between infrequent PMW scans will likely be missed.

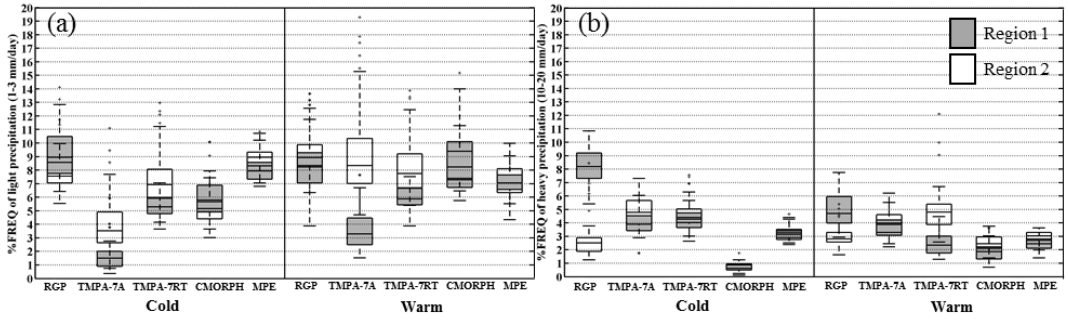

Figure 22 The frequency of (a) light precipitation (1-3 mm/day) and (b) heavy precipitation (10-20 mm/day) reported by RGP and by SBP products during cold and warm seasons.

Figure 23 shows the seasonal variation of categorical performance measures for precipitation magnitudes greater than 1 mm/day and for those greater than 9 mm/day. Note that the heavy precipitation threshold (9mm/day) is selected to ensure that the categorical measures for each grid combination is calculated based on at least 4 samples. It should be noted that POD and FAR are complementary measures and hence should be considered together to understand the performance trade-off between correctly detected observed precipitation and falsely estimated precipitation. In terms of precipitation detection, it can be seen from Figures 23a and 23b that CMORPH has the lowest POD performance (less than 0.3) among the SBP products in cold season indicating precipitation detection problems in both regions. Due to this detection problem CMORPH provided the best (lowest) FAR performance in cold season in Region 1 and Region 2. MPE precipitation estimates are characterized by low POD values varying between 0.30 and 0.45 in Region 1 and Region 2 respectively, followed by worst (highest) FAR values among the compared SBP products. TMPA-7RT showed the best (highest) POD performance in both seasons and regions (0.4 in Region 1 and 0.6 in Region 2) followed by poor (high) FAR values (0.35) in Region 2 and moderate FAR values (0.18) in Region 1. Therefore TMPA-7RT can be characterized by a detection problem (low POD and low FAR) in Region 1 and overestimation problem (high POD and high FAR) in Region 2. The correction procedure included in TMPA-7A deteriorated the POD performance while slightly improving the FAR performance compared to TMPA-7RT

product. Focusing on the warm season, an improvement in POD and FAR performance of all SBP products is evident compared to cold season for both regions. In warm season, MPE product is characterized by low POD and FAR performance compared to other SBP products. As a summary considered SBP products are characterized by varying degrees of precipitation detection problems in Region 1, which are more significant in cold season and they showed improved precipitation detection performance in Region 2 especially in warm season.

In terms of heavy precipitation (Fig. 23c and 23d) both CMORPH and MPE products show significant deterioration in POD performance in cold season. MPE further showed significant deterioration in FAR performance (FAR > 0.75) in both Regions in cold season. Evaluated SBP products are characterized by poor POD performance specifically in Region 1 and they are characterized by poor FAR performance specifically in Region 2 regardless of the season. TMPA products perform better than other SBP products in terms of detecting heavy precipitation; TMPA-7A outperforming others.

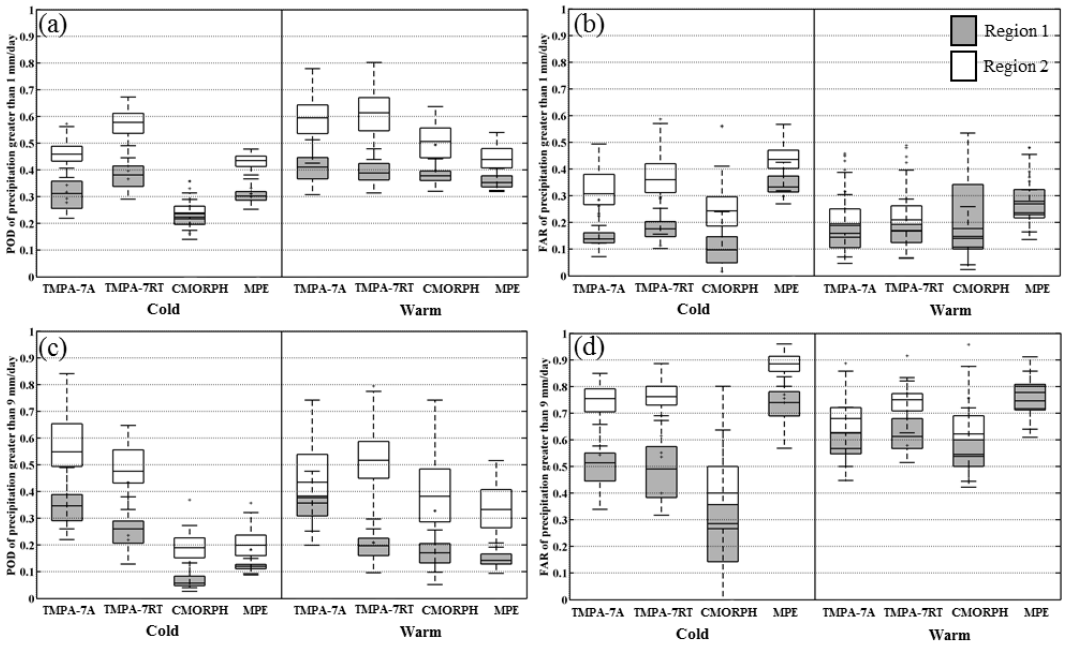

Figure 23 Categorical performance results for precipitation greater than 1 mm/day (a) POD, (b) FAR and for precipitation greater than 9mm/day (c) POD, (d) FAR during cold and warm seasons.

3.4.3. Comparison of 3B40RT, 3B41RT and MWCOMB

Since the datasets utilized in the development of these SBP products are different and have undergone various quality control procedures, caution is needed while evaluating the performance of these products. For example, TMPA-7RT algorithm produces rain rates by combining information from both MW and IR retrievals via a calibration procedure, whereas CMORPH produces rain rates solely from MW retrievals and propagates these temporally sparse retrievals via temporally rich IR retrievals. To investigate potential sources of errors in these algorithms, we further analyzed the IR and MW datasets used in developing these products. TMPA-7RT product combines MW-only and IR-based precipitation estimates, named as 3B40RT and 3B41RT respectively. 3B40RT is a merged microwave (Microwave Imager on TRMM (TMI), Advanced Microwave Scanning Radiometer-Earth Observing System (AMSR-E), SSM/I, Special Sensor Microwave Imager/Sounder (SSMIS), Advanced Microwave Sounding Unit-B (AMSU-B) and MHS) precipitation estimate averaged at 0.25^0x0.25^0 spatial and 3 hourly

temporal resolution. 3B41RT is an IR-based precipitation estimate that converts 0.25^0x0.25^0 averaged IR brightness temperature to precipitation rates via a local space-time calibration procedure incorporating high quality MW data. CMORPH product derives precipitation estimates at 0.25^0x0.25^0 spatial 3-hourly temporal resolutions by merging various microwave retrievals (TMI, SSM/I and AMSU-B) which are than propagated in space by cloud motion vectors derived from IR images. This merged microwave product is named as MWCOMB. In the procedure, the daily time steps marked as "missing" for a single dataset has been removed from the analysis. Note that, time steps used in this analysis are different from those used in Section 3.4.2 hence a comparison of the statistics between these two sections is not appropriate.

Figure 24 shows summary statistics calculated by comparing daily precipitation estimates from RGP grids and their co-located 3B41RT, 3B40RT and MWCOMB grids. It can be seen that the MW datasets used in TMPA and CMORPH products (3B40RT and MWCOMB respectively) perform very similar in cold season in both regions, indicated by CORR values less than <0.15, NRMSE values ranging between 1.5 and 2, and %BIAS values ranging between negative 75-100%. The IR dataset used in TMPA-7RT (3B41RT), shows similar CORR and NRMSE performance with the MW datasets in Region 1 during cold season with improved (less negative) %BIAS performance. In Region 2, however, 3B41RT shows higher performance in terms of CORR and %BIAS (also opposite sign with overestimation) and lower performance in terms of NRMSE (due to false alarms) as compared to MW datasets in cold season. In warm season, MW dataset used by CMORPH performs slightly better than that used by TMPA in terms of CORR and %BIAS, however performs slightly poorer in terms of NRMSE. It can be concluded that the performance of the MW and IR datasets are similar in warm season, moreover the performance of the IR dataset is generally better than MW dataset in cold season in Region 2. The uniform nature of underestimation by CMORPH in Region 2 can be attributed to the MW dataset used in the algorithm and spatially heterogeneous nature of TMPA-7RT product in Region 2 can be explained by the differences in precipitation rates produced by IR and MW datasets used in this algorithm.

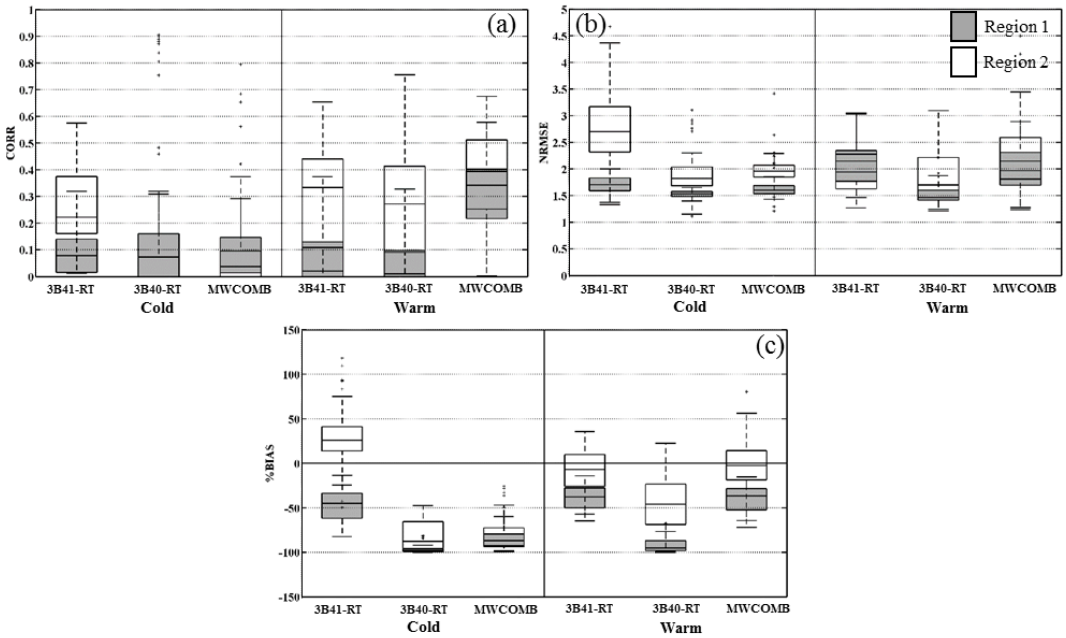

Figure 24 Daily statistical results (a) CORR, (b) NRMSE and (c) %BIAS obtained by comparing RGP grids in Region 1 (Gray box) and Region 2 (White box) and their corresponding co-located 3B41RT, 3B40RT and MWCOMB grids during cold and warm seasons.

CHAPTER 4

DEVISING A BIAS ADJUSTMENT METHODOLOGY FOR SATELLITE-BASED PRECIPITATION PRODUCTS

The objective of this chapter is to propose a bias adjustment methodology for SBP products over Western Black Sea Region of Turkey, which is characterized by complex topography. The effect of the complex topography on the performance of these products was studied in Chapter 3. Four different SBP products are evaluated: TMPA including experimental real time monitoring product and post real time research quality product; CMORPH and MPE (See Chapter 2 for detailed information). In Chapter 3 the results of the evaluation methodology indicated that considered SBP products are characterized by varying degrees of precipitation detection problems in windward region, which are more significant in cold season and they showed improved precipitation detection performance (high POD and low FAR) in leeward region especially in warm season. Noting these error characteristics of the SBP products, research problem addressed in this chapter is to adjust these products so that the performance of a hydrological model driven by these products would improve.

4.1. Introduction

Uncertainties in hydrologic predictions can be attributed to a large extent to errors in the precipitation products since precipitation is the main driver of the hydrologic system. Therefore, reliability and accuracy of any hydrologic study largely depends on realistic representation of the spatio-temporal distribution of precipitation (Segond et al. 2007). SBP measurements are quasi-global, high resolution and easily accessible however these

products have certain limitations that necessitates a bias adjustment or merging procedure using more accurate precipitation estimates. Limitations of the SBP products originates from the fact that they indirectly measure atmospheric characteristics and then interpret precipitation estimates with the help of different algorithms.

Bias definition depends on the defined error model. There are several error model descriptions, which are simply mathematical representation of measurement's deviation from observed data. According to Tian et al. (2013) two type of error models are commonly used for precipitation measurements: additive (Vila et al. 2009, AghaKouchak et al. 2012) and multiplicative (Hossain and Anagnostou 2006) error models.

Another important aspect of bias adjustment of SBP products is spatial distribution of results of the error model. This can be achieved by using several interpolation techniques.

We propose a bias adjustment algorithm for the SBP products based on the "physiographic similarity" concept which incorporates topographical and location specific variables in the bias adjustment process. The premise of the algorithm is that, the rain gauges within physiographically similar regions are grouped to calculate weights of the bias adjustment procedure rather than the rain gauges in proximity. In the literature weights of bias adjustment algorithm are mostly calculated based on proximity of rain gauges (Vila et al. 2009, Boushaki et al. 2009). However in topographically complex terrain two close stations might have different precipitation characteristics. Hence proximity concept does not work affectively in topographically complex terrain. Therefore, weights of the proposed bias adjustment algorithm is calculated based on the rain gauges within physiographically similar regions and bias adjustment further conducted by adding the weighted bias to the SBP product. Even though multiplicative scheme is suggested by Tian et al. (2013) to remove the daily bias, this methodology is not useful while determining the magnitude of precipitation when SBP product estimate is zero and observed precipitation magnitude is different than zero (Vila et al. 2009). The performance of the proposed bias adjustment algorithm is compared to inverse distance weighting (IDW) bias correction algorithm which is selected as the "baseline model". We will conclude this chapter with a discussion of the utility of satellite-based precipitation

(SBP) algorithms as input to hydrologic models in topographically complex regions. The evaluation of the bias adjustment methodology is performed at multiple time and space scales using quantitative, categorical and graphical measures.

Present study differs from and complements previous studies in several aspects. First the study area is characterized by a complex topography with significant orographic precipitation and a distinct rain-shadow effect. Second the bias adjustment is based on a gridded rain gauge dataset constructed using the "physiographic similarity" concept which is well-suited to regions with complex topography. Third, the TMPA products (TMPA-7RT and TMPA-7A) are retrospectively processed by the algorithm developers with the latest algorithm hence the performance of these new products having uniform temporal error characteristics are presented.

4.2. Error Models for Precipitation Measurements

4.2.1. Additive Error Model

Additive error model is defined in its simplest form as;

$$Y_i = a + bX_i + \varepsilon_i \qquad (4.1)$$

where, i: index of a datum

X_i: reference data

Y_i: measurement

a: offset (determine systematic error)

b: scale parameter to represent the differences in the dynamic ranges between reference data and the measurement (determine systematic error)

ε_i: instance of the random error which has zero mean and variance of σ^2 (Tian et al. 2013)

4.2.2. Multiplicative Error Model

Multiplicative error model is defined in its simplest form as;

$$Y_i = aX_i^b e^{\varepsilon_i} \quad (4.2)$$

where, e^{ε_i}: multiplicative factor with mean of ε_i being zero and the variance σ^2 (Tian et al. 2013)

Depending on the error model formulation for both additive and multiplicative models, values of σ will be different from each other. However, error definition for both models can be summarized as the difference between measurements and observation for additive error model and ratio between the two for multiplicative error model.

4.3. Interpolation Algorithms

Spatial distribution of the precipitation is important for hydrological studies. If only a single rain gauge is used to simulate flow of the basin, simulation would not be accurate at the basin scale (Segond et al 2007). Moreover, averaging the precipitation datasets restrict the accuracy of the hydrologic model compared to distributed model (Shah et al. 1996). Accurate representation of the spatial variability of precipitation is important since it affects the catchment response, peak flow time and model outputs. There are many different interpolation techniques to construct spatially distributed precipitation estimates, however the problem is to choose the correct method according to the study region and available data (Caruso et al. 1998). However, challenges in estimation of precipitation persist specifically over complex topography where precipitation is characterized by high spatio-temporal variability. In these regions, rain gauges are generally located in lowland due to accessibility considerations, thus under-representing the precipitation occurring high land that is of main interest in hydrologic studies.

Therefore interpolation of rain gauge observations generally results in underestimation of precipitation in topographically complex regions. Especially capturing the influence of orographic lifting on precipitation is difficult due to underrepresentation of gauge locations at high elevations (Adam et al. 2006).

Interpolation algorithms estimate a value at unsampled points based on weight of observed regionalized values (Ly et al. 2013)

$$Pr = \sum_{i=1}^{ns} \lambda_i RG_i \qquad (4.3)$$

where, Pr: interpolated precipitation value at required point

RG_i: observed precipitation value at point i

M: total number of rain gauges

λ_i: weight contributing to the interpolation

The main difficulty is calculating the weights, and interpolation methods mainly differ in this aspect. Weight estimation methods can generally be classified into two main groups as deterministic methods and geostatistical methods.

4.3.1. Deterministic Interpolation Methodologies

The most commonly used deterministic methods are Thiessen polygon (THI), Inverse Distance Weighting (IDW), spline interpolation and moving window regression method. THI method calculates its weight according to the distance and gives the highest weight to the closest stations proportion to the catchment area. Therefore this method is not suitable for topographically complex regions due to orographic influences (Goovaerts, 1999). IDW on the other hand calculates its weights again according to the distance however this time method uses inverse distance so that weights decrease as the distance increases. Weights are normalized so the sum equals one. If IDW is used along with elevation weighting method could be more suitable for topographically complex regions (Masih et al. 2011). Spline interpolation method fits a minimum-curvature surface to a specified number of nearest input points. Again this method is not suitable for

topographically complex regions (Ruelland et al. 2008). Finally moving window regression method is a linear regression method where precipitation is selected as primary variable and elevation as secondary variable. Therefore interpolation is based on relationship between precipitation and elevation.

4.3.2. Geostatistical Interpolation Methodologies

The most commonly used geostatistical interpolation method is kriging. Kriging interpolates observed values to a certain point by using weighted sum of available observed values. There are several types of kriging depending on the mean of the interest variable. If the mean is constant and known it is the simple kriging, if mean is constant but unknown the ordinary kriging and if mean is a polynomial function of spatial coordinates it is the universal kriging. System variables in the kriging equation can be determined in several ways. If mean locally varies and it is not constant it is Simple Kriging with locally varying mean (Goovaerts, 2000), if mean depends on auxiliary variables it is Kriging with External Drift (Hengl et al. 2003), if first order trends are removed using secondary variables by linear regression it is called residual kriging and finally if weighted linear combination of observations are used it is called ordinary kriging.

It is widely known that kriging interpolation is superior to IDW since estimates tend to be less biased as predictions are accompanied by prediction standard errors (Creutin and Obled (1982), Basistha and Goel (2007) and Diodata and Caccelelli, 2005).

4.4. Literature Review of Bias Adjustment of Satellite-based Precipitation Products

Most of the bias adjustment procedures assume rain gauge measurements are unbiased and SBP product contains useful information on spatial patterns of precipitation. It should also be noted that as with any modeling exercise, there is probably no unique way of representing error completely (Hossain and Huffman 2008). For example, TMPA-7A is bias adjusted against monthly GPCP precipitation product by locally defined adjustment

factors. Bias adjustment by rain gauge in real time is generally not possible because of the availability of gauge data and it should also be kept in mind that regional effects like topography play an important role in rainfall regime which can be smoothed at the monthly time scale.

Boushaki et al (2009) proposed a grid-based merging procedure to correct the bias in PERSIANN product by CPC daily gauge product. The procedure removes the weighted mean difference between the two products. On sub-daily scale methodology reduced bias and correlation but with limited improvement on the latter one. They concluded that in regions where rain gauge number is limited, improvement of SBP product depends on its own quality. Vila et al (2009) developed a methodology adjusting SBP products with daily gauge data. They used additive, multiplicative and combination of additive and multiplicative (CoSch) bias correction schemes. As a result, it is stated that CoSch method outperforms additive and multiplicative methods where CoSch can get more correct estimates in each defined category and the amount of false alarm estimated is smaller. It is also stated that CoSch tends to overestimate lower values and underestimate the larger values. Tian et al. (2010) on the other hand, train an algorithm by using Bayesian approach. Algorithm establishes a statistical relationship between SBP estimate and gauge measurements in historical time period. This learned relationship is then applied to real time SBP products when gauge data are not available. They concluded that this method works best for error corrections on seasonal scales or longer and it cannot improve performance metrics such as probability of detection or false-alarm ratio. Cheema and Bastiaanssen (2012) adjusted SBP products by using regression analysis and geographical differential analysis. They concluded that geographical differential analysis perform much better than regression analysis especially over mountainous regions. Hossain and Anagnostou (2006) developed two dimensional satellite rainfall model which generates ensembles of satellite rainfall fields. One of the strength of this algorithm is that, algorithm can improve missed rainfall and falsely detected rainfall by introducing rainfall in areas where SBP does not detect rain and correcting falsely detected rainfall.

It should be noted that several approaches suffer from a number of drawbacks. SBP products suffer from spatially varying, temporally changing and range dependent biases

that need to be adjusted. Errors in magnitude and temporal structure of rainfall should be adjusted since both factors are important for hydrological predictions. However error adjustment of magnitude of rainfall (PDF corrections) do not correct temporal structure of rainfall. Spatially varying errors are especially important for complex topography to represent orographic precipitation. Interpolation methodologies of reference data that bias adjustment is conducted affects spatially-explicit corrections adversely.

To sum up, it is stated that two error models can be used in bias adjustment of SBP products which are additive and multiplicative models. The result of these error models can be interpolated by using different weight calculations. Since the study area is a topographically complex region two nearby stations might have different precipitation characteristics. Therefore calculating the weights of the bias adjustment procedure based on proximity would not be accurate. Rather, assigning weights according to the physiographic similarities of the rain gauges should improve the results. Moreover, even though multiplicative scheme is suggested by Tian et al. (2013) to remove the daily bias, this methodology is not useful while determining the magnitude of precipitation when SBP product estimate is zero and observed precipitation magnitude is different than zero (Vila et al. 2009).

4.5. Study area & Datasets

Detailed information about study area and datasets used is provided in Chapter 1.2, Chapter 2.3 and Chapter 3.2 respectively.

4.6. Bias Adjustment Based on Physiographic Similarity (BAPS)

Proposed bias adjustment algorithm for the SBP products is based on “physiographic similarity” concept. The premise of the algorithm is that, the rain gauges within physiographically similar regions are grouped to calculate weights of the bias adjustment procedure rather than the rain gauges in proximity. Hence the proposed bias adjustment

algorithm methodology will be called bias adjustment based on physiographic similarity, or, “BAPS”.

In the PRISM approach the physiographic similarity between rain gauges and grids are represented by the PRISM weights, which are weighted combination of a set of physiographic variables (Section 3.2.2). These PRISM weights representing physiographic similarities are used in estimating the weight of the rain gauges in bias adjustment procedure. Bias adjustment will be conducted in 0.25^0 resolution; native resolution of satellite-based precipitation products. As explained in section 3.2.2 parameters of the PRISM approach were optimized for four different seasons. Therefore, weights adjustment vary as a function of both seasons and regions, in our effort to correct spatial and temporal errors in the SBP products. Note that the bias adjustment procedure is only utilized for the satellite-only SBP products (TMPA-RT, CMORPH and MPE), and TMPA-7A, which is already corrected by algorithm developers using GPCC rain gauge network, is not bias adjusted.

Bias of the SBP products are evaluated at every rain gauge location by subtracting SBP estimation from the rain gauge measurement. This point based bias values are then spatially distributed using the weights that we obtained from the PRISM approach. However weights are obtained from PRISM in 0.05^0 resolutions which need to be coarsened to 0.25^0 which is the native resolution of SBP products. Weights should be coarsened carefully while considering their physiographic properties.

For each 0.25^0 satellite-only SBP grid, precipitation is adjusted based on weighted difference between precipitation measurement from rain gauges and their co-located SBP grids. The adjustment weights are calculated by first grouping the 0.05^0 PRISM grids within a 0.25^0 SBP grid than sorting the PRISM weights assigned (Fig. 24) to every station (23 station) for estimation of the grouped PRISM grids. 50^{th} quantile (Q50) PRISM weight threshold is selected after trial and error process to exclude the insignificant PRISM weights within 0.25^0 window. In other words, the rain gauges with insignificant weight are located in regions that are physiographically not similar to the

region of interest. Later the bias adjustment weights are assigned to each rain gauge based on frequency of its occurrence within this Q50 range (Eqn. 5.1).

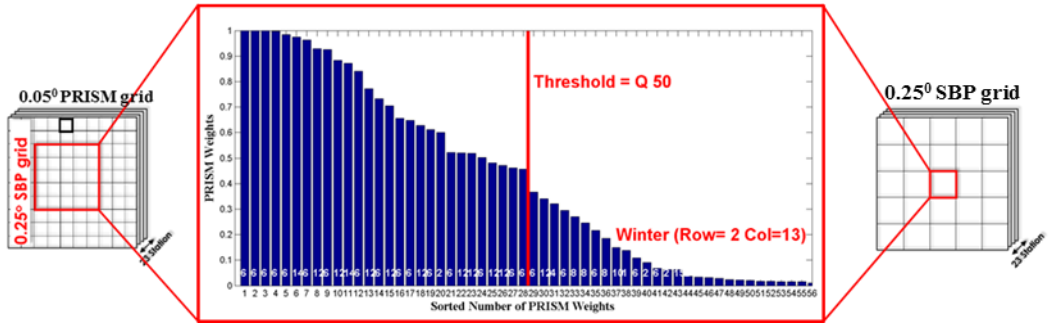

Figure 25 PRISM weight distribution for a 0.25^0 SBP grid.

$$w_{BAPS,in} = \frac{\#\ of\ RGin\ weights\ greater\ than\ Q50}{total\ \#\ of\ all\ \text{PRISM}\ weights\ greater\ than\ Q50} \quad (4.1)$$

where, $w_{BAPS,in}$: weight of rain gauge (RG) *i* for SBP grid *n* for BAPS methodology

Note that,

$$\sum_{i=1}^{M} w_{BAPS,i} = 1 \quad (4.2)$$

for each SBP grid.

where, M: total number of rain gauges (23)

Bias is calculated and distributed spatially as the weighted difference between rain gauges and their co-located SBP grids. Further these distributed bias values are added to the SBP to obtain adjusted SBP rainfall estimates (Eqn. 5.3 & Eqn. 5.4).

$$Bias_{BAPS,n} = \sum_{i=1}^{M} w_{BAPS,in}(RG_i - SBP_i) \quad (4.3)$$

$$BAPS\ Adjusted\ SBP_n = SBP_n + Bias_n \quad (4.4)$$

where, n: selected SBP grid (0.25^0)

We further compare this method with inverse distance weighted method (IDW) where weights are calculated as a function of inverse of the distance, *d*, between estimated grid (*n*) and reference rain gauge (*i*) (Eqn. 5.5, Eqn. 5.6 & Eqn. 5.7).

$$w_{IDW,in} = \frac{1}{d_{in}^2} \quad (4.5)$$

$$Bias_{IDW,n} = \sum_{i=1}^{M} w_{IDW,in}(RG_i - SBP_i) \quad (4.6)$$

$$IDW\ Adjusted\ SBP_n = SBP_n + Bias_n \quad (4.7)$$

where, $w_{IDW,in}$: weight of rain gauge *i* for the grid n for IDW methodology

4.7. Results and Discussion

Evaluation of the bias adjustment algorithm is initially, performed using two independent stations ZNG (Region 1) and BOL (Region 2). Cumulative precipitation of independent rain gauge stations ZNG and BOL, as well as satellite-only SBP products and bias adjusted SBP products are compared to understand the performance of BAPS and IDW bias adjustment methodologies (Fig. 26). Daily performance statistics are also provided in this figure. In general it is clear that all SBP products significantly underestimated the precipitation occurring in ZNG station and both BAPS and IDW bias adjustment algorithms improved the results. However, over the long term, it is clear that IDW algorithm underestimates ZNG station precipitation while BAPS algorithm performed better than the IDW algorithm, with less underestimation. For Station ZNG in Region 1, BAPS algorithm consistently provided better performance statistics compared to IDW method in cold season (Fig. 26 a, b, c) during which majority of the annual precipitation occurs (see Figure 3). In warm season, however, IDW algorithm seems to provide slightly improved statistics compared to BAPS algorithm, with the exception of the %BIAS statistic. It can be seen from these statistics that the large negative bias in the SBP products

is reduced more significantly by the BAPS algorithm. For station BOL in Region 2 (Fig. 26 d,e,f), both BAPS and IDW bias adjustment algorithms provided improved performance statistics compared to satellite-only SBP products. However, over the long term, IDW algorithm resulted in significant positive bias, even more than the SBP products, while BAPS algorithm resulted in slight underestimation as compared to the BOL station. The only exception is the TMAP-RT product for which, both IDW and BAPS algorithms significantly overestimating BOL station while failing to correct for the long term bias (see Fig. 26d). For BOL station during cold season, BAPS algorithm resulted in improved performance statistics NRMSE and %BIAS compared to IDW algorithm, while the latter provided better CORR statistic. In warm season, IDW algorithm showed improved performance in terms of CORR and NRMSE statistics as compared to BAPS algorithm, while the latter providing better %BIAS statistic. For BOL station, during warm period, BAPS algorithm was unable to improve the performance statistics over the satellite-only SBP products. Possible explanations for this situation could be the heterogeneous spatial distribution of the TMPA-RT SBP product due to direct replacement of IR estimates in to the product.

Inability of BAPS algorithm in improving CORR statistic shows similarity with the study of Boushaki et al. (2009) who reported that their algorithm was successful in improving RMSE and BIAS statistics however their CORR statistic did not show significant improvement as did the other statistics they have used.

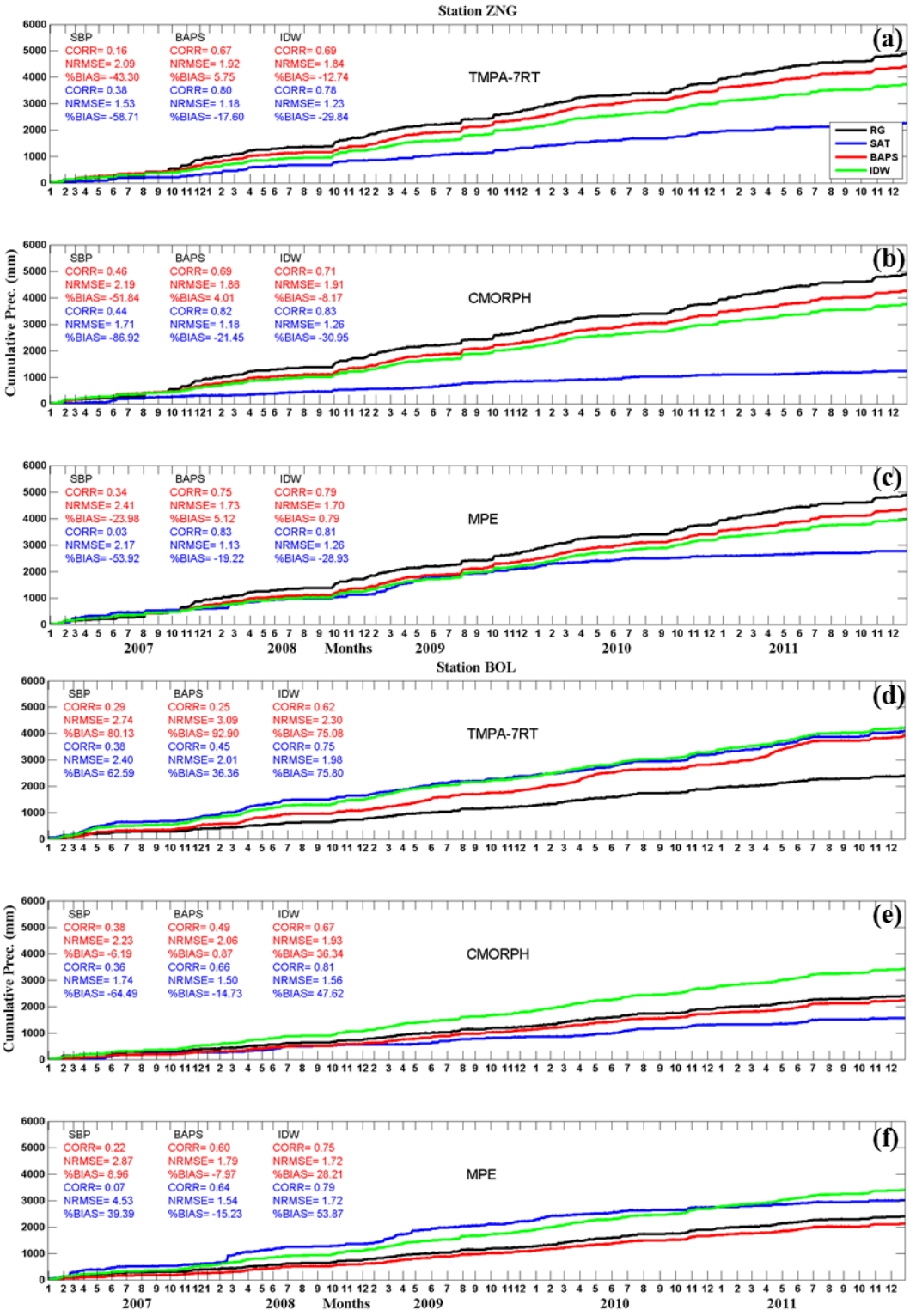

Figure 26 Cumulative precipitation of independent rain gauge stations (a, b, c) ZNG and (d, e, f) BOL, satellite-only SBP products and bias adjusted SBP products. Note that statistics in red represent warm season and blue represent cold season.

To investigate the performance of the SBP products before and after the BAPS and IDW bias adjustment process in a more detailed manner, Figure 27 and 28 shows comparison of daily precipitation from two independent stations ZNG (Region 1) and BOL (Region 2), respectively, and their co-located SBP grids before and after bias adjustment, using scatterplots and quantitative statistics for cold (September-February) and warm (March-August) seasons. In general these plots show that before bias adjustment at the daily timescale, there is a wide scatter between precipitation obtained from rain gauges and SBP products indicating poor performance. The points located along x-axis and y-axis show missed and falsely detected daily precipitation events respectively, which are specifically important if these products will be used to drive hydrologic models for flood estimation. It is clear from these plots that problems associated with missed and falsely detected daily precipitation are solved to a large extent with the proposed bias adjustment algorithm, as indicated by points scattered closer to the 1:1 line after the adjustment; for example, compare Figure 27 g & h. Notice that heavy precipitation generally occurring in cold season (circle markers) are largely missed by the satellite-only SBP products and bias adjustment algorithms were able to correct for these events. For station BOL (Fig. 28), TMPA-7RT significantly overestimates precipitation regardless of the season and neither of bias adjustment algorithms was able to correct this problem significantly. On the other hand underestimation problem by CMORPH in cold season (negative 64.49 %BIAS in Fig. 28d) is reduced to negative 14.73 %BIAS by BAPS algorithm while this underestimation is turned into positive 47.62 %BIAS overestimation by IDW algorithm. MPE showed significant amount of daily false precipitation which were corrected by both bias adjustment algorithms, however IDW further deteriorated the performance of the SBP product by significant overestimation while BAPS algorithm outperforms IDW.

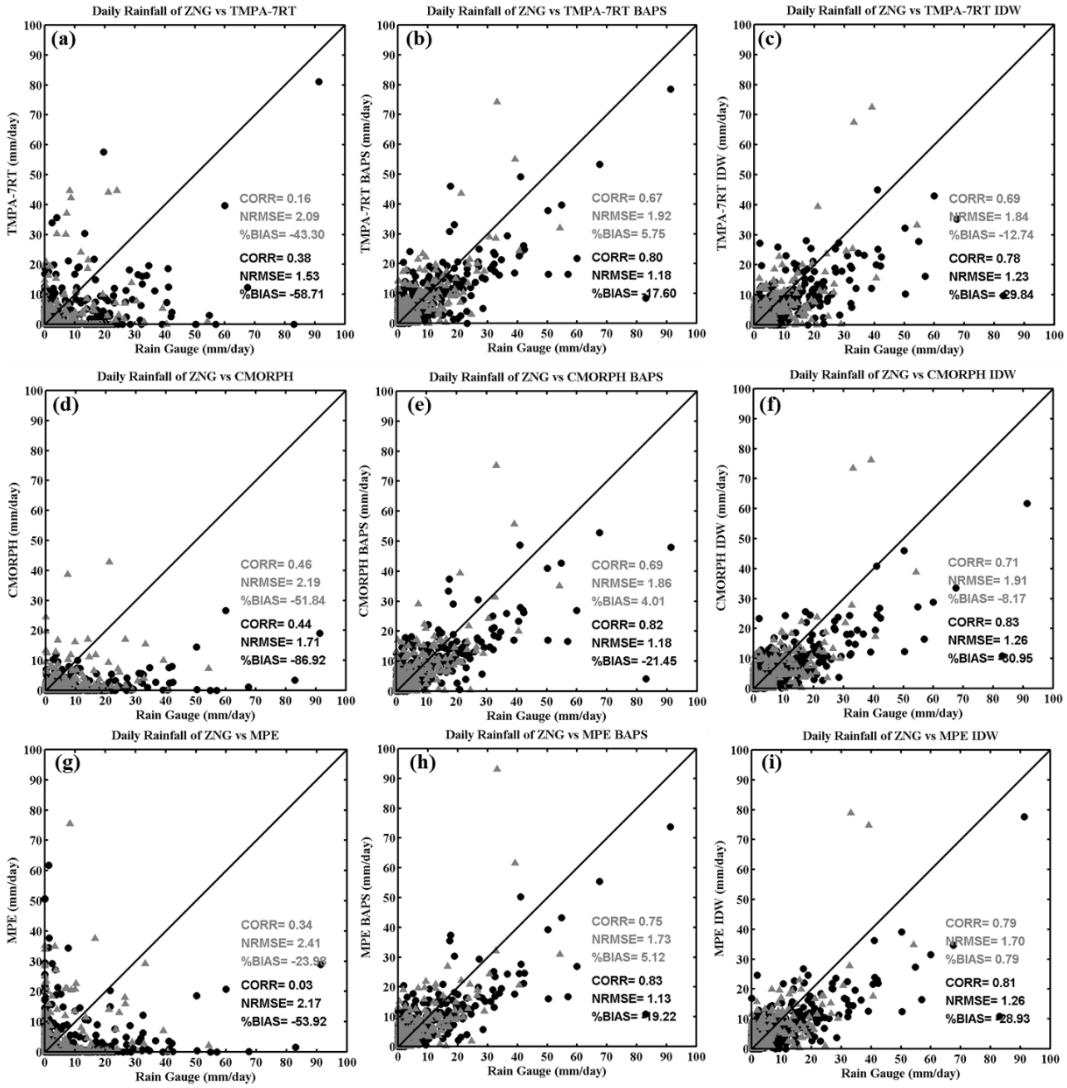

Figure 27 Daily scatterplots of rain gauge ZNG observations vs. SBP products before and after bias adjustment during 2007-2011 period. Station ZNG (in Region 1) vs. (a) TMPA-7RT, (b) TMPA-7RT BAPS, (c) TMPA-7RT IDW, (d) CMORPH, (e) CMORPH BAPS, (f) CMORPH-IDW, (g) MPE, (h) MPE BAPS, and (i) MPE-IDW. Triangle markers and gray colored statistics are for the warm season and circle markers and black colored statistics are for the cold season.

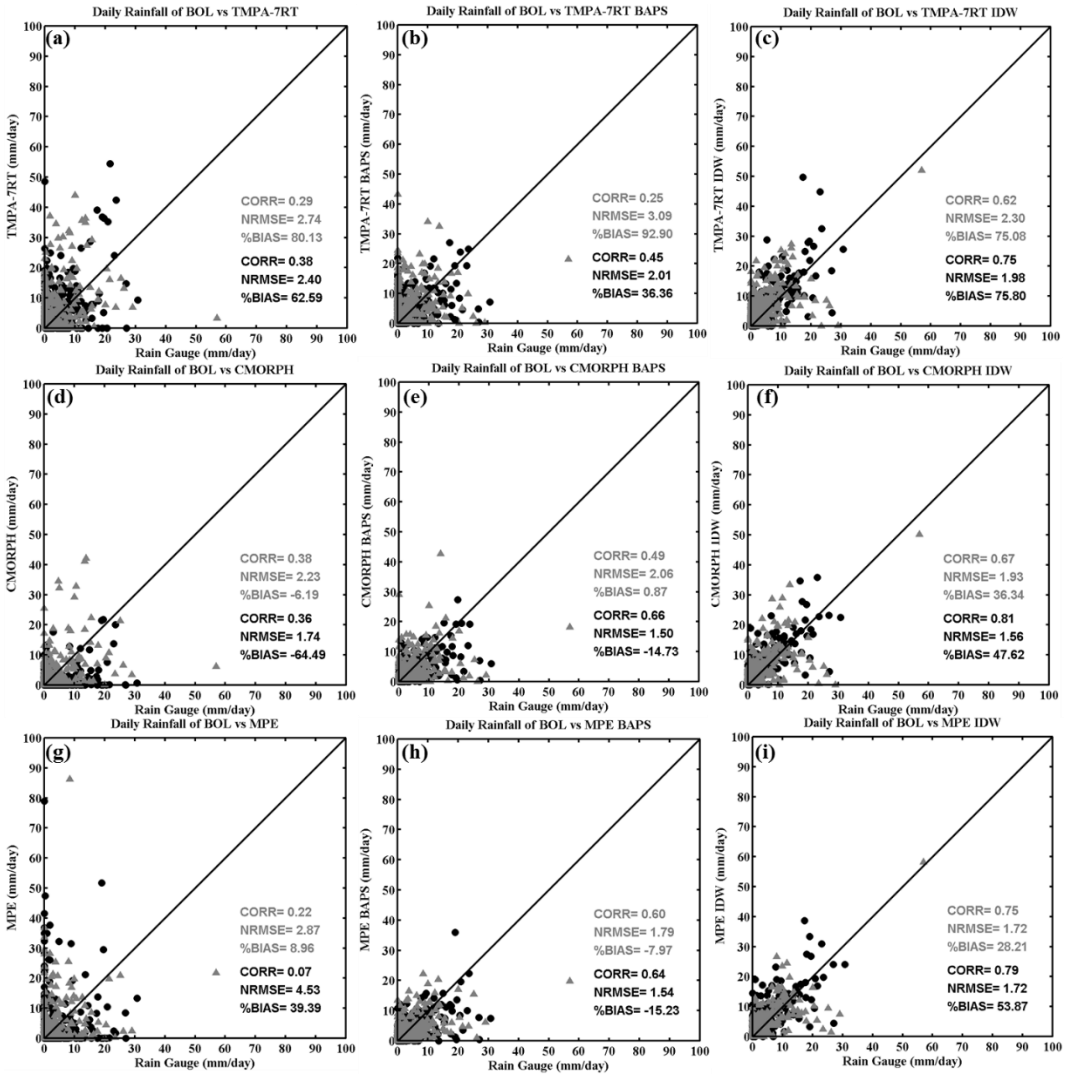

Figure 28 Daily scatterplots of rain gauge BOL observations vs. SBP products before and after bias adjustment during 2007-2011 period. Station BOL (in Region 2) vs. (a) TMPA-7RT, (b) TMPA-7RT BAPS, (c) TMPA-7RT IDW, (d) CMORPH, (e) CMORPH BAPS, (f) CMORPH-IDW, (g) MPE, (h) MPE BAPS, and (i) MPE-IDW. Triangle markers and gray colored statistics are for the warm season and circle markers and black colored statistics are for the cold season.

Comparison between rain gauges (point scale) and corresponding SBP grid performance are studied up to this point. In order to understand spatial performance of the proposed bias adjustment methodology investigation of the correspondence between RGP grids and corresponding SBP grids will be presented next. To understand the temporal variation in the performance of the BAPS bias adjustment methodology the time series of monthly

precipitation averaged over Region 1 and Region 2 is presented in Figure 29. In Region 1 (Fig. 29 a, b, c), significant underestimation is apparent for the SBP products compared to RGP, especially in cold season. This underestimation is largely corrected by extent by both BAPS and IDW bias adjustment algorithms. In Region 2 (Fig. 29 d, e, f) SBP products in general overestimates RGP at the monthly time scale with the exception of CMORPH. It can be seen that both BAPS and IDW algorithms resulted in improved precipitation estimates as indicated by red and green dot markers aligned close to the black line (RGP). However, it can also be seen that after adjustment with the IDW algorithm overestimation still persists in the precipitation estimates indicating inability of the algorithm to correct for this error. In summary, BAPS adjustment algorithm resulted in better precipitation estimates compared to IDW algorithm at the monthly timescale without significant seasonal dependency.

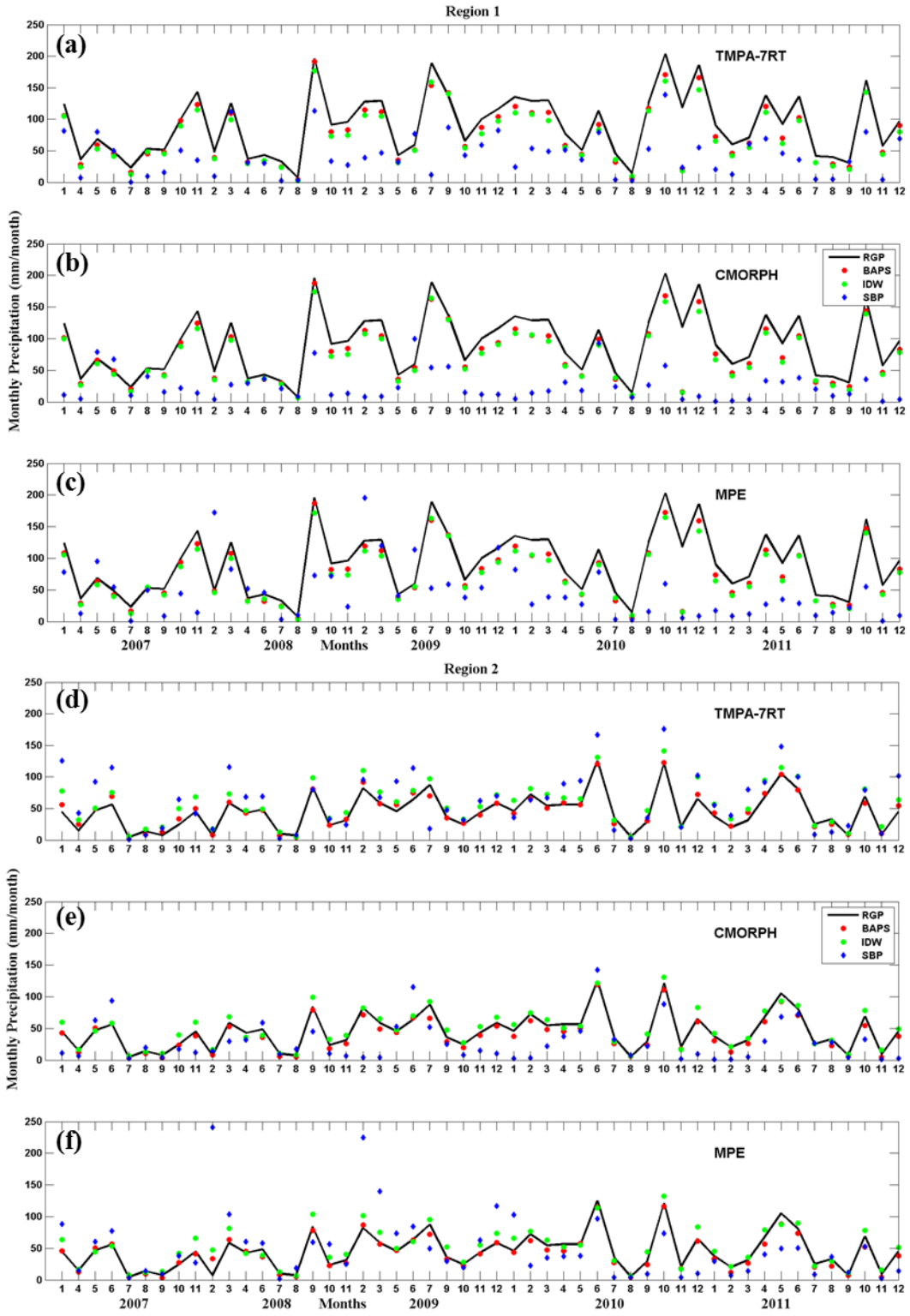

Figure 29 Monthly time-series of average precipitation for BAPS, SBP and RGP over (a, b, c) Region 1 and (d, e, f) Region 2.

Box plots in Figure 30 show summary statistics calculated by comparing daily precipitation estimates from RGP grids and their co-located SBP grids located in Region 1 and Region 2 during cold and warm seasons. In these box plots horizontal lines are 25^{th} and 75^{th} percentiles and median (50^{th} percentile) of the distribution, vertical lines represent the extent of the rest of the data which is 1.5 times the 2^{5th}-75^{th} percentile range and outliers are represented by '+' markers. Note that TMPA-7A product already incorporated monthly rain gauge information and hence was not bias adjusted using BAPS and IDW algorithms. Starting with the CORR statistic, it can be seen from Fig. 30a that all SBP products are characterized by CORR statistics lower than 0.5, while TMPA-7A resulted in highest values in general since already includes rain gauge information. After bias adjustment with BAPS and IDW algorithms (Fig 30b and c) CORR statistics significantly increased with values around 0.9 for Region 1 and with values ranging 0.5 to 0.9 for Region 2. Note that improvements were less significant for the TMPA-7RT algorithm in Region 2 for both BAPS and IDW methodologies. This might be again due to the fact that TMPA-7RT product is characterized by heterogeneous spatial distribution in Region 2. It can be seen that IDW algorithm resulted in slightly better performance than the BAPS algorithm in terms of CORR statistic. Focusing on the NRMSE statistic (Fig. 30d, e, f) it can be seen that BAPS algorithm resulted in improved performance regardless of season and region, but more specifically for cold season in Region 2. In terms of %BIAS statistic (Fig. 30g,h,i) all SBP products are characterized by significant overestimation in Region 2 and significant underestimation in Region 1, CMORPH being an exception (Fig. 30g). Bias adjustment with BAPS algorithm resulted in significantly favorable %BIAS values compared to IDW algorithm, which is more pronounced for the cold season in Region 2. It can be seen from Figure 30i that IDW algorithm has difficulty in correcting the %BIAS especially in Region 2 cold season. In summary, bias adjusted SBP products agree well with the rain gauge based gridded precipitation products with high CORR, low NRMSE and favorable %BIAS statistics, more specifically in Region 1. While IDW algorithm resulted in slightly improved CORR statistic as compared to BAPS algorithm, the later performed better in terms of NRMSE and %BIAS statistics especially in Region 2 cold season. It is clear that cold season

performance is better than warm season. BAPS bias adjustment procedure seems to perform better during cold season and in Region 1, due respectively to less convective precipitation occurrence and higher density of rain gauges.

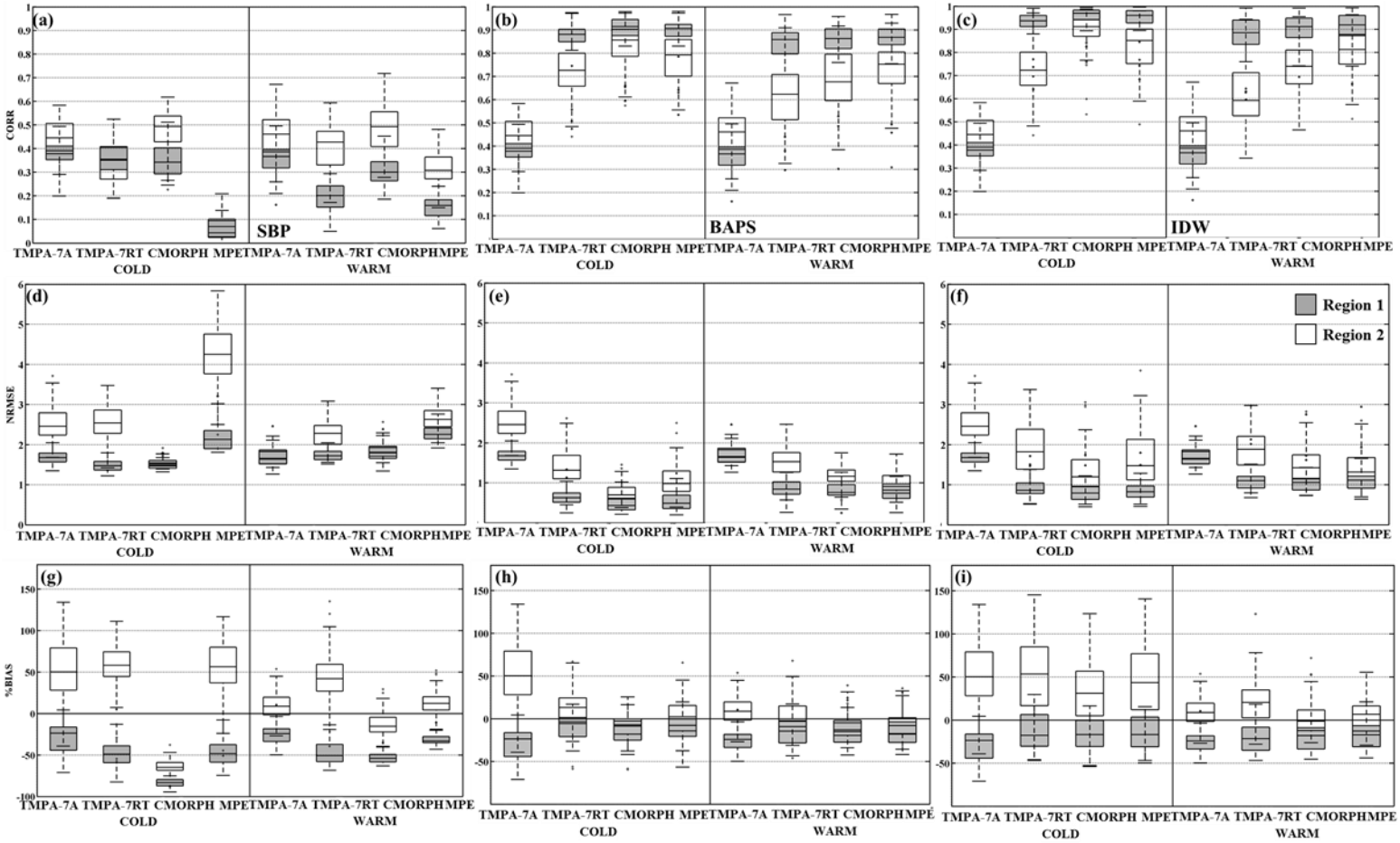

Figure 30 Daily statistical results computed between RGP grids in Region 1 (Gray box) and Region 2 (White box) and their corresponding co-located SBP product grids before bias adjustment, (a, d, g) after BAPS bias adjustment and (b, e, h) after IDW bias adjustment.

Figure 31a, b, c and 31d, e, f compare respectively, the frequency of light precipitation (1-3mm/day) and heavy precipitation (10-20mm/day) reported by RGP and SBP products before and after bias adjustment. Before bias adjustment (Fig. 31a) it is clear that TMPA-7RT underestimated the number of days with light precipitation in Region 1 regardless of the season, and bias adjustment algorithms were able to correct for this error with slight overestimation for cold season. CMORPH product slightly underestimated the number of days with light rain in cold season regardless of the region and after bias correction slight overestimation is evident in cold season. In general, it can be seen that both BAPS and IDW bias adjustment algorithms improved the frequency of light precipitation detection to the same extent in Region 1 with slight overestimation in cold season. In Region 2, however, BAPS algorithm provided better light precipitation frequency compared to IDW algorithm more specifically in cold season. Focusing on the heavy precipitation events (Fig. 31d, e, f), it can be seen that RGP dataset reported significantly more number of days with heavy precipitation in Region 1 compared to Region 2 in cold and warm seasons and before bias adjustment SBP products fail to discriminate this behavior. After bias adjustment using BAPS algorithm this behavior is successfully represented by the SBP products (Fig. 31e). IDW algorithm was able to represent this behavior to some extent, with underestimation of heavy precipitation in Region 1 and overestimation in Region 2.

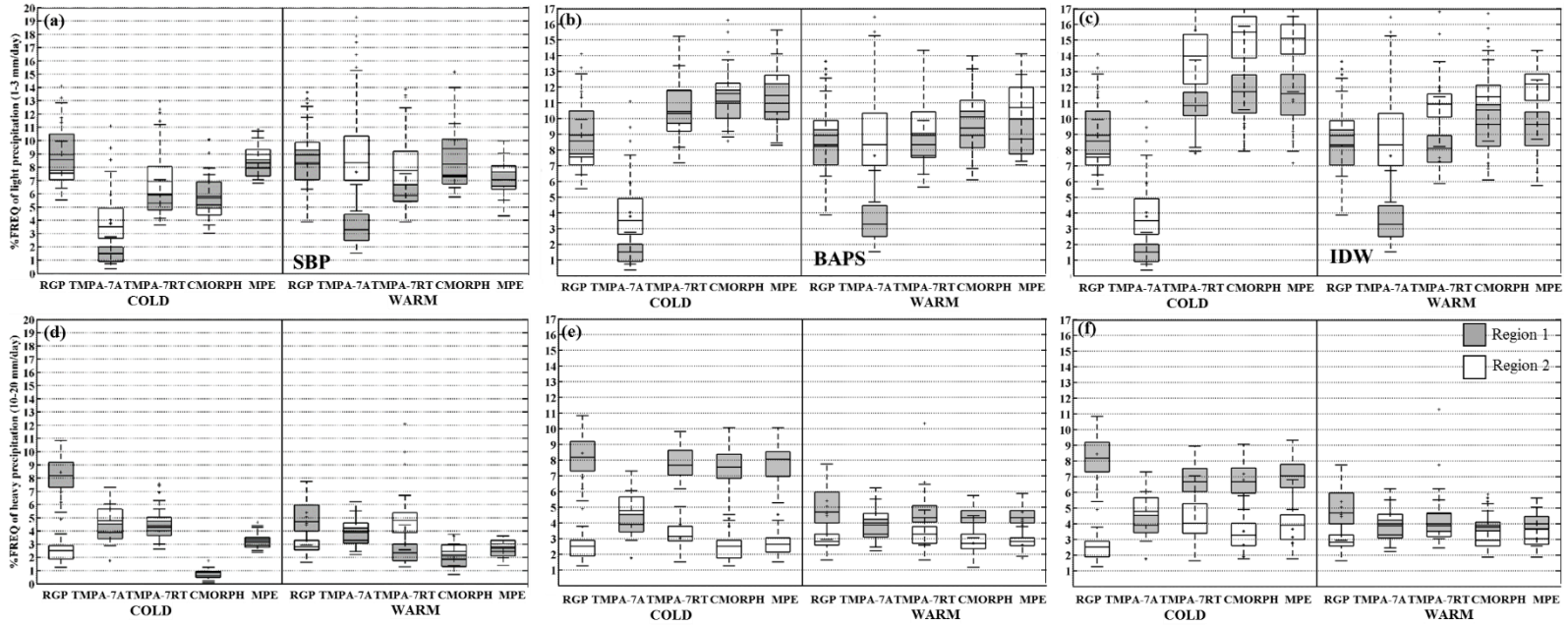

Figure 31 The frequency of (a, b, c) light precipitation (1-3 mm/day) and (d, e, f) heavy precipitation (10-20 mm/day) reported by RGP and by SBP products before and after bias adjustment.

Figure 32 and 33 shows the seasonal variation of POD and FAR categorical performance measures for precipitation magnitudes greater than 1 mm/day and for those greater than 9 mm/day, respectively. Note that the heavy precipitation threshold (9mm/day) is selected to ensure that the categorical measures for each grid combination is calculated based on at least 4 samples. It should be noted that POD and FAR are complementary measures and hence should be considered together to understand the performance tradeoff between correctly detected observed precipitation and falsely estimated precipitation. It can be seen from these figures that bias adjustment algorithms significantly improved both light and heavy precipitation detection capability of the SBP products. Focusing on light precipitation (Fig. 32), in Region 1 BAPS algorithm provided slightly higher (better) POD and lower (better) FAR statistics regardless of the season compared to IDW algorithm. In Region 2, IDW algorithm provided higher (better) POD values compared to BAPS algorithm, however at the expense of higher (poorer) FAR values. For heavy precipitation events (Fig. 33) similar performance trend can be observed. In Region 1 BAPS algorithm provided significantly higher (better) POD and lower (better) FAR statistics regardless of the season compared to IDW algorithm. In Region 2 cold season, IDW algorithm provided higher (better) POD values compared to BAPS algorithm, however at the expense of higher (poorer) FAR values. In Region 2 warm season, BAPS and IDW algorithms provided similar POD values, with the former providing lower (better) FAR values.

Next, performance improvement of individual SBP products with the BAPS algorithm will be discussed for light (Fig. 32) and heavy (Fig. 33) precipitation events. Before bias adjustment CMORPH had the detection problem for precipitation magnitudes greater than 1 mm/day, and BAPS bias adjustment provided significant improvement over this problem. TMPA-7RT can be characterized by a detection problem (low POD and low FAR) in Region 1 and overestimation problem (high POD and high FAR) in Region 2. The BAPS correction procedure overcome these problems significantly for Region 1 but for Region 2 it is not as significant as in Region 1. Moreover before the correction SBP products had seasonal dependency with higher performance in warm season, with the BAPS correction procedure the performance of the SBP products improved for cold

season significantly. In terms of heavy precipitation events, both CMORPH and MPE products show significant deterioration in POD performance in cold season before correction. These deteriorations are corrected to some extent but heterogeneity still exists for the heavy precipitation. For all SBP products, the BAPS algorithm performance in Region 1 is much better than the Region 2. Related with these significant improvements in POD and FAR, it can be concluded that proposed BAPS correction algorithm can introduce rain in areas where the SBP does not detect rainfall and algorithm can assign no rainfall where SBP falsely detects rainfall.

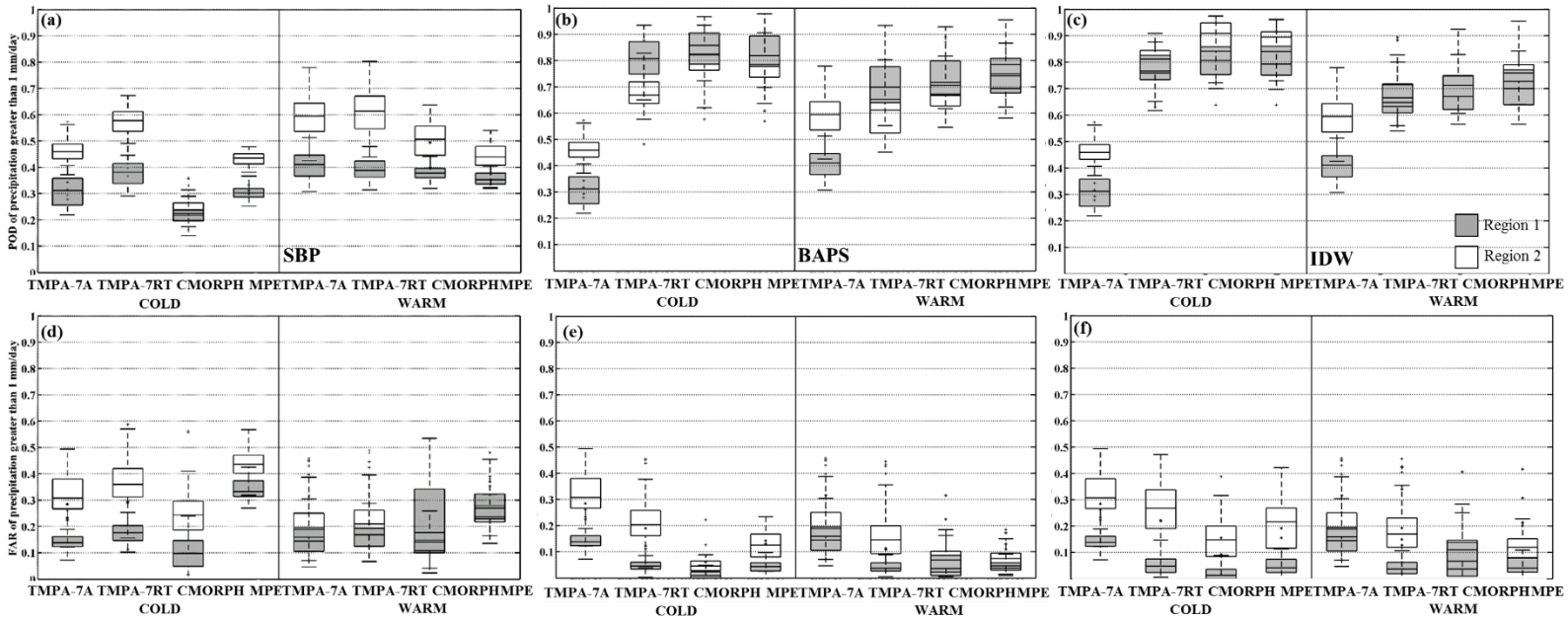

Figure 32 Categorical performance results for precipitation greater than 1 mm/day of (a, b, c) POD values and (d, e, f) FAR values before and after bias adjustment with BAPS and IDW algorithms.

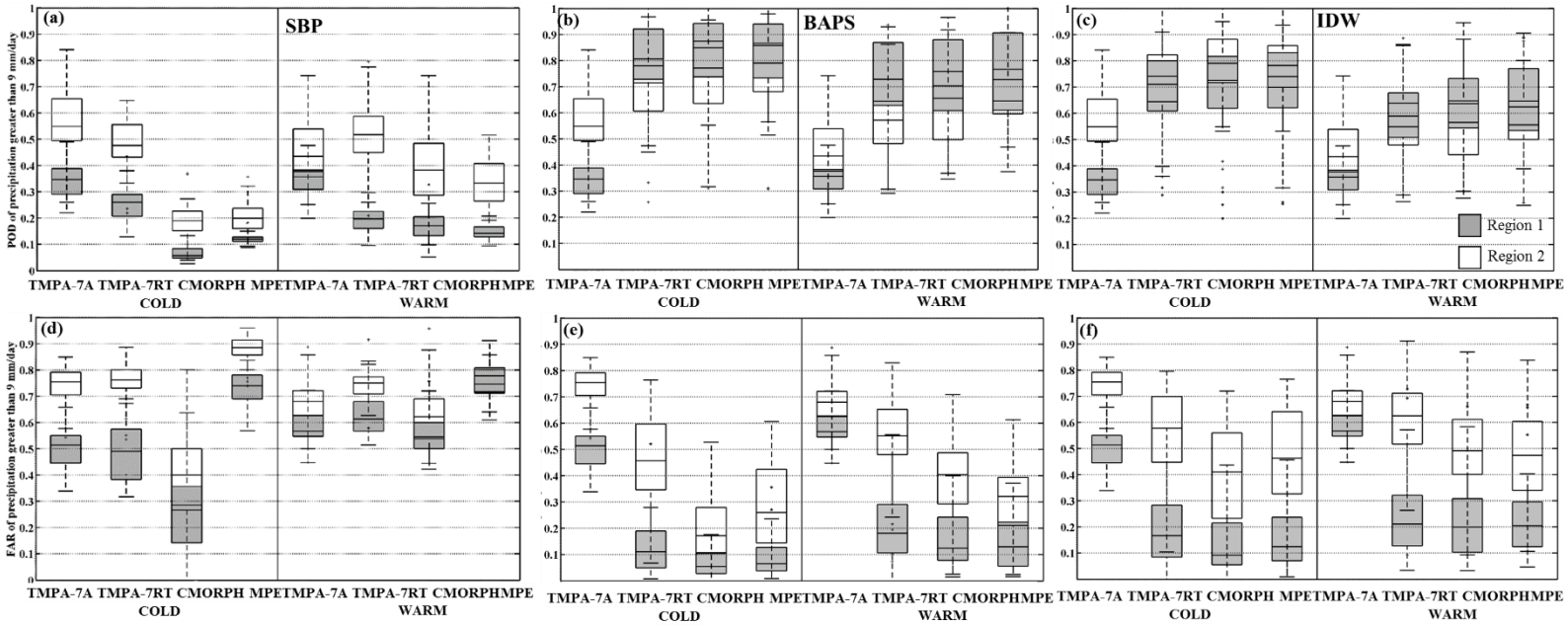

Figure 33 Categorical performance results for precipitation greater than 9 mm/day of (a, b, c) POD values and (d, e, f) FAR values before and after bias adjustment with BAPS and IDW algorithm.

CHAPTER 5

IMPLEMENTATION, DIAGNOSTIC EVALUATION AND CALIBRATION OF THE MIKE SHE-MIKE 11 MODEL IN THE ARAÇ BASIN

This chapter firstly presents the physically based, spatially distributed, integrated hydrologic modeling, and then define MIKE SHE-MIKE 11 hydrologic modeling modules. Finally implementation of the MIKE SHE-MIKE 11 model for the Araç Basin located in the Western Black Sea Region is explained. Parameter sensitivity analysis and evaluation using a diagnostic approach is presented followed by constraining of the parameter sets based on signature measures representing major functions of a watershed system. The performance of the model driven by gridded RGP product and SBP products before and after bias adjustment using BAPS algorithm is provided.

5.1. Introduction

To better understand and manage water systems under changing climate and meet the increasing demand for water, hydrologic modeling has become essential tool with two main roles. Hydrological model's first main role is to improve understanding of the physical processes and interactions within a watershed. Second main role is the application of this understanding for forecasting in order to manage and protect the water resources. To improve our understanding of the physical processes and interactions quantitative understanding of the hydrological cycle is essential. Water cycle or hydrologic cycle describes the movement of water on, above and below the Earth's

surface. Due to great variability in space and time scales it is often difficult to understand and manage water resources; existence of complex interactions between different compartments and fluxes add further difficulties to measure and observe variable of interest. Hydrologic system is affected by many factors which make it very complex such as climate system, heterogeneities in soil and geologic units and modification by human activities. This heterogeneity makes it difficult to represent hydrological processes accurately (Grayson and Blöschl, 2000). Comprehensive research and engineering studies are conducted in this area to understand the various aspects of hydrologic cycle. However, these studies were mainly conducted only concentrating on either surface water or groundwater without emphasizing their often complex interrelations. Groundwater and surface water are hydraulically connected at various degrees in different landscapes, therefore in order to increase our knowledge in this area and better manage water resources we have to conduct studies on interrelation of surface water and groundwater.

Questions related with;

- Basin scale water management
- integrated use of surface water and groundwater
- floodplain and wetland management
- anthropogenic effects on water resources
- water quality influences of surface water on groundwater, vice versa

cannot be answered by traditional surface water and groundwater models. Some surface water models have basic, limited groundwater component, therefore they are used for only surface water modeling. Same goes with the groundwater models with basic surface water components. Therefore, to be able to answer these questions, watersheds modeling should be conducted by fully integrated hydrologic models. Integrated hydrological models can simulate, water flow processes, movement of sediment, chemical, nutrient, waterborne organisms and their role in watershed habitats and ecology.

Mainly hydrological models can be classified according to;

- description of the physical process (as conceptual and physically based)
- spatial description of catchment processes (as lumped and distributed) (Refsgaard, 1997).

Understanding of the physics of the hydrological processes which controls the catchment response is important and should be represented by physically based equations. Physically based equations describes mass flow and momentum transfers which solves the partial differential equations such as St. Venant equations and Darcy's equations. Therefore integrated physically based distributed hydrological models can represent hydrological cycle thoroughly and can be applied to many kinds of hydrological problems. However it should be noted that physically based models requires a significant amount of data and time to solve equations and complexity may lead to over parameterization and predictive uncertainty.

As it is stated earlier, hydrologic system is affected by climate system, heterogeneity in soil and geologic units and modification by human activities, all of which makes the system heterogeneous and complex and as a result makes it difficult to represent hydrological processes accurately. Lumped models make the assumption that rainfall and hydrologic parameters are uniform across the watershed and operate at the "point scale". Through representing dominant processes at a conceptual level, lumped models are comprised of relatively simple model structure that enables short run times. Lumped models are generally used for flood forecasting and/or reservoir operation purpose due to this short run times and simpler model structures. Spatially distributed models, on the other hand, consider spatial variations in the landscape and hydrologic processes across the watershed through spatially variable parameters and states such as climatic conditions, topography, soil, geology and vegetation which are related to the physical characteristics of a watershed (Refsgaard et al., 1996). Distributed models simulate:

- spatial variability of both input and output of hydrologic variables,
- hydrologic response at interior ungauged sites within a watershed basin (Smith et al. 2004).

Spatial distribution of hydrologic processes can be simulated by distributed hydrological models to improve the knowledge of watershed functioning so that we can understand and manage water related natural hazards such as flooding. Smith et al. (2004) reported that for flood forecasting at the basin outlet, distributed models does not necessarily outperform the lumped models. They note however that, testing the performance of simulation at the interior point of the basin is not studied in detail yet. Moreover, distributed models have potential advantages for predicting runoff in ungauged basins, and simulate the impact of land use/land change effects on hydrologic response for the watershed basin (Refsgaard et al. 1997; Downer et al. 2002; Hayakawa et al. 1995).

Main difficulty in implementation of physically-based spatially distributed integrated hydrologic models is the requirement of detailed spatial and temporal datasets regarding physical and dynamic characteristics of the watershed, such as climate, soils, land cover, geology and hydrogeology, which are often not available. Some of these detailed input data can be provided by remotely sensed information and application of Geographical Information Systems (e.g. Khan et al. 2011). It should be noted that even though physically based distributed hydrological models simulate majority of the hydrologic processes, it is often not practical to include all the processes in the model because of data, time and budget limitations. Instead dominate hydrological processes selected based on the conceptual understanding of the flow system and the purpose of the modeling could be represented in the model.

There exist a number of hydrologic models that are widely used with the objective of integrating surface waer and groundwater processes, such as MODHMS (Panday and Huyakorn, 2004), ParFlow (Kollet and Maxwell, 2006), HydroGeoSphere (Therrien et al., 2007) and MIKE SHE (Graham and Butts, 2005). The advantage of the MIKE SHE-MIKE 11 model is that it is widely used, well documented and its modular structure allows representation of hydrological processes at various level of complexity.

5.2. Literature Review on MIKE SHE - MIKE 11 Hydrologic Modeling

MIKE SHE has been used for wide range of hydrologic applications. Table 5 summarizes the literature review on hydrological modeling studies that utilized MIKE SHE-MIKE 11 integrated model at different geographic regions of the world.

Table 5 Literature review on hydrological modeling with the MIKE SHE-MIKE 11 model.

Reference	Model	Watershed & Time Interval	Grid Size	Inputs & Model Setup	Calibration
Sultana and Caulibaly (2011)	MIKE SHE/ MIKE 11	Spencer creek (291 km^2) 12 year for calibration 8 year for validation	50m	• 50m DEM • Precipitation interpolated by using Theissen polygon method • Potential ET calculated by using Blaney-Cridle method • Snow melt simulated by using degree day method • Land use data included 30 different type which is further lumped to six type. • LAI, root depth and Kc are determined from MIKE database • Finite difference method used for overland flow Manning M and detention storage are obtained from literature • Initial water depth set to zero • Soil is divided into 16 type however they lumped to 5 type • 2 Layer UZ is used to simulate unsaturated zone flow component • River network is simplified to 18 river channel • Uniform Manning M used for river channels • Total 174 cross sectional data obtained, some of which are added by interpolation and some are obtained from 1m DEM. • Water level and discharge values from flow stations are used as initial conditions • All branches are coupled with MIKE 11 and MIKE SHE	• Model calibrated against daily flows (4 flow stations) • First peak flows are calibrated then base flows • Peak flows are calibrated by adjusting Manning's M, snowmelt parameters and detention storage • Model was able to capture the snow storage well. • Simulated flows were in good agreement with observed flow.
Wijesekara et al (2012)	MIKE SHE/ MIKE 11	Elbow River (1238 km^2) 5 year for calibration 5 year for validation	200m	• Land use land cover includes 9 type • LAI, root depth are obtained from literature • 25m DEM • Soil is divided into 2 different class • 16 survey cross sections are used and remaining cross sections are digitized from DEM. Total 141 cross section entered • 10 flow stations • Finite difference is used for overland flow • 2 Layer UZ is used for unsaturated zone • Linear reservoir method is used for saturated zone	• Sensitivity analysis is conducted for saturated hydraulic conductivity, ET surface depth, degree day coefficient, detention storage, surface roughness, and time constants for interflow and baseflow • According to sensitivity analysis two parameters area calibrated, saturated hydraulic conductivity and manning's M • MIKE SHE-MIKE 11 is used to assess the impact of land-use changes on different hydrological processes of the study region.

Table 5 (continued)

Sahoo et al (2006)	MIKE SHE	Two sub basins (2.6 km^2 and 24.6 km^2) 1 year calibration 1 year validation		• Soil classification divided area to 31 major soil types which are further lumped to 16 type. Van Genuchten parameters of the soils estimated using RETC computer code and neural network option • 7 LU/LC type • 2 meteorological station used • 2 flow station used • Reference Evapotranspiration is calculated by using Penman Monteith equation • Kc values are obtained from MIKE SHE database • Detention storage set to 1m and tie constant to 120 day • Manning number is set constant for all channels	• Study find out that distributed rainfall along the watershed is important for flow estimation. • Calibration results produced better flows. • Initial soil moisture tension, initial phreatic level and initial drainage depth were found not so important as long as values are physically realistic. On the other hand Manning's M and hydraulic conductivity values are found important and changing the shape of the hydrograph.
Thompson et al (2013)	MIKE SHE/MIKE 11	Mekong River ($795000 km^2$) 29 year calibration 7 year validation	10km	• 1km DEM • 1km FAO digital soil map of the world is used to classify the soil and it is aggregated to 4 broad categories. Infiltration rate and percentage water content at saturation, field capacity and wilting point for each soil obtained from literature. • 1km LU/LC from USGS global land cover characterization dataset used with 24 classes aggregated to 9 class. • Variation in LAI through year taken from Kite (2000) which is based on time series of NDVI derived from NOAA AVHRR imagery. Root depths are obtained from literature and database of MIKE SHE. • LU/LC grids are used (all forest types combined into one category) used to spatially distribute Manning's M (values are taken from literature) for overland flow resistance. • Cross sections are taken from literature and Mekong river commission. Cross section widths are checked at google earth pro. Cross section bank elevations are taken from relevant MIKE SHE topographic grid square. Manning n values are taken from literature. • Degree day snow scheme selected • PET is calculated by Linacre method	• Automated calibration method used • Interflow time constants for saturated zone interflow reservoirs, percolation time constants for saturated zone interflow reservoirs, time constant for base-flow reservoirs, dead storage in base flow reservoirs, precipitation lapse rate, temperature lapse rate, snow melt degree-day coefficient are calibrated. • Model performance is stated as excellent/very good and found out that superior to the SLURP model.

Table 5 (continued)

Gül et al (2010)	MIKE SHE/MIKE 11	Havelse river system (250 km^2) 3 year calibration 2 year validation	100m	• Corine land cover 2000 dataset is used for LU/LC • 100 m DEM • Soil data obtained from GEUS • Degree day snow scheme selected • Overland flow method is chosen as finite difference method. Manning's M set uniformly to 3. Detention storage again uniformly to 10 mm which are both calibrated later. • 2 Layer water balance method chosen for unsaturated flow. Soil hydraulic parameters are assigned values according to FAO.	• Hydraulic conductivities for geological layers, manning's roughness coefficient, detention storage, drainage level, drainage time constant, soil water content at saturation, at field capacity, at field wilting point and infiltration rate of each soil type are calibrated. • Model is found to be suitable for modeling lowland river systems and mentioned that model has important capacity if groundwater head levels, flows and UZ components are included.
Thompson et al (2009)	MIKE SHE/MIKE 11	Elmley Marshes (8.7 km^2) 18 month calibration 18 month validation	30m	• 1:2500 topographic map is used. • Zero flow boundary around the model area specified • Uniform soil profile • Potential evapotranspiration is calculated by Penmann Monteith equation • Cross sections are based on field surveys, aerial photography and from literature • Uniform channel roughness and leakage coefficients are used	• Overland flow resistance, channel roughness, leakage coefficient are calibrated. • Model sufficiently simulates changes in hydrological conditions to infer ecological impacts.
Singh et al (2010)	MIKE SHE/ MIKE 11	Loktak Lake (4947 km^2)	600	• 7 rain gauge is used, interpolated by using Theissen polygon method • PET is calculated by Penmann Monteith equation. • Dynamic coupling of MIKE SHE with MIKE 11 includes river-aquifer exchange, overland flow from MIKE SHE and MIKE 11 river branches • 1:50000 scale land cover map is used • LAI, RD are taken from literature • 90 m resolution DEM is used • MIKE 11 branches are extracted from 1.50000 scale map. Cross sections are defined based on field surveys. All branches are coupled with MIKE SHE. Uniform manning M is assigned.	• Calibrated parameters are horizontal and vertical hydraulic conductivity of the saturated zone, unsaturated zone infiltration rate, overland flow resistance and flow resistance within stream channels. Initial values of these values are taken from literature. • Model successfully simulated impacts of climate change upon river discharge within Lake catchment.

5.3. MIKE SHE-MIKE 11 Integrated Hydrologic Model

Water on Earth cycle continually between land, sea and air where water evaporates from the oceans, lakes, rivers, soil and transpired by plants. Evaporated water vapor is transported in the atmosphere and precipitates to earth as rain and snow. Precipitated water infiltrates to the groundwater and discharges either to the streams and rivers as baseflow or to the oceans and also runs off directly to the streams and rivers which flows back to the ocean (Fig. 34). Hydrologic cycle is a closed loop and anthropogenic effects do not remove water but affect the movement and transfer of water within the cycle.

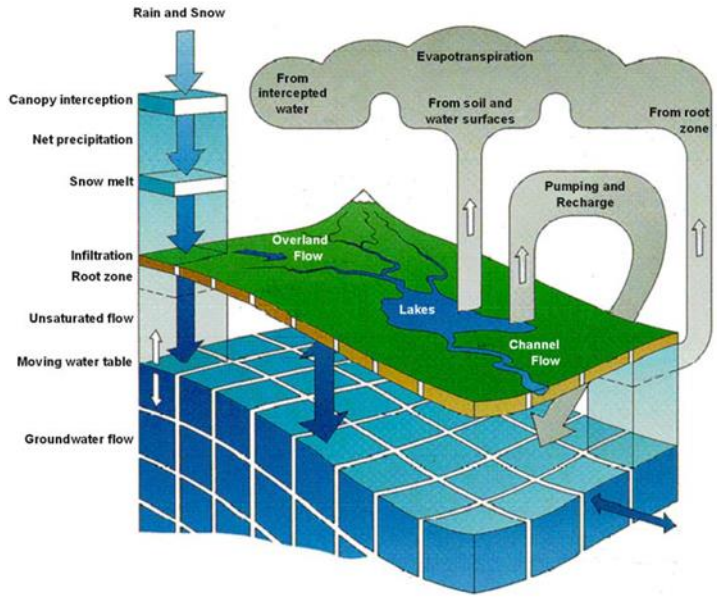

Figure 34 Hydrologic cycle simulated by MIKE SHE

Freeze and Harlan (1969) proposed a blueprint to model hydrologic cycle in which they described different flow processes by their governing partial differential equations. Later, consortium of the Institute of Hydrology in the United Kingdom, SOGREAH in France, and Danish Hydraulic Institute in Denmark applied these blueprints and developed Système Hydrologique Européen (SHE; Abbot et al. 1986). MIKE SHE emerged from this work later on. After mid-1980's MIKE SHE is further developed by DHI Water &

Environment. Today MIKE SHE evolved into a flexible, physically based, spatially distributed, integrated hydrological model.

MIKE SHE models hydrologic processes of evapotranspiration, overland flow, unsaturated flow, groundwater flow, channel flow and their interactions. Most importantly each of these processes can be modeled at different level of spatial and temporal resolution and complexity, according to the objectives of study, availability of field data and budgetary constraints. MIKE SHE can be applied to a variety of scales from single soil profile to large regions including several river catchments (Sahoo et al. 2006; Thompson et al. 2013). To simulate channel flow MIKE SHE uses MIKE 11 (Havnø et al. 1995) which can model complex channel networks and river structures.

MIKE SHE has a flexible structure enabling descriptions for each hydrologic process at various complexity levels, it can either use fully distributed conceptual approach and can simulate all the processes by using physics-based methods (Fig. 35).

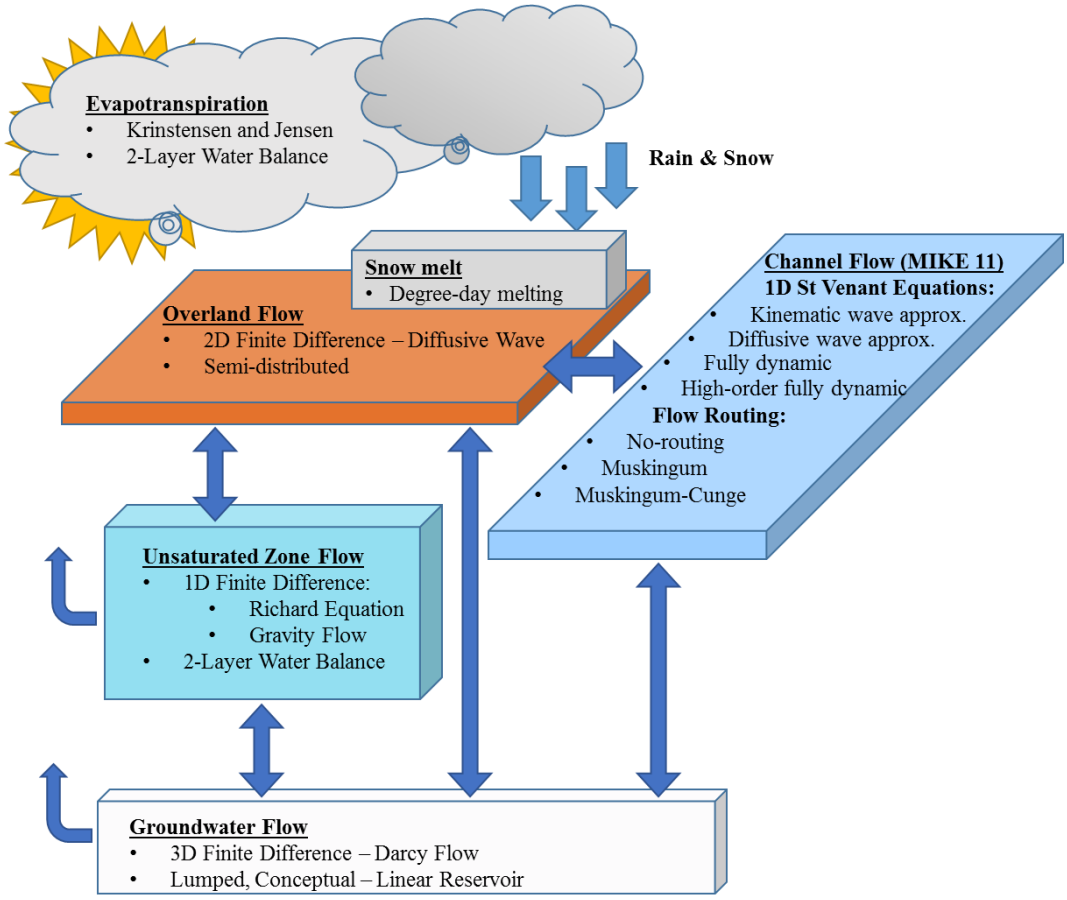

Figure 35 Schematic view of the process in MIKE SHE, including available numeric engines for each process. The arrows show the available exchange pathways for water between the process models (modified from DHI, 2012).

In the next sub-sections all the hydrologic processes included in MIKE SHE-MIKE 11 will be explained in detail.

5.3.1. Precipitation and Evapotranspiration

Precipitation is direct input to the model. Evapotranspiration is the sum of direct evaporation from water surfaces (lakes, rivers, snow surfaces and rainfall drops on leaves) and transpiration from plants. Depth of groundwater table, soil hydraulic properties and soil wetness effects the evaporation from soil. On the other hand root depth, water extraction capacity of roots from soil, leaf characteristics affects the transpiration. Unsaturated zone soil moisture content also affects the transpiration rate. In other words,

spatial variation of evapotranspiration is related with daily, seasonal, climate and land use changes.

Evapotranspiration and precipitation is important since timing and amount of recharge and overland flow is determined by evapotranspiration and infiltration to the unsaturated zone.

MIKE SHE calculate actual evapotranspiration from reference evapotranspiration. Reference evapotranspiration is calculated by idealized reference grass crop (Shuttleworth, 1992). MIKE SHE calculates actual evapotranspiration by Kristensen and Jensen method or Two-layer water balance method. Since two-layer water balance method is used in this study, this methodology will be explained in detail.

Two-layer water balance method is simplified water balance method for evapotranspiration calculation and unsaturated zone storage. This method divides unsaturated zone into two zone;

- root zone where evapotranspiration can be extracted
- zone below root zone where evapotranspiration does not occur (Yan and Smith, 1994).

Evapotranspiration is calculated explicitly and storages that water extracted are as follows;

- evaporation and sublimation is removed from snow
- infiltration to unsaturated zone and recharge to saturated zone is calculated
- evaporation from the canopy is calculated
- evaporation from ponded water is calculated
- transpiration from the unsaturated zone is calculated
- transpiration from the saturated zone is calculated

$$ET_{rate} = ET_{crop} = ET_{ref} k_c \quad (5.1)$$

where, ET_{ref}: reference evapotranspiration

ET_{crop}: crop reference evapotranspiration

k_c: crop coefficient

Maximum evapotranspiration that can be extracted in one time step;

$$ET_{max} = ET_{rate} * \Delta t \quad (5.2)$$

where, ET_{max}: maximum amount of evapotranspiration that can be removed in one time step

$$ET_{snow} = ET_{wetsnow} + ET_{drysnow} \quad (5.3)$$

where, ET_{snow}: evapotranspiration from snow storage

$ET_{wetsnow}$: evapotranspiration from wetsnow storage

$ET_{drysnow}$: evapotranspiration from drysnow storage

$$ET_{wetsnow} = ET_{ref} * \Delta t \quad (5.4)$$

If wet snow storage is insufficient then evapotranspiration will be extracted as sublimation from dry snow;

$$ET_{drysnow} = ET_{ref} * S_f * \Delta t \quad (5.5)$$

where, S_f: sublimation reduction factor

Again, if dry snow storage is not enough either, then snow storage reduction will be zero.

$$ET_{canopy} = ET_{rate} * \Delta t \quad (5.6)$$

where, ET_{canopy}: evapotranspiration from canopy storage

If there is not enough canopy storage, canopy storage reduction will be zero.

$$ET_{ponded} = ET_{rate} * \Delta t \quad (5.7)$$

where, ET_{ponded}: evapotranspiration form ponded storage

If there is not enough ponded storage, ponded storage reduction will be zero.

Evapotranspiration from unsaturated zone will be conducted only at the upper layer and when wilting point is reached evapotranspiration will stop. Evapotranspiration rate will be maximum until plant deficit fraction is reached, then evapotranspiration will be reduced linearly to zero while water content falls to wilting point. ET_{rate} will be reduced by;

$$F_{ETUZ} = \frac{\min(\theta_{act}, \theta_p) - \theta_{min}}{\theta_P - \theta_{min}} \quad (5.8)$$

where, θ_p: water content when evapotranspiration begins to be restricted

θ_{act}: current water content in the upper layer

$$\theta_p = \theta_{min} + F_p * (\theta_{max} - \theta_{min}) \quad (5.9)$$

where, θ_{min} & θ_{max}: minimum and maximum water contents

F_p: plant-specific deficit fraction

$$ET_{UZ} = ET_{rate} * F_{ETUZ} * \Delta t \quad (5.10)$$

where, ET_{UZ}: evapotranspiration from unsaturated storage

$$ET_{SZ} = ET_{rate} * F_{ETSZ} * \Delta t \quad (5.11)$$

where, ET_{SZ}: evapotranspiration from saturated storage

F_{ETSZ}: when water table is in the root zone is equal to 1 and linearly decreases to zero if water table is below the root zone

If water table is below the extinction depth, there will be zero extraction from saturated zone.

Finally actual evapotranspiration is calculated as;

$$ET_{actual} = ET_{snow} + ET_{canopy} + ET_{ponded} + ET_{UZ} + ET_{SZ} \qquad (5.12)$$

while ET_{actual} cannot be greater than ET_{max} and ET_{actual} is calculated until ET_{max} is reached.

5.3.2. Unsaturated Flow

Precipitation replenish soil moisture in the unsaturated zone while evapotranspiration extract water from it, creating cyclic fluctuations. Since gravity dominates infiltration, unsaturated flow in MIKE SHE is calculated only vertically to reduce computation cost. MIKE SHE calculates unsaturated flow by 3 methods; full Richards equation, simplified Gravity flow procedure and Two-Layer water balance. Since Richards equation and Gravity flow procedures are computationally intensive and requires detailed soil data, such as soil horizon information, which is not available for the study area, Two-Layer water balance method is used in this study.

As stated in the previous section, Two-Layer water balance divides unsaturated zone into two as; root zone and zone below the root zone. After evapotranspiration extraction water recharges to the saturated zone as follows;

If there is a ponded water on the ground F_{ETSZ} is multiplied by anaerobic tolerance factor, F_{antol}. After extraction of water remainder water recharges to the saturated zone as;

$$ET_{left} = \left(ET_{max} - ET_{snow} - ET_{canopy} - ET_{UZ}\right) * F_{antol} \qquad (5.13)$$

5.3.3. Overland Flow

Overland flow path and amount is affected by topography, flow resistance, evaporation and infiltration. MIKE SHE calculates overland flow in two different methods as; finite difference method or semi-distributed method. In this study finite difference method is used which uses diffusive wave approximation of the Saint Venant equations.

The conservation of mass gives;

$$\frac{\partial h}{\partial t} + \frac{\partial}{\partial x}(uh) + \frac{\partial}{\partial y}(vh) = i \qquad (5.14)$$

where, h(x,y): flow depth above ground surface

u(x,y) & v(x,y): flow velocities in the x and y directions respectively

i(x,y): net input into overland flow

And the momentum equation gives;

$$S_{fx} = S_{Ox} - \frac{\partial h}{\partial x} - \frac{u}{g}\frac{\partial u}{\partial x} - \frac{1}{g}\frac{\partial u}{\partial t} - \frac{qu}{gh} \qquad (5.15)$$

$$S_{fy} = S_{Oy} - \frac{\partial h}{\partial y} - \frac{v}{g}\frac{\partial v}{\partial y} - \frac{1}{g}\frac{\partial v}{\partial t} - \frac{qv}{gh} \qquad (5.16)$$

where, S_f: friction slopes in x and y directions

S_o: slope of the ground surface

Equations 6.14, 6.15, 6.16 are known as St. Venant equations which calculates fully dynamic description of 2D free surface flow. It is clear that these equations are numerically challenging, the complexities of the equations are reduced by ignoring momentum losses due to local and convective acceleration and lateral inflows perpendicular to the flow direction. This reduced equations are known as diffusive wave approximation and MIKE SHE implements this equation.

$$uh = K_x(-\frac{\partial z}{\partial x})^{1/2} h^{5/3} \quad (5.17)$$

$$vh = K_y(-\frac{\partial z}{\partial y})^{1/2} h^{5/3} \quad (5.18)$$

where, K_x & K_y: Strickler coefficients in the two directions which is equivalent of Manning M which ranges in between 100 (smooth channels) to 10 (thickly vegetated channel). Manning M is the inverse of the commonly used Mannings n.

uh & vh: discharge per unit length along the cell boundary in the x and y directions

5.3.4. Channel Flow (MIKE 11)

Overland flow is input to the streams and rivers where topography is lower than the surrounding region. In MIKE 11 channel flow is calculated by implicit, 1D finite-difference formulation. MIKE 11 also contains simple hydrologic routing methods such as Muskingum and Muskingum-Cunge methods. In this study river branches are defined as kinematic routing and calculated by Muskingum-Cunge. Muskingum-cunge is based on diffusion wave model while including pressure term, method neglects local and convective acceleration terms, in other words method approximates the diffusion of natural flood wave. Kinematic routing method starts calculation from upstream in the river network. In other words discharge computation is conducted successively. At kinematic routing points (Fig. 36) discharge is calculated from one time level to the next by considering previous and new discharges at the location of the upstream boundary.

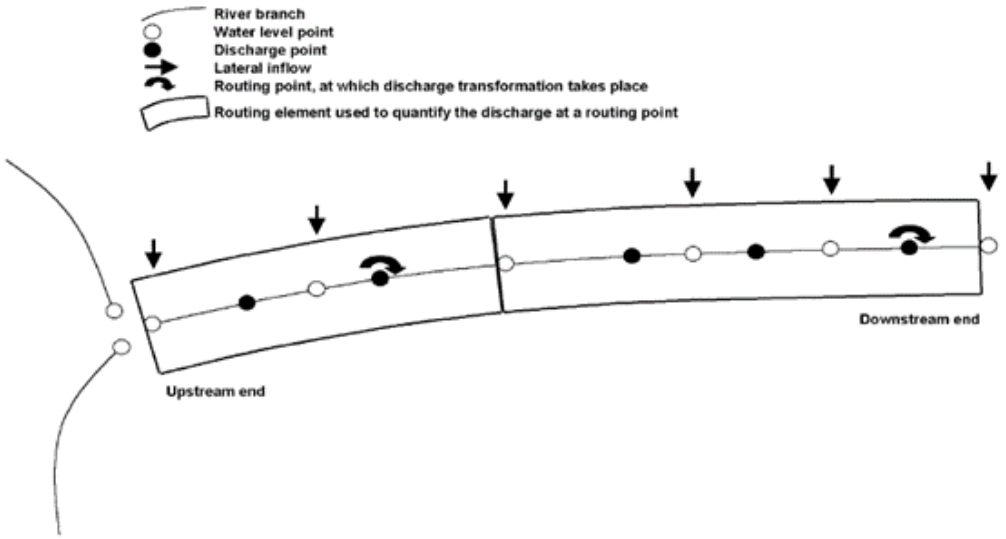

Figure 36 MIKE 11 kinematic routing branch elements and transformation points (DHI, 2012).

$$Q_{i+1}^{j+1} = C_1 Q_i^{j+1} + C_2 Q_i^j + C_3 Q_{i+1}^j + C_4 \quad (5.19)$$

where, i & j: considered grid point and time level, respectively

$$C_1 = \frac{\Delta t - 2K_x}{2K(1-x)+\Delta t} \quad (5.20)$$

$$C_2 = \frac{\Delta t - 2K_x}{2K(1-x)+\Delta t} \quad (5.21)$$

$$C_3 = \frac{2K(1-x)-\Delta t}{2K(1-x)+\Delta t} \quad (5.22)$$

$$C_4 = \frac{Q_{lat}\Delta t}{2K(1-x)+\Delta t} \quad (5.23)$$

$$K = \frac{\Delta x}{c_k} \quad (5.24)$$

$$x = 1/2(1 - \frac{Q}{Bc_k S_0 \Delta x}) \quad (5.25)$$

$$c_k = \frac{dQ}{dA} = \frac{dQ}{dx}\frac{dx}{dA} + \frac{dQ}{dt}\frac{dt}{dA} \quad (5.26)$$

where, Δx: length of kinematic routing element

S_0: bed slope

B, A & Q: width, cross sectional area and discharge, respectively and calculated at the elevation point just upstream of the considered kinematic routing point (Fig. 35).

x & t: space and time variables, respectively.

To calculate water level at a specific point, one upstream and one downstream kinematic routing points are located and water level is calculated at those point, if the specific point is in-between these two points, linear interpolation is conducted to obtain water level at that point. If upstream and downstream kinematic routing points cannot be located then Manning equation is used to compute discharge:

$$Q = MR^{2/3}S_0^{1/2}A \qquad (5.27)$$

where, M: manning resistance number

R: hydraulic radius

S_0: bed slope

A: cross sectional area

MIKE 11 is coupled with MIKE SHE where river network contains digitized points and calculation points where cross-sections are defined. All these information interpolated to the edges of MIKE SHE grids for overland flow and saturated flow exchange with MIKE 11 (Fig. 37). MIKE SHE only exchange water with intersect MIKE SHE overland flow and groundwater grids. Exchange water are input to MIKE 11 as lateral flow.

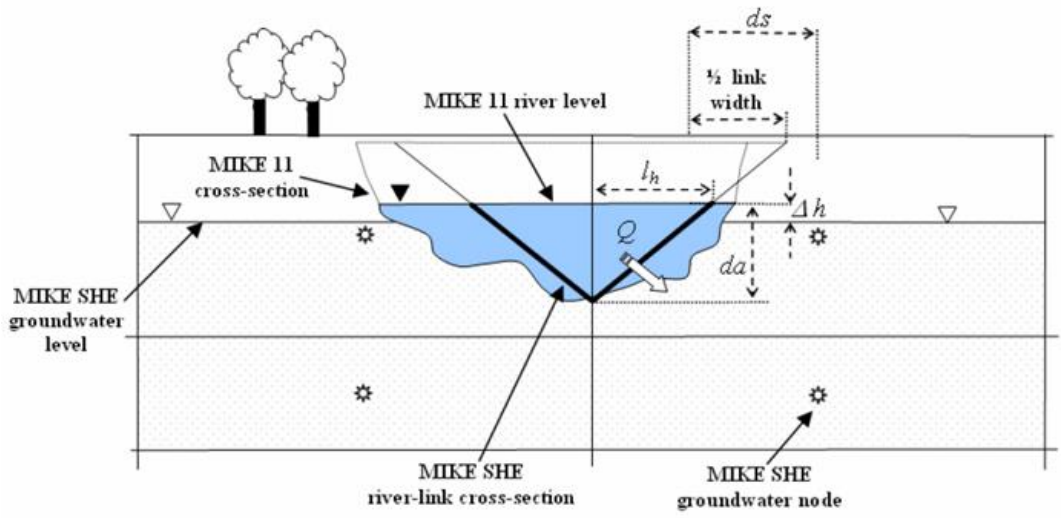

Figure 37 MIKE SHE river link cross-section compared to equivalent MIKE 11 cross section (DHI, 2012).

5.3.5. Saturated Groundwater Flow

MIKE SHE can model saturated groundwater flow in two methods, 3D finite difference scheme similar to MODFLOW or conceptual, linear reservoir method. Since the study area does not contain a productive aquifer system, groundwater utilization in the area is negligible and hydrogeological datasets such as well logs, pumping tests, groundwater levels etc. is not available. Therefore linear reservoir method is used in this study to simulate saturated flow. In this method the catchment is subdivided into sub-catchments and each sub-catchment is represented by shallow interflow reservoirs, deep baseflow reservoirs and the percolation from interflow reservoir. Further each baseflow reservoirs are subdivided into two parallel reservoirs. Water will infiltrate into interflow reservoirs and then percolate into baseflow, which later added to the river as lateral inflow (Fig. 38).

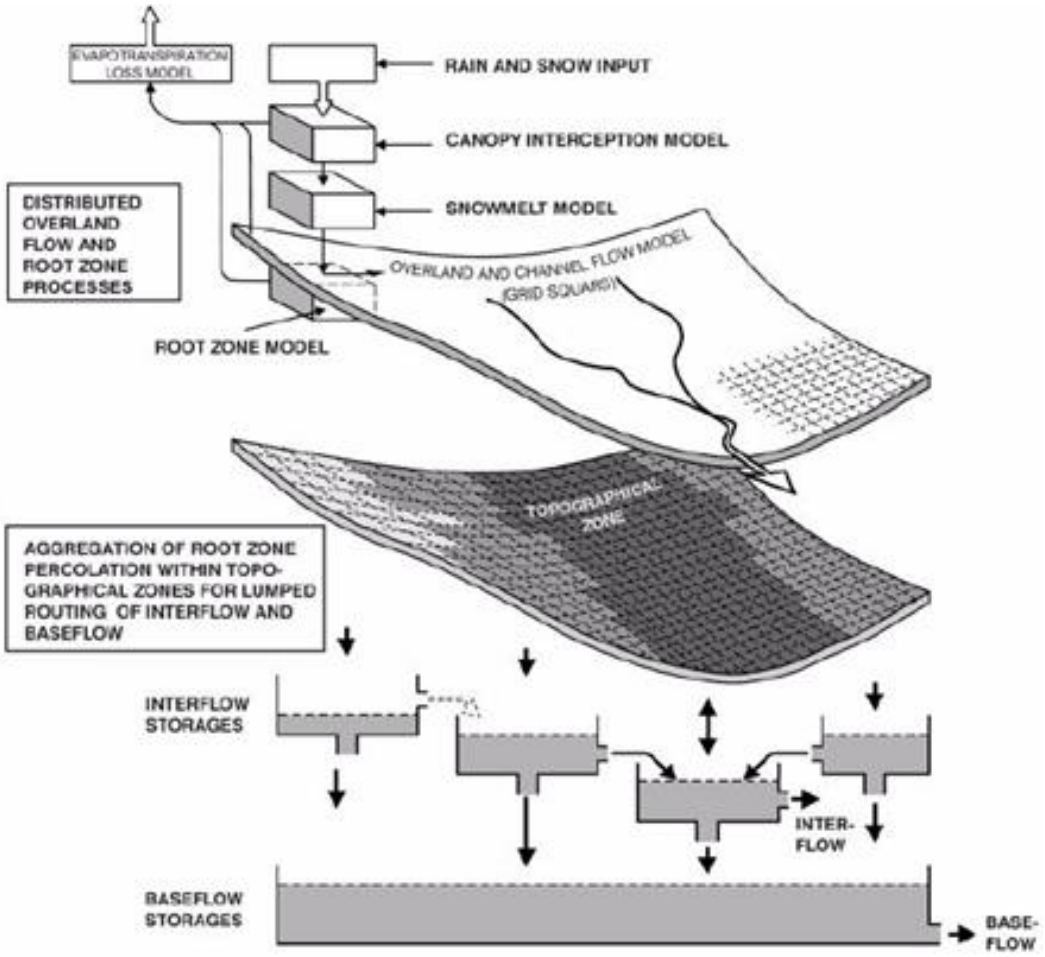

Figure 38 Linear reservoir module of MIKE SHE for saturated zone (DHI, 2012).

Linear reservoir storage is linearly related to the output by a storage constant with the time as:

$$S = kQ \qquad (5.28)$$

where, S: storage in the reservoir

k: time constant

Q: outflow from reservoir

Interflow reservoir is treated as single linear reservoir with two outlets and calculated as:

$$Q_I = (h - h_{thresh})/k_i \quad (5.29)$$

where, h: depth of water in the interflow reservoir

k_i: time constant for interflow

Baseflow reservoir is calculated as:

$$Q_B = \frac{h - h_{thresh}}{k_b} \quad (5.30)$$

where, h: depth of the water in the baseflow reservoir

h_{thresh}: depth of water required before baseflow occurs

k_b: time constant for baseflow

5.4. Study Area

The study area is the Araç Basin, a sub-basin of Filyos Basin located in the West Black Sea Region of Turkey (Fig. 39). The catchment area of the Araç basin is calculated as 854.9 km^2. Araç River flows from west to east in between the city of Kastamonu and Araç town. The outlet of the selected basin is situated in Araç town. Araç river basin is characterized by steep slopes with mountains reaching up to 2400 m in the southern headwaters and 1600 m in the northern headwaters.

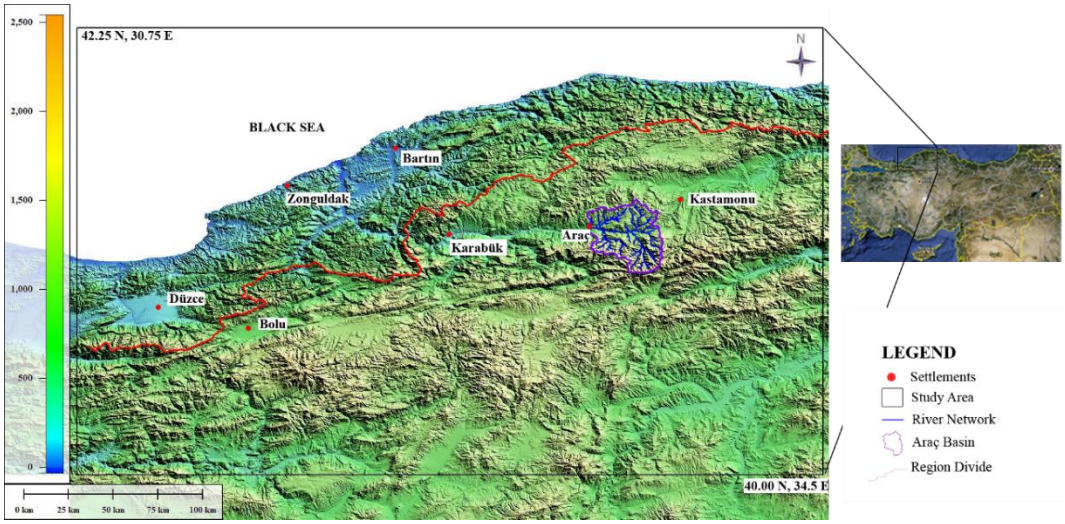

Figure 39 Araç River Basin

Elevation ranges in between 2400 m and 800 m in the basin as can be seen from Figure 40. 90% of the local area elevation ranges in between 800 m and 1600 m and 10% of the local area elevation ranges in between 1600 m and 2400 m.

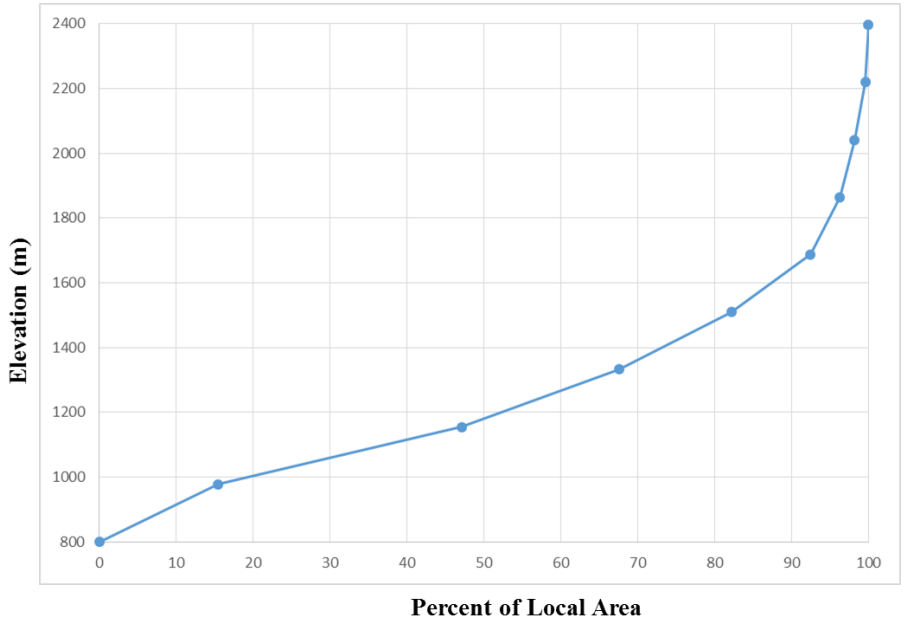

Figure 40 Hypsometric curve of the study region Araç Basin.

5.5. Datasets

5.5.1. Flow Data

There are two stream gauges in Araç River Basin operated by General Directorate of State Hydraulic Works (DSİ). Stream gauge situated on the Başköy stream a tributary of the Araç River, does not have data available for 2007-2011 period for which continuous precipitation datasets are available (Table 6).

Table 6 Stream gauges within Araç Basin. Black boxes represent the period for which data is available.

	Station No	Station Name	Location	Area (km^2)	Available data set				
					2007	2008	2009	2010	2011
Araç River	D13A060	Başköy Stream	Başköy	141					
	D13A061	Araç River	Araç	876					

Daily stream gauge data collected at station Araç River D13A061 is obtained from DSİ for the period 01.01.2007 through 09.05.2011. This station is located at the bridge in the Araç Town and marks the outlet of the Araç Basin for this study. Total runoff can be represented by hydrograph which is usually divided into two components as direct runoff and baseflow (Fig.41).

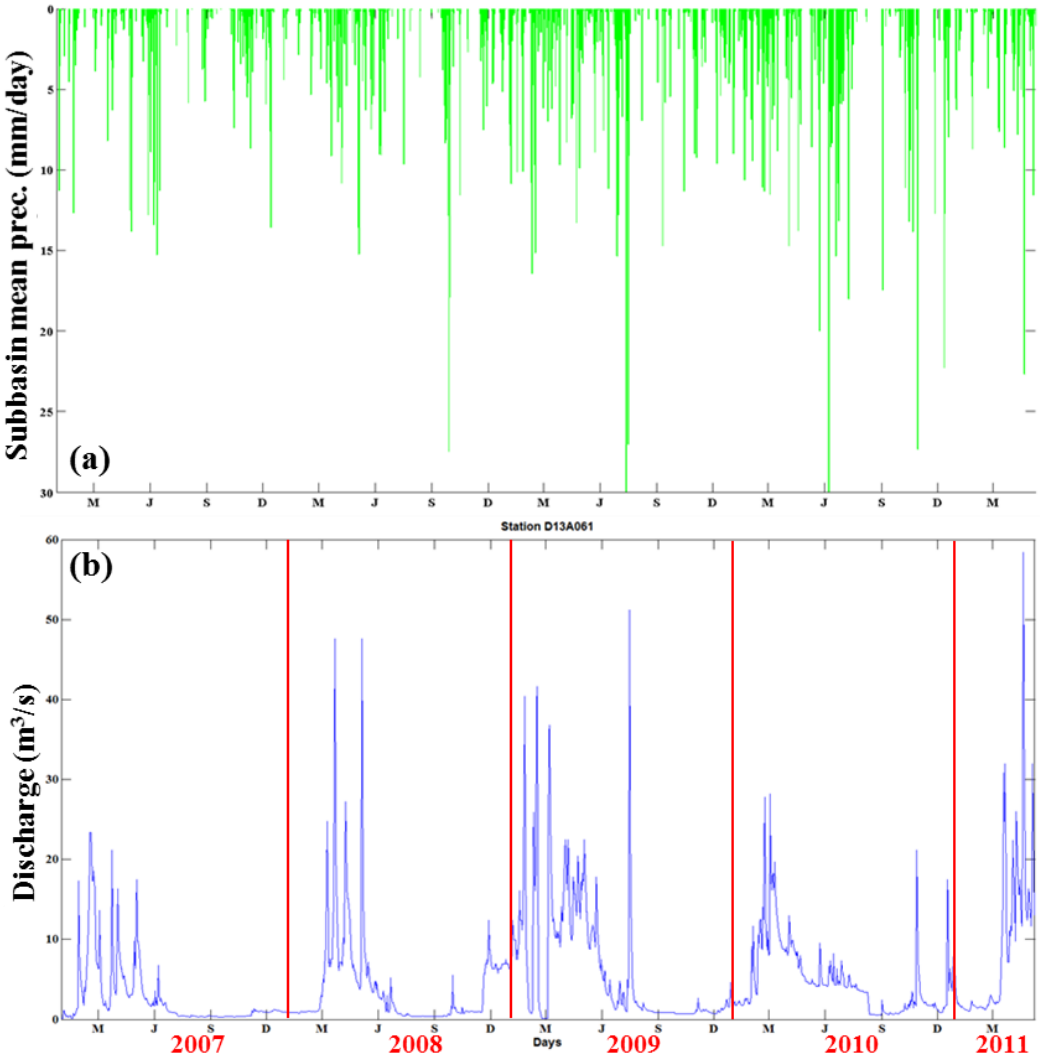

Figure 41 Daily basin mean hyetograph (a) and hydrograph for station D13A061 (b) covering 2007-2011 period.

The implementation of the saturated flow component of the MIKE SHE-MIKE 11 model requires specification of the baseflow recession time constant parameter value, which can be described as the groundwater drainage rate into the stream channel long after precipitation ceases. This drainage can be observed over time in the form of an exponential curve in the hydrograph and as a straight line in the log-transformed hydrograph.

Available data interval for stream gauge D13A061 is plotted in Figure 41. From this figure apparent recession periods are identified as, for example shown in Figure 42. These recession periods are separately plotted on log transformed flow versus time graph in which baseflow recession constants were approximated by the slope of the best fit lines. (Equation 7.1).

$$lnQ = lnQ_0 - at \qquad (5.31)$$

where, Q: flow at some time, t, after the recession has started

Q_0: flow at the start of the recession, i. e. t=0

a: recession constant for the basin (1/time)

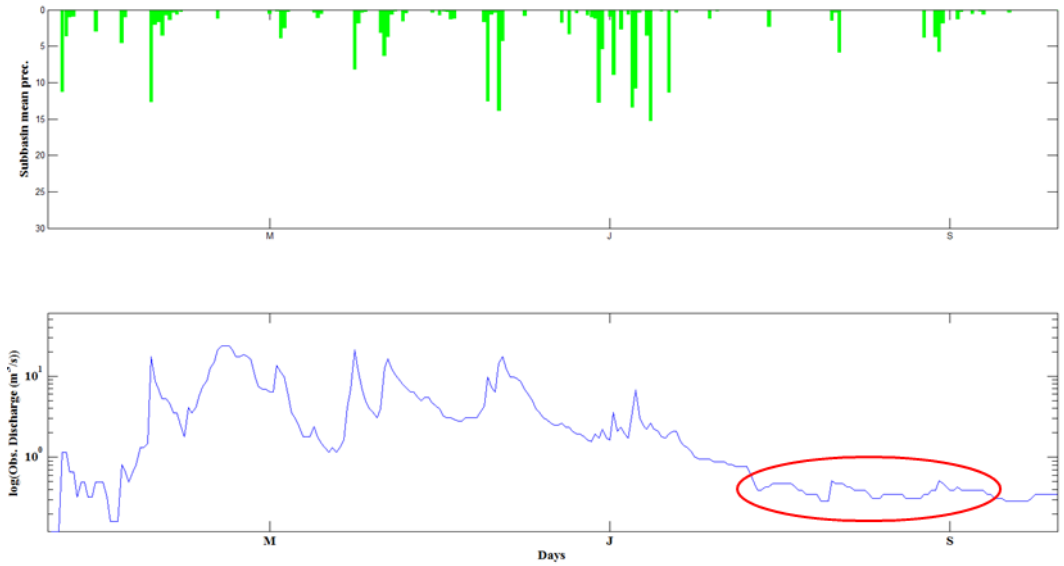

Figure 42 Natural logarithm of daily flows versus time graph for year 2007. Period of data circled by red provide one of the recession curves used to determine baseflow recession time constants.

Chosen recession curve (Fig. 42) is used to determine baseflow recession time constant by plotting natural log of flow versus time graphs and determining slopes of their best fit lines (Fig. 43).

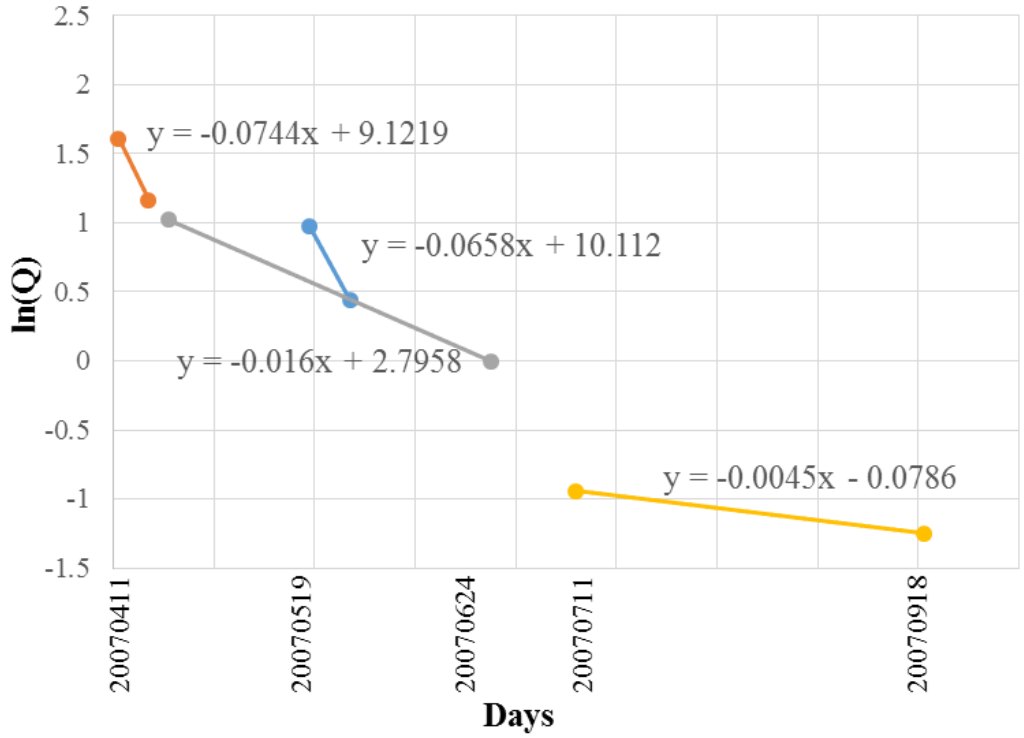

Figure 43 Natural log of flow versus time graph. Slopes of their best fit lines is used to determine baseflow recession time constant.

All these procedures were conducted for 2007-2011 time interval and 11 periods were identified (Table 7).

Table 7 Recession time constants estimated for 2007-2011 period.

Years	Recession time constant (days)	Assigned Runoff type
2007	15.21	Interflow
	13.44	Interflow
	62.59	Baseflow
	222.5	Baseflow
2008	17.64	Interflow
	26.69	Interflow
2009	16.65	Interflow
	16.11	Interflow
2010	59.99	Baseflow
	348.2	Baseflow
2011	24.14	Interflow

To understand the low flow characteristics of this basin baseflow separation is conducted. Automated baseflow separation as described in Arnold et al (1995) is used. In this methodology surface runoff is filtered from baseflow. The filter can be passed over the stream flow data three times as forward, backward and forward. The resulted baseflow separation for water year 2008 and three pass can be seen from following Figure 44.

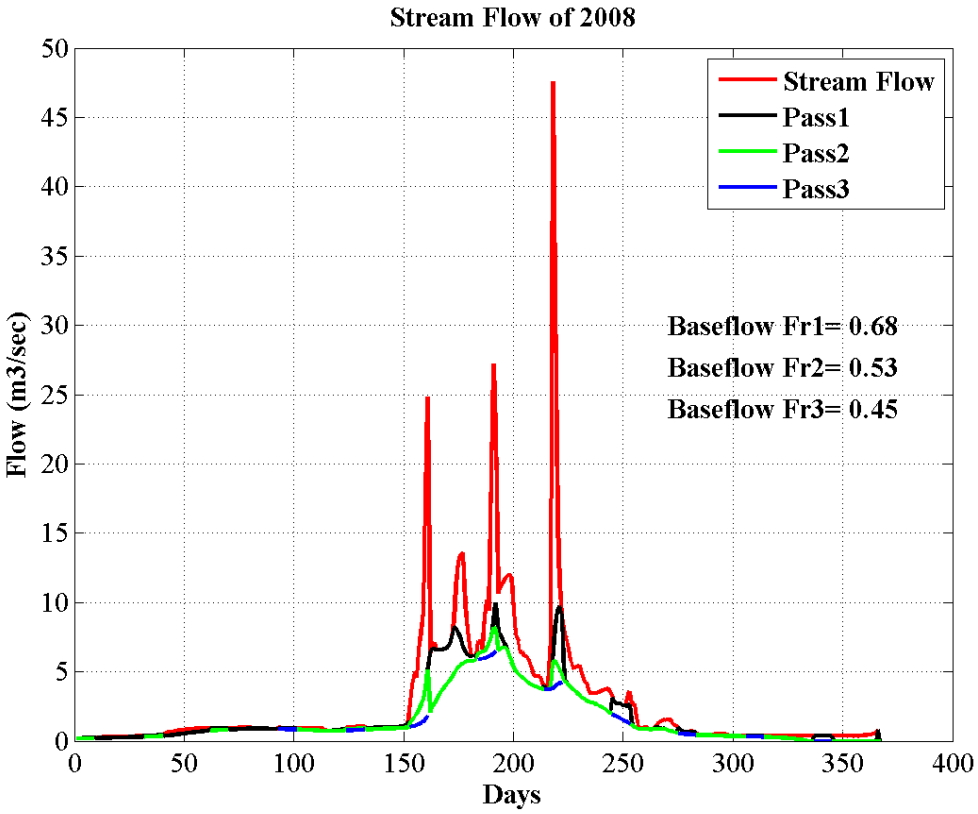

Figure 44 Automated baseflow separation by using digital filter.

Baseflow index for water year 2008 is 45%, which means that stream flows 45% is baseflow. However it should be noted that 2008 water year is a relatively dry year and hence computed baseflow component is relatively high.

5.5.2. Precipitation

Rain gauge gridded precipitation dataset, satellite-based precipitation dataset and bias adjusted satellite-based precipitation datasets are used to drive the model. All these dataset are explained in detail in Chapter 2 & 3. Note that rain gauge based gridded precipitation dataset was used in evaluation and calibration of the hydrologic model parameters. After calibration of the hydrologic model parameters, other precipitation datasets were used and the performance of the flow simulation by the hydrologic model was investigated.

5.5.3. Temperature

Hourly temperature dataset measured by the AWOS type stations is obtained from TSMS. Following table provides the 5 year averaged temperature values for every station in Region 2.

Table 8 5 year averaged temperature values for stations in Region 2.

Station ID	Station Name	Elevation (m)	T_{avg} (^{0}C)
17078	KRA	242	13.6
17618	DVN	1142	7.9
17074	KST	906	10.1
17641	ESK	740	11.1
17648	ILG	859	10.6
17646	CRK	1111	8.6
17650	TSY	869	11.3

5.5.4. Reference Evapotranspiration

The principal atmospheric variables affecting evapotranspiration are radiation, air temperature, humidity and wind speed. Several procedures have been developed to assess the evaporation rate using these parameters (Table 9).

Table 9 Reference evapotranspiration calculation methodologies

Method	Temperature	Solar Radiation	Relative Humidity	Wind speed	Atmospheric pressure	Sunshine hours	Temporal Data Period
Penman	X	X	X	X	X		Daily
Penman-Monteith	X	X	X	X	X		Daily
Kimberly-Penman	X	X		X	X		Daily
Priestley Taylor	X	X					Daily
Hargreaves	X						Monthly
Samani-Hargreaves	X						Monthly
Blanney-Criddle	X		X	X		X	Monthly

The evaporative power of the atmosphere is expressed by the reference crop evapotranspiration (ET_0). The ET_0 represents the evapotranspiration from a standardized vegetated surface. Relating evapotranspiration to a specific surface provides a reference to which evapotranspiration from other surfaces can be estimated. The only factors affecting ET_0 are climatic parameters. ET_0 expresses the evaporating power of the atmosphere at a specific location and time of the year and does not consider the crop characteristics and soil factors.

The FAO Penman-Monteith method is one of the most widely used and recommended method for determining ET_0. This method closely approximate grass ET_0 at a specific location, utilizes physically based equations and explicitly incorporates both physiological and aerodynamic parameters.

Since resistance to diffusion of vapor strongly depends on crop height, ground cover, LAI and soil moisture conditions, the character of reference crop should be well defined and fixed. FAO accepts a hypothetical reference crop with an assumed crop height of 0.12 m a fixed surface resistance of 70 s/m and an albedo of 0.23. FAO Penman-Monteith equation is given by;

$$ET_0 = \frac{0.408\Delta(R_n - G) + \gamma\frac{900}{T+273}u_2(e_s - e_a)}{\Delta + \gamma(1 + 0.34u_2)} \qquad (5.32)$$

where, ET_0: Reference evapotranspiration (mm/day)

R_n: Net radiation at the crop surface (MJ/m^{2}day)

G: Soil heat flux density (MJ/m^{2}day) as the magnitude of the day soil heat flux beneath grass reference surface is relatively small, it might be ignored

T: Mean daily air temperature at 2m height (^{0}C)

u_2: Wind speed at 2m height (m/s)

e_s: saturation vapor pressure (kPa)

e_a: actual vapor pressure (kPa)

e_s-e_a: saturation vapor pressure deficit (kPa)

Δ: Slope vapor pressure curve (kPa/^{0}C)

γ: Psychrometric constant (kPa/^{0}C)

Required meteorological datasets to calculate the ET_0 are temperature, atmospheric pressure, relative humidity, solar radiation and wind speed. All these datasets are obtained from TSMS which are recorded by AWOS type stations at hourly time scale. The variables in Equation 7.2 are calculated as follows:

$$\gamma = 0.665 * 10^{-3} * P \quad (5.33)$$

where, P: atmospheric pressure (kPa)

$$e_s = \frac{e^0(T_{max}) + e^0(T_{min})}{2} \quad (5.34)$$

$$e^0(T) = 0.6108\exp\left(\frac{17.27T}{T+237.3}\right) \quad (5.35)$$

$$e_a = \frac{e^0(T_{min})\frac{RH_{max}}{100} + e^0(T_{max})\frac{RH_{min}}{100}}{2} \quad (5.36)$$

$$\Delta = \frac{4098[0.6108\exp\left(\frac{17.27T_{mean}}{T_{mean}+237.3}\right)]}{(T_{mean}+237.3)^2} \quad (5.37)$$

$$R_n = R_{ns} - R_{nl} \quad (5.38)$$

where, R_{ns}: incoming net shortwave radiation

R_{nl}: outgoing net longwave radiation

$$R_{ns} = (1 - a)R_s \quad (5.39)$$

where, a: albedo, 0.23 for grass

R_s: solar radiation (MJ/m^{2}day)

$$R_{nl} = 4.903 * 10^{-9}\left[\frac{T_{max,K}^4 + T_{min,K}^4}{2}\right](0.34 - 0.14\sqrt{e_a})\left(1.35\frac{R_s}{R_{so}} - 0.35\right) \quad (5.40)$$

where, $T_{max,K}$: maximum absolute temperature during 24 hour period

R_{so}: clear-sky solar radiation

$$R_{so} = (0.75 + 2 * 10^{-5} z) R_a \quad (5.41)$$

where, z: station elevation above sea level (m)

R_a: extraterrestrial radiation (MJ/m^{2}day)

$$R_a = \frac{24(60)}{\pi} 0.0820 d_r [w_s \sin(\varphi) \sin(\delta) + \cos(\varphi) \cos(\delta) \sin(w_s) \quad (5.42)$$

where, d_r: inverse relative distance Earth-Sun

w_s: sunset hour angle (rad)

φ: latitude (rad)

δ: solar decimation (rad)

$$d_r = 1 + 0.033 \cos(\frac{2\pi}{365} J) \quad (5.43)$$

$$\delta = 0.409 \sin(\frac{2\pi}{365} J - 1.39) \quad (5.44)$$

$$w_s = \arccos(-\tan(\varphi) \tan(\delta)) \quad (5.45)$$

where, J: number of the day in year between 1 and 365 or 366

AWOS type stations measures wind speed at 10m above ground, therefore we have to convert this measurement to 2m above ground as follows;

$$u_2 = u_z \frac{4.87}{\ln(67.8z - 5.42)} \quad (5.46)$$

where, z: height of measurement above ground surface (m)

Finally reference evapotranspiration is calculated daily for four stations in and around the Araç Basin (stations Karabük, Kastamonu, Ilgaz and Çerkes). Daily reference evapotranspiration values for Kastamonu station during 2007-2011 time period can be seen in Figure 45.

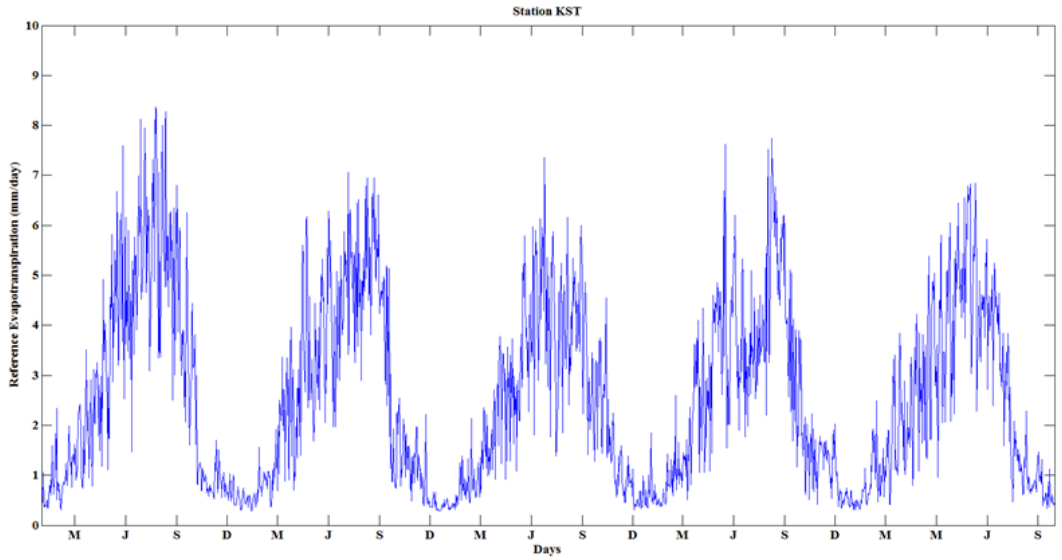

Figure 45 Daily reference evapotranspiration for station Kastamonu calculated by FAO Penmann Montheith method (2007-2011 period).

Reference evapotranspiration values are spatially distributed by using Theissen polygon over the Araç Basin by using four station (Karabük, Kastamonu, Ilgaz and Çerkes). Area of the stations over the Araç Basin for Karabük 47.6%, Kastamonu 23.5%, Çerkes 6.4% and Ilgaz 22.4%.

5.5.5. Topography & River Network

1/25000 scale digital topographic contour maps were obtained from General Directorate of Mineral Research and Exploration. A 10 m resolution DEM was constructed for the study region using these contour maps (Fig. 46). To create the DEM, ArcGIS software was used with the topo to raster interpolation method. This is an interpolation method specifically designed for construction of hydrologically correct DEM and is based on the ANUDEM program developed by Hutchinson et al. (2009, 2011). The river network extracted from 10 m DEM can be seen in Figure 46.

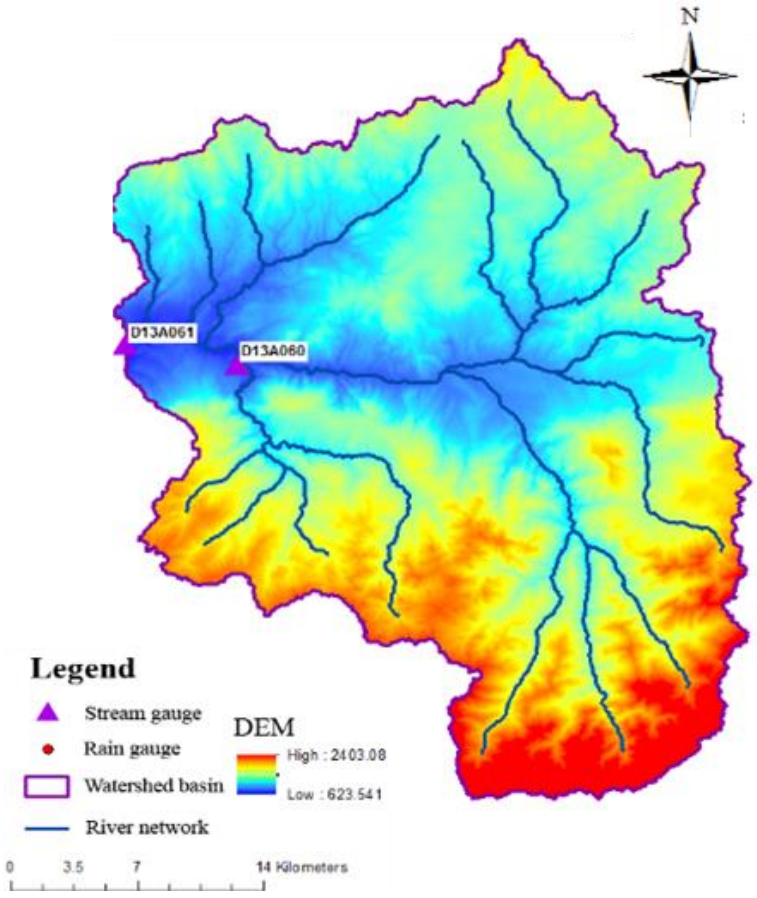

Figure 46 DEM & river network of the Araç Basin.

5.5.6. Land Use/ Land Cover

Land use/land cover classification is obtained from the CORINE land cover dataset. The CORINE land cover 2006 database provides a pan-European inventory of biophysical land cover, using a 44-class nomenclature. It is made available on a 250m by 250m grid database, which has been aggregated from the original vector data at 1:100 000 SCALE. There are, in total, 22 different land cover/land use classification for the Araç basin. However the dataset has been reclassified where similar classifications were grouped, and 8 different classes were obtained (Figure 47, Table 10).

MIKE SHE model requires LAI, RD and Kc values of the vegetation which are determined from the vegetation library provided with the MIKE SHE model. This library

contains seasonal variations of the variables for certain vegetation types except apple tree. Therefore we obtain vegetation development values for apple tree from the literature. For every agricultural product, planting months are determined for Turkey from literature.

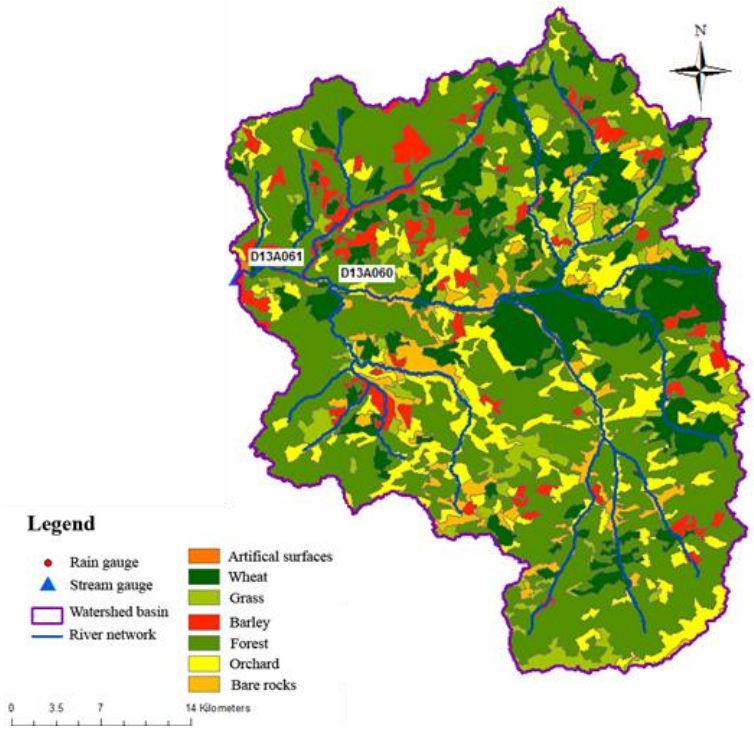

Figure 47 Land Cover/Land Use map of the study region

Table 10 Land use/Land cover classification for study region.

Corine Land Cover Classes	**Area (km^2)**	**%**
Artificial surfaces	0.85	0.09
Crops (Wheat)	162.04	18.57
Crops (Grass)	65.42	7.49
Crops (Barley)	54.49	6.24
Forest	415.12	47.57
Shrub	126.39	14.48
Bare rocks	48.31	5.53
Total area	872.62	

Overland flow module requires specification of detention storage and overland Manning M parameters. Manning's M for overland flow is an effective roughness coefficient that includes the effect of raindrop impact, drag over the plane surface, obstacles such as litter, crop ridges, rocks, erosion and also transportation of sediment. Therefore land use/ land cover conditions are used to determine initial spatial distribution of overland flow Manning's M values. The amount of water must exceed the detention storage value, which is the depth of ponded water so that it can form sheet flow. These values have been developed using land use relationships. Water in detention storage is not available for overland flow but is available for infiltration to the unsaturated zone and evapotranspiration. Initial values for these parameters (Table 11) have been estimated using land use/land cover information and literature review. (Table 11) (Lull 1964; Zinke 1967; Chow 1964; Haan 1982; Earth Tech and DHI 2007; Zhao 2012).

Table 11 Overland Manning M & Detention Storage values classified according to the land cover/land use classes.

Corine Land Cover Classes	Range of Manning's n	Range of Manning's M	Detention Storage (mm)
Artificial surfaces	0.011-0.05	20-90.9	63.5
Crops	0.17-0.48	2.08-5.88	1.5
Evergreen Forest	0.2-0.8	1.25-5	31.8
Deciduous Broadleaf Forest	0.2-0.8	1.25-5	31.8
Bare rocks	0.01-0.033	30.3-100	1-5

5.5.7. Soil

Soil map of the study region is obtained from Turkish National Soil database inventory which is available at 1/25000 scale. Turkish Soil database classifies the soils within the study region as alluvial soil, colluvial soil, brown forest soil, rendsina and vertisol. Unsaturated zone module requires the values of the soil hydraulic parameters such as water content at saturation, wilting point, field capacity and saturated hydraulic conductivity. Since Turkish Soil database does not contain these required parameters, or information such as soil texture values to derive these parameters. The values estimated by Tombul et al (2004) were utilized in this study. Tombul et al (2004) utilized several pedotransfer functions to estimate soil hydraulic properties for loam, sandy clay loam and sandy loam soil textures in Kurukavak Creek subbasin located in Sakarya Basin. These soil textures were overlain with the Turkish soil database map and the soil groups within the Araç Basin were reclassified (Fig. 48) based on the soil texture descriptions provided by Tombul et al (2004). As a result soil hydraulic properties listed in Table 12 were used in this study as initial parameters.

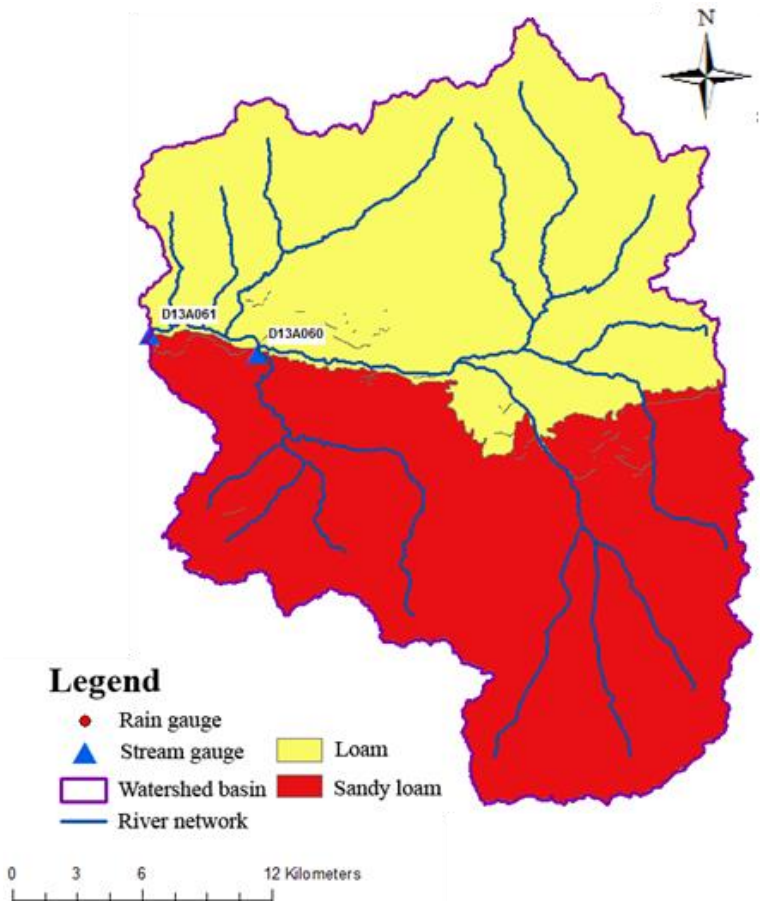

Figure 48 Soil map of the Araç Basin

Table 12 Soil hydraulic properties for the study region

	Water content at saturation (Q_{sat})	Water content at field capacity (Q_f)	Water content at wilting point (Q_w)	Saturated hydraulic conductivity (K_{sat} (m/s))
Loam	0.47	0.362	0.172	$0.264x10^{-5}$
Sandy loam	0.46	0.338	0.168	$0.286x10^{-5}$

Unsaturated zone module requires capillary fringe thickness which is then added to the root depth to define the thickness of Layer 1 in the Two-Layer Water Balance evapotranspiration/unsaturated zone method. Capillary fringe depends on soil type, in coarse to medium sands, the capillary fringe is typically less than 10cm. In fine sands and silts, the capillary fringe could be a half a meter or more. Capillary fringe thickness values

for loam and sandy loam are obtained from literature (Table 13) (Richardson and Vepraskas, 2000).

Table 13 Capillary fringe values for different soil classes.

Soil classes	ET surface depth (cm)
Loam	25
Sandy loam	15

5.5.8. Geology

Geological map of the study region is determined from General Directorate of Mineral Research and Exploration at 1/25000 and 1/100000 scales, where the latter comes with a report describing the geological units and structures present in the map coverage.

Regional Geology

Study region is located along Safranbolu Basin and Araç-Daday Belt which reside in Sakarya Composite Terrane. Sakarya Composite Terrane is extending along 100-200 km east-west trending belt, covering almost the entire northern Anatolia (Goncuoglu, 2010). According to Goncuoglu the lower part of the overstep sequence is Early Jurassic in age, followed by a more or less continuous succession of Jurassic-Cretaceous platform sediments. From Late Cretaceous onward, slope-type sediments dominate, which in turn were covered by flysch-type deposits with ophiolitic blocks.

Local Geology

The most characteristic feature in the area is the basalt-andesite formations. They cover the middle of the study area dominantly. Along the margins ophiolitic rocks are widely observed, especially at the Northern part alteration of schist, serpentinite, migmatite, gneiss, metagranite and marble are dominant. Marble in the study region is observed as massive and have moderate thickness. At Southern part of the overthrust structure where ophiolitic rocks are in contact with the limestone, clastic and basalt-andesite alluvial fan and slope debris are observed. At the western part of the study region, near Araç limestone

and clastic rocks can be observed. Moreover clastic rocks extend towards the East of the study region which are observed on top of the basalt-andesite formation. Faults examined in Araç Basin stretch in the E-W direction. The longest fault enters the study region near Araç and stretches to Akkaya. Over-thrust structures are observed at the North of the study region (Uğuz and Sevin 2011). As seen from the geologic map of the study area (Fig.49), there are 11 different geological units.

Sakızdağ formation contains conglomerate, sandstone, mudstone and gypsum overlay all formations by unconformity. Ilıca formation mainly contains limestone, sandstone and marl. Ilıca formation has two members, these are clastic member and Akyörük volcanic member. Clastic member contains sandstone and mudstone in which sandstone is poorly graded and well rounded. Akyörük volcanic member contains basalt, andesite, tuff and agglomerate. Kavak formation contains sandstone, conglomerate, siltstone, mudstone, chert, clayey limestone and volcanic where volcanic in this formation is andesite lava flows. Kavak formation overlain ophiolities and overlain by metamorphic by angular unconformity. Bekirli formation contains sediment origin phyllite, schist, metadiabase and marble blocky in places. Başakpınar metacarbonate contains calcite marble and dolomite marble.

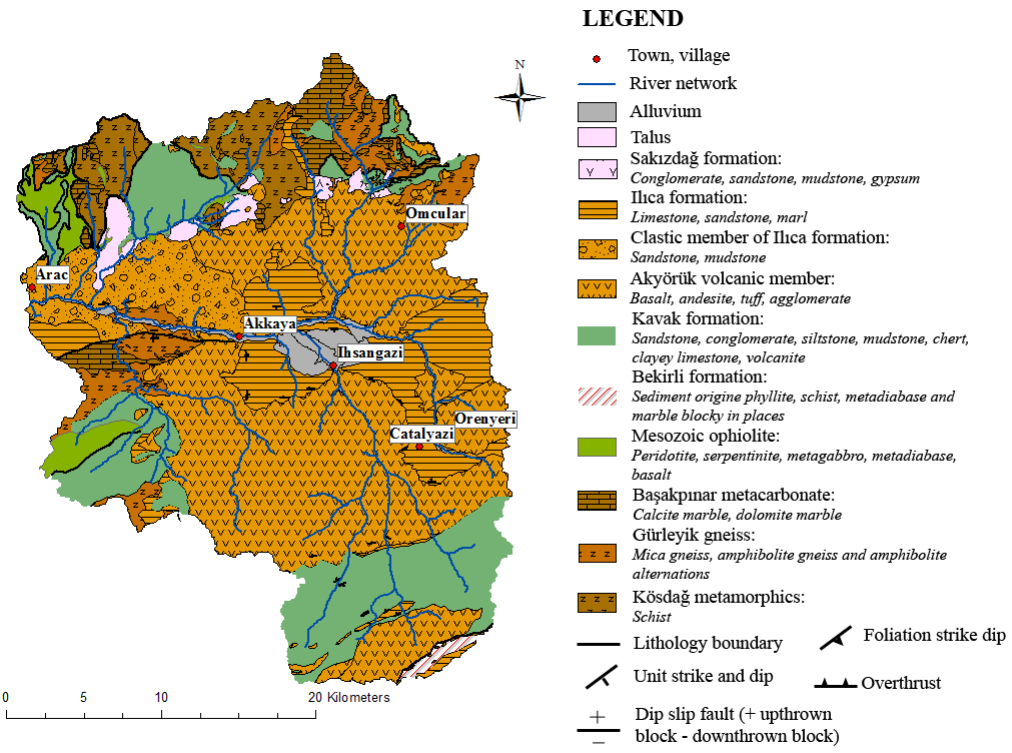

Figure 49 Geological map of the study region (Uğuz and Sevin, 2011).

5.5.9. Hydrogeology

Hydrogeological information about the study area is mainly obtained from the "Hydrogeological Investigation Report for Kastamonu, Araç Plain" report published by DSI (1968). Moreover 1/500000 scale national hydrogeological map was also obtained from DSI. According to the DSI Report (1968) geological units in the Araç Basin do not contain significant amount of groundwater. Metamorphic series including schists and marbles were classified as impervious. Flysch series comprised of conglomerate and marn alternation are poor in groundwater; however, they feed a large number of low-yield springs at locations where permeability contrasts occur. Eocene aged limestone is perhaps the most significant source of groundwater due to the karstic features and fractures. Most of the springs in the region originate from the contact between limestone and the

ophiolites with yields up to 80 lt/sec. Table 14 lists the groundwater potential of the geological units present in the study area based on the 1/500000 scale hydrogeological map. Considering this information together with the hydrogeological classification of the geological units described by the DSI (1968) report a hydrogeological map of the study region is constructed (Fig. 50).

Table 14 Groundwater potential of the geological units based on 1/500000 hydrogeological map of Turkey.

Groundwater potential	**Lithology**	**Degree of groundwater productivity**
Formation containing local groundwater	Limestone	Poor
Formation not containing groundwater	Metamorphic series	Very poor
Formation not containing groundwater	Ophiolitic series	Very poor
Formation containing local groundwater	Flysch	Poor
Formation not containing groundwater	Andesite	Very poor
Formation containing local groundwater	Clay, sand, gravel	Poor

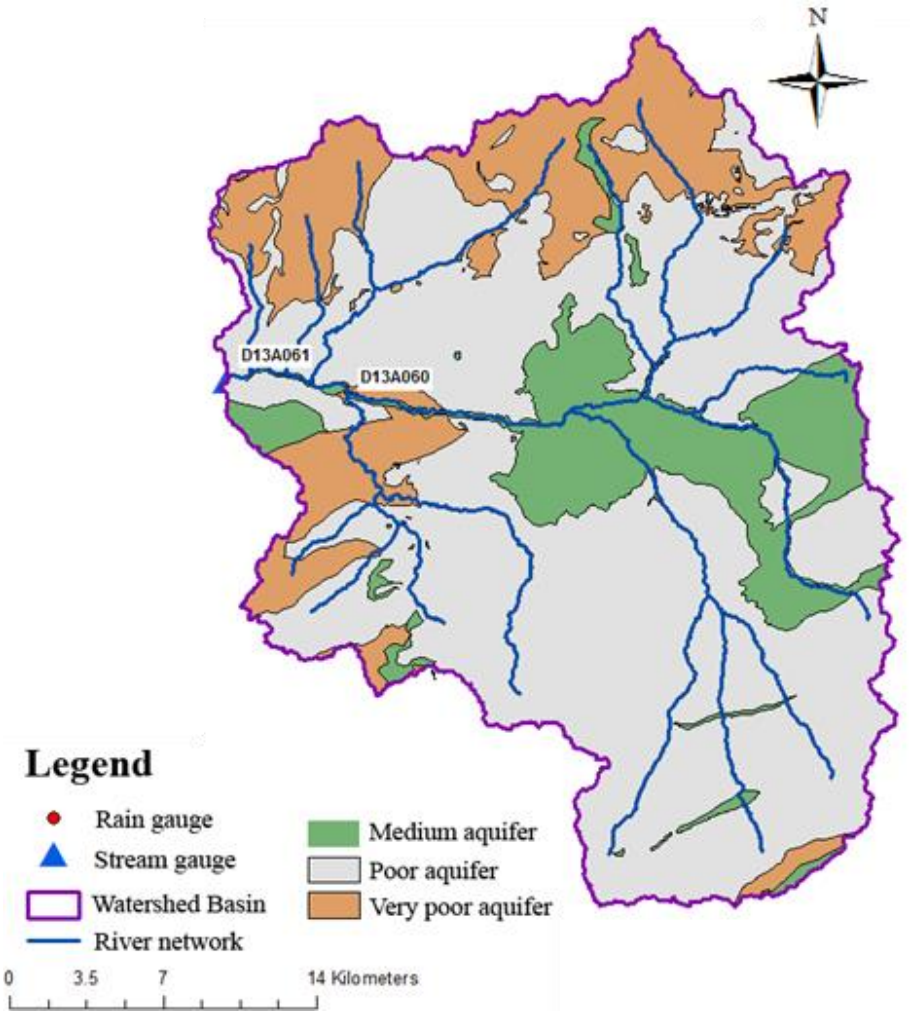

Figure 50 Hydrogeological map of the Araç Basin.

5.5.10. Cross Sections

MIKE 11 module requires channel cross section information to calculate discharge values.11 channel cross sections were surveyed during a field trip held in 21-23 March 2014 (Fig. 51).

Figure 51 Picture showing measurement of a channel cross section along Araç River during a field trip held in 21-23 March 2014.

However MIKE 11 requires at least two cross section for every branch. For the remaining branches at least two trapezoidal cross sections are taken from the 10 m DEM. In total 34 cross sections are input to the model. To compare the cross sections surveyed in the field and obtained from the DEM Figure 52 is plotted. It can be seen that the general cross section information are somewhat similar while the DEM lacks the local details as expected.

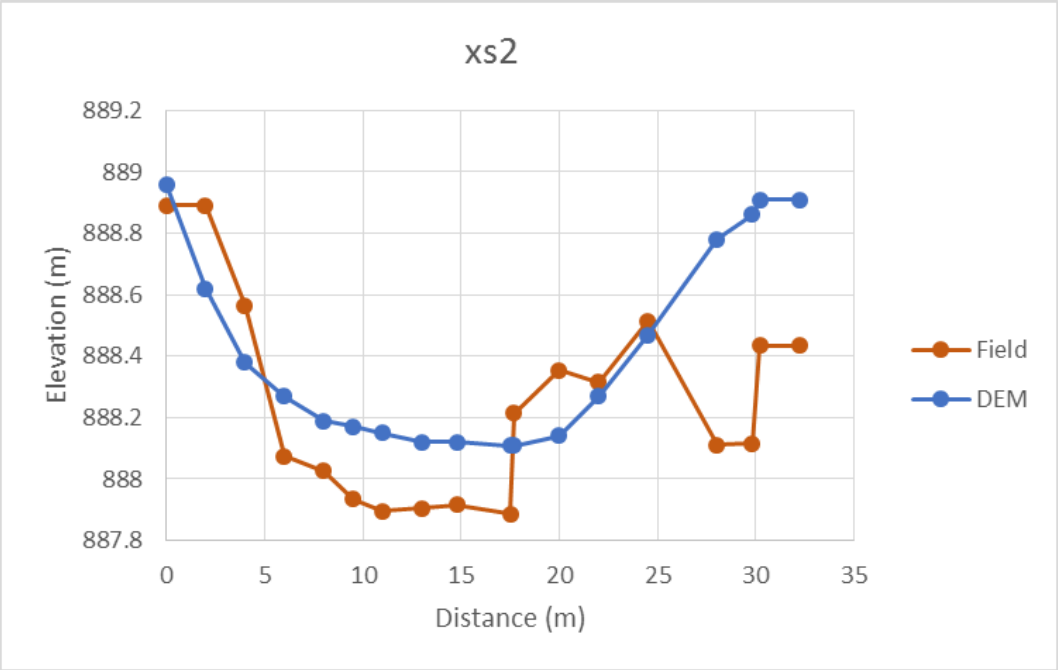

Figure 52 Comparison of surveyed cross section with that of constructed from 10m DEM.

5.5.11 Initial Model Setup

MIKE SHE model is setup for the Araç Basin using a 110x150 square grids with 350m resolution. Data inputs were explained in detail earlier in this Chapter. Parameters of the MIKE SHE-MIKE 11 utilized in this study are summarized in Table 15. After determining initial values for the parameters, their lower and upper bounds are determined from the literature.

Table 15 Parameters of the MIKE SHE-MIKE 11.

Parameters		**Initial Value**	**Lower Bound**	**Upper Bound**
Degree day coefficient	Ddc	2 mm/C/d	1	15
Manning M (overland flow)	Mo	Spatial distributed	1.25	65.15
Detention Storage	DS	Spatial distributed	1.5	63.5
ET Surface Depth	ETsd	Spatial distributed	15	30
Manning M (channel)	Mc	25	12	50
Groundwater depth (m) (relative to ground)	Gwd	-10	-20	0
Soil (L) water content at saturation	WtS	0.47	0.44	0.61
Soil (SL) water content at saturation	WtS	0.46	0.44	0.61
Soil (L) water content at field capacity	WtF	0.362	0.15	0.44
Soil (SL) water content at field capacity	WtF	0.338	0.15	0.44
Soil (L) water content at wilting point	WtW	0.172	0.09	0.26
Soil (SL) water content at wilting point	WtW	0.168	0.09	0.26
Soil (L) saturated hydraulic conductivity	Shc_L	$0.264x10^{-5}$	10^{-9}	10^{-5}
Soil (SL) saturated hydraulic conductivity	Shc_SL	$0.283x10^{-5}$	10^{-9}	10^{-5}
Specific Yield of interflow (loam)	SYint	0.2	0.15	0.25
Specific Yield of interflow (sandy loam)	SYint	0.27	0.17	0.31
Initial Depth for interflow (loam)	Dinintl	5 (m)	2	15
Initial Depth for interflow (sandy loam)	Dinintl	5	2	15
Bottom & Threshold Depth for interflow (loam)	DbotIn	5 (m)	0.5	15
Bottom & Threshold Depth for interflow (sandy loam)	DbotIn	5	0.5	15
Interflow time constant (loam)	Tint	3 (day)	1	40
Interflow time constant (sandy loam)	Tint	2	1	40
Percolation time constant (loam)	Tperc	4 (day)	1	40
Percolation time constant (sandy loam)	Tperc	3	1	40
Fraction of percolation (medium aquifer)	Frac	0.5	0	1
Fraction of percolation (poor aquifer)	Frac	0.5	0	1
Specific Yield of baseflow 1&2 (medium aquifer)	Sybase	0.25	0.15	0.4
Specific Yield of baseflow 1&2 (poor aquifer)	Sybase	0.1	0.05	0.15
Time constant for baseflow 1 (medium aquifer)	Tbase1	20 (day)	20	80
Time constant for baseflow 1 (poor aquifer)	Tbase1	20 (day)	20	80
Time constant for baseflow 2 (medium aquifer)	Tbase2	85 (day)	80	350
Time constant for baseflow 2 (poor aquifer)	Tbase2	85 (day)	80	350
Subtract constant to calculate Initial Depth for baseflow 1&2 (medium aquifer)	DiniBt	1 (subtraction)	0	5
Subtract constant to calculate Initial Depth for baseflow 1&2 (poor aquifer)	DiniBt	1	0	5
Bottom & Threshold Depth for baseflow 1&2 (medium aquifer)	DbotBt	50	20	80
Bottom & Threshold Depth for baseflow 1&2 (poor aquifer)	DbotBt	50	20	80

To evaluate the model first inconsistencies in the initial model setup were investigated. Simulated flow vs observed flow through 2007-2011 can be seen from the Figure 53.

Statistics of percent bias (BIASP), Nash–Sutcliffe model efficiency coefficient (NSE) and correlation (CORR) between observed and simulated discharge can be seen in Figure 53b. It is clear that model overestimates discharge by 15%. Since precipitation dataset is already quality controlled inconsistency in overall bias is further investigated using the evapotranspiration estimates.

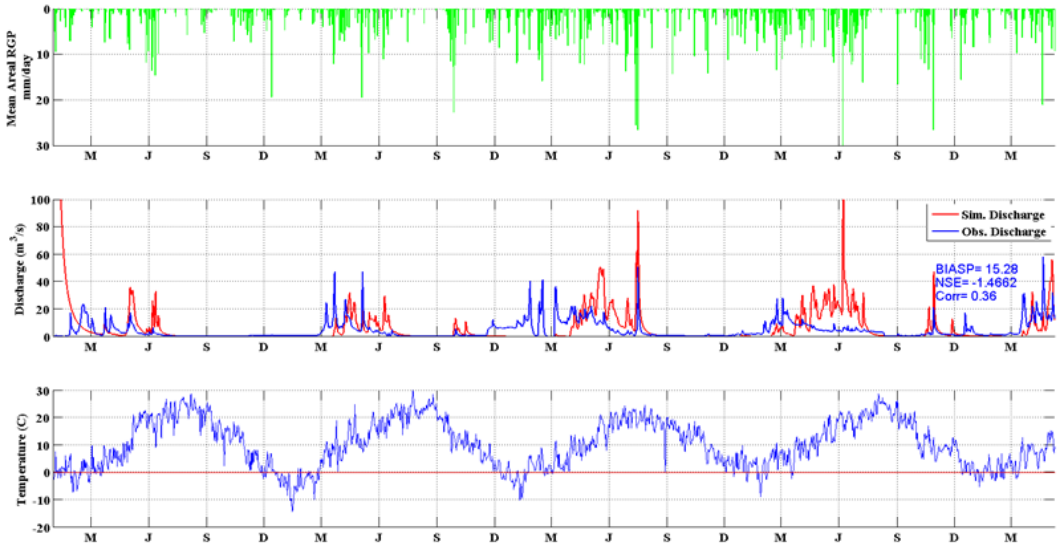

Figure 53 Simulated discharge of initial model setup. (a) mean areal RGP data of Araç Basin, (b) simulated (red) vs. observed (blue) streamflow and (c) mean temperature of Station Ilgaz and Kastamonu.

As it is mentioned in detail earlier that reference evapotranspiration is calculated by FAO Penmann Monteith equation and further this value is converted to evapotranspiration by using two layer water balance methodology in MIKE SHE model. Reference evapotranspiration input to the model is performed by station based datasets, therefore there is a chance that these four stations might not fully represent the basin reference evapotranspiration values. Therefore to understand the long term behavior of the initial model annual major water balance components such as precipitation, streamflow and evapotranspiration are plotted in Figure 54. Note that water balance components are calculated for water years.

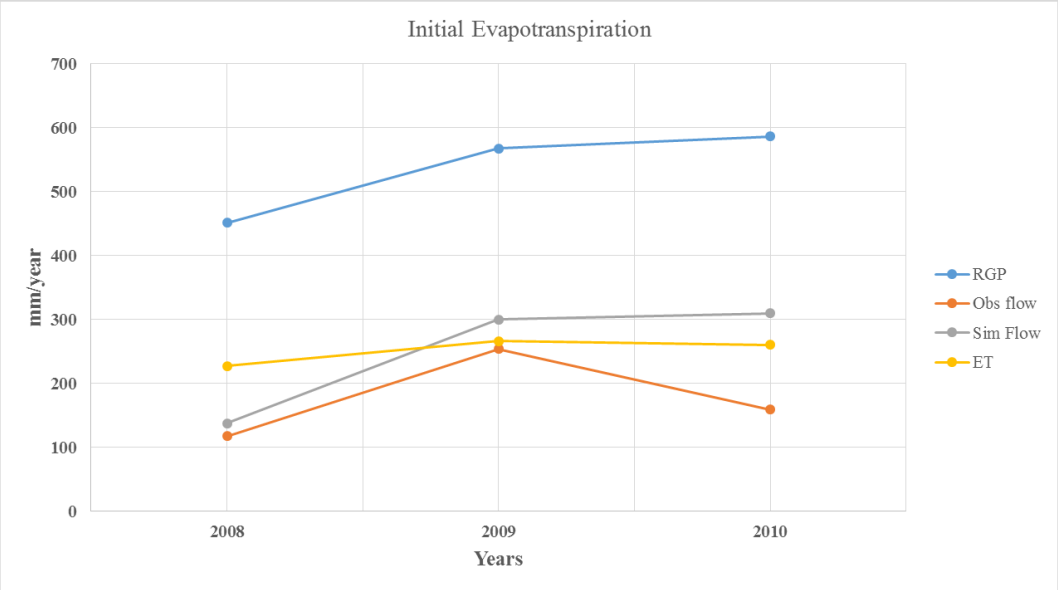

Figure 54 Annual variation of major water balance components (RGP: mean areal rain gauge gridded precipitation of Araç Basin, Obs flow: observed flow of stream gauge located at the outlet of the Araç Basin, Sim flow: simulated flow and ET: evapotranspiration by using FAO Penmann Monteith equation

It is clear that simulated discharge consistently overestimates observed discharge which likely indicate that initial calculated reference evapotranspiration value is not high enough to match the long term simulated flow with the observed flow. Therefore all four stations reference evapotranspiration is multiplied by a factor of 1.3 Figure 55.

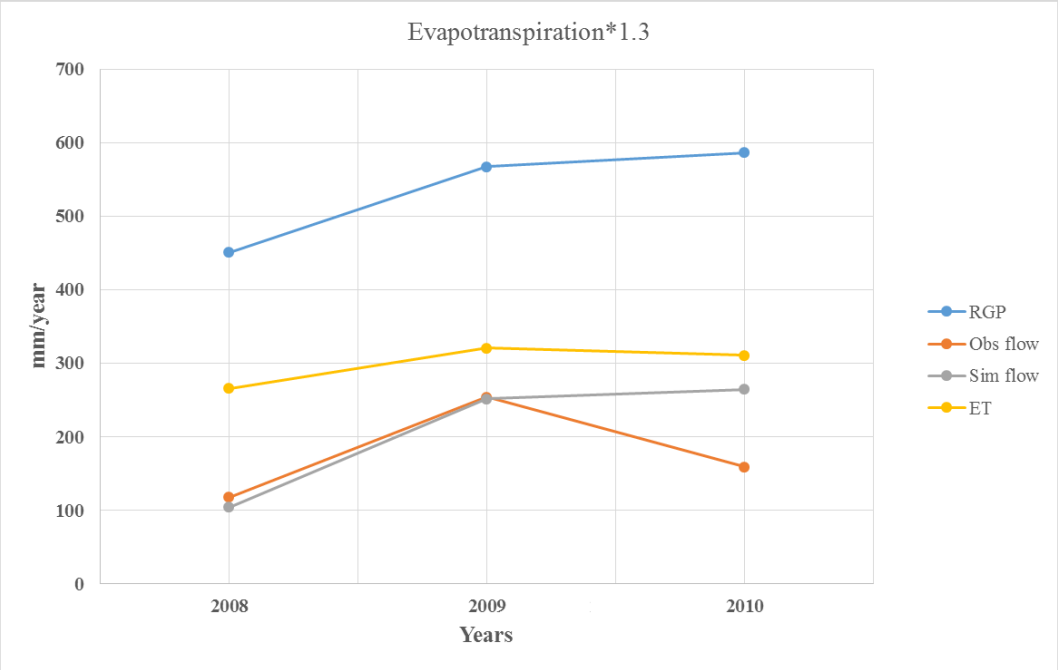

Figure 55 Annual variation of major water balance components (RGP: mean areal rain gauge gridded precipitation of Araç Basin, Obs flow: observed flow of stream gauge located at the outlet of the Araç Basin, Sim flow: simulated flow by reference evapotranspiration multiplied by 1.3 and ET: evapotranspiration.

After adjusting the ET component simulated and observed flows in years 2008 and 2009 match much better than the initial value (Fig. 54). Therefore reference evapotranspiration is updated for four station by multiplying with a factor of 1.3.

After these checks it is clear that initial model setup still consist of significant bias. Remaining bias could be due to specification of initial states, biases in meteorological datasets and incorrect model parameterization. However remaining bias is assumed to be incorrect specification of the model parameter fields. Therefore next step of this study is to determine which parameter is incorrectly specified and responsible for the bias among other performance measures.

5.6. Calibration of the Model Parameters by Diagnostic Evaluation Methodology

Physically based models require a significant amount of data and time to solve equations and their inherent complexity may potentially lead to over parameterization. Determining all these parameters might not be possible in data sparse regions and obtaining from similar basins might lead to incorrect specification of the model parameter fields. Or else generalizing over large basins without taking into account of the heterogeneity raises many difficulties. Therefore these initial parameter values should be refined. There are variety of model calibration techniques however pinpointing the causes of model inadequacies and providing meaningful guidance to improve model is still not fully understood (Gupta et al. 2008). Most of the calibration methodologies do not point toward the causes of the poor model performance (diagnostic power) but simultaneously adjust all parameters so to optimize an aggregate measure of the model fit (e.g. RMSE) to the observed data (Duan et al. 1992). These methodologies can improve the model result for wrong reasons. There is a significant amount of parameters all of which has varied influence on model output and differentiation of these influences by single regression-based aggregate measure of performance in general is weak (Gupta et al. 1998, 2008 and Wagener and Gupta 2005).

Automated model calibration procedures rely on a single statistical measure (e.g. RMSE) and often lead to ill-posed parameter values due to projection of the high dimension of the data set down to single dimension of the residual-based summary statistics. Statistical metrics only measure the (weighted) distance between observed and simulated runoff and fail to incorporate diagnostic information regarding to causes of poor model performance. Dynamic aspect of hydrological model can be evaluated by hydrologically-relevant metrics that enable quantitative evaluation of the hydrological behavior.

In this study to evaluate the performance diagnostic evaluation methodology is used incorporating hydrologically relevant metrics and in model evaluation and calibration.

5.6.1. Diagnostic Approach

Diagnostic model evaluation approach is capable of pinpointing inadequacies in model performance, parameters that cause problems and specific aspects of model structure.

Basis for diagnostic model evaluation is derivation of hydrologically-relevant summary metrics and/or signature patterns in the observed/simulated data derived, for example, from flow duration curve (FDC). FDC summarizes catchments ability to produce discharge values of different magnitudes. Derivation of hydrologically-relevant summary metrics can be conducted from primary functions of any watershed. These watershed functions can be listed as partitioning, storage and release (Yilmaz et al. 2008, Wagener et al 2007) (Fig. 56).

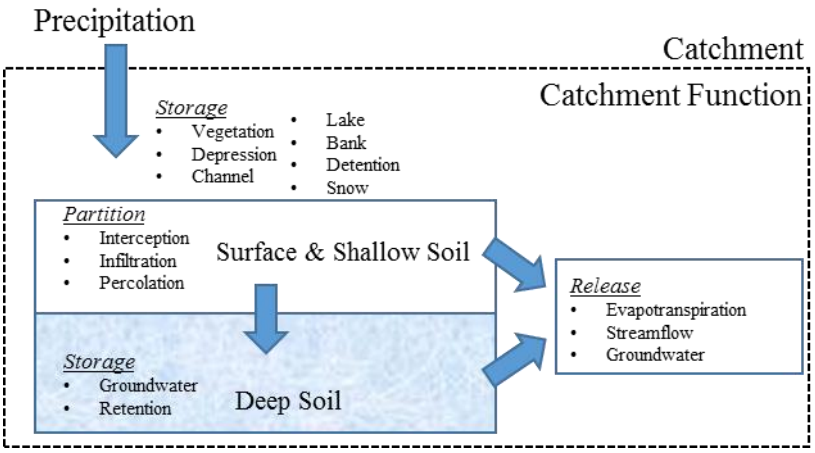

Figure 56 Primary functions of watershed system.

In this study signature measures related to primary watershed functions are determined by considering to;

- maintain overall water balance
- vertically redistribute excess rainfall between faster and slower runoff components
- redistribute runoff in time (Yilmaz et al. 2008)

Signature measure related with overall water balance can be determined by considering characteristic watershed behavior at longer time scales. Signature measure related with

vertical redistribution can be determined by characteristic watershed behaviors at shorter time scales and flow timing.

Signature measure related to overall water balance

To evaluate violations in the overall water balance of the catchment Yilmaz et al. (2008) used percent bias in overall runoff ratio (%BiasRR) as diagnostic signature measure (Equation 7.17). Since this measure can be characterized at longer time scale, it is highly sensitive to climatic variability of evapotranspiration. Therefore parameters controlled by evapotranspiration are more sensitive to this signature measure. These parameters can be soil water content at saturation, soil water content at field capacity, soil water content at wilting point, saturated hydraulic conductivity, ET surface depth and detention storage.

$$\%BiasRR = \frac{\sum_{t-1}^{N}(QS_t - QO_t)}{\sum_{t=1}^{N} QO_t} x100 \qquad (5.47)$$

where, QS: simulated flow

QO: observed flow

Signature measure related to vertical soil moisture redistribution

Vertical redistribution of excess precipitation are characterized by overland flow, runoff, interflow and primary and secondary baseflow. These processes performance can be determined from streamflow hydrograph as fast and slow runoff process. Since these processes are not time dependent, their responses can be best observed from FDC. To determine fast and slow runoff processes FDC is divided into three segments. Heavy precipitation event's responses can be detected from high-flow segment of FDC. Moderate size precipitation events, primary and secondary baseflow relaxation response of the watershed can be detected from mid-segment of FDC. Interaction of baseflow with evapotranspiration during dry period can be detected from low-flow segment of FDC. Moreover FDC slope indicates flashy or slow response of watershed. If FDC slope is steep this indicates that watershed has flashy response however if slope is flatter watershed has slow and more sustained groundwater flow response.

All these FDC properties can be used as signature index for model evaluation and calibration. Vertical redistribution of soil moisture signature measure is defined from slope of FDC mid-segment (Yilmaz et al. 2008). Yilmaz et al. (2008) also find out that volume of water of high flow segment provide information about vertical redistribution of soil moisture. Vertical redistribution signature measures used in this study are percent bias in FDC mid-segment slope (%BiasFMS) and the percent bias in FDC high-segment volume (%BiasFHV).

$$\%BiasFMS = \frac{[\log(QS_{m1}) - \log(QS_{m2})] - [\log(QO_{m1}) - \log(QO_{m2})]}{[\log(QO_{m1}) - \log(QO_{m2})]} x100 \qquad (5.48)$$

where, m1: lowest flow exceedance probability (0.2)

m2: highest flow exceedance probability (0.8)

$$\%BiasFHV = \frac{\sum_{h=1}^{H}(QS_h - QO_h)}{\sum_{h=1}^{H} QO_h} x100 \qquad (5.49)$$

where, h=1,2,…H flow indices for flows with exceedance probabilities lower than 0.04

Signature Measure Related to Behavior of Long-Term Baseflow

Total volume of low flow segment is index for long-term baseflow response. Yilmaz et al. (2008) defined long-term baseflow signature measure to be the percent bias in FDC low-segment volume (%BiasFLV).

$$\%BiasFLV = -1x \frac{\sum_{l=1}^{L}[\log(QS_l) - \log(QS_L)] - \sum_{l=1}^{L}[\log(QO_l) - \log(QO_L)]}{\sum_{l=1}^{L}[\log(QO_l) - \log(QO_L)]} x100 \qquad (5.50)$$

where, l=1,2,…L index of flow value located within the low-flow segment (0.8-1.0 flow exceedance probabilities) of the flow duration curve, L being the index of the minimum flow.

Signature Measure Related to Snow Melt & Timing

Signature measure commonly used to evaluate hydrograph timing is linear correlation coefficient between observed and simulated runoff. Therefore our signature measure to determine hydrograph timing is the correlation coefficient (CORR).

5.7. Results

5.7.1. Model Driven by RGP Dataset

In the diagnostic model evaluation process a sensitivity analysis was performed using by hydrologically meaningful signature measures described earlier. Sensitivity analysis was performed by generating random parameter sets within the pre-defined interval between upper and lower boundaries of the parameters, see Table 15 and consequently running MIKE SHE-MIKE 11 model for each of the sampled parameter sets. It should be noted that 2007/01/01-2007/09/30 period was set as warm up period and signature measures were calculated for the 2007/10/01-2010/03/24 period. The period between 2010/03/25-2011/05/09 was left for evaluation. Prior to the sensitivity analysis, based on the understanding of the hydrologic processes and the model structure it is expected that the parameters controlling baseflow should be sensitive to the low flow measure, %BiasFLV, those controlling interflow should be sensitive to high flows, %BiasFHV, the degree day coefficient parameter should be sensitive to the timing, CORR, and the soil hydraulic parameters to %BiasRR due to ET control.

Initially 360 random parameter sets were generated and for every parameter set model was run and signature measures were calculated from the simulated and observed stream flow values. The results are presented in Fig. 57. Note that each gray colored point in these plots represent a sampled parameter within the defined parameter range with a total of 360 sampled sets in this case. The dashed lines indicate the 25% and 75% quantile (solid line indicates the median) of the signature measure distributions [computed using a binning technique; see Yilmaz et al, 2007]; the region between the two dashed lines contains 50% of the sampled points. The orientation of this region indicates the existence, or not, of a relationship between the signature measure and the parameter whereas a horizontal region indicates no relationship. From the results of the sensitivity analysis it

is clear that water content at field capacity for sandy loam (Fig. 57a) is sensitive to the %BiasRR since it affects the evapotranspiration rate and hence overall water balance. It can be seen that higher values of this parameter results in better %BiasRR measure. On the other hand degree day coefficient being a snow model parameter, is not expected to affect the overall water balance but will affect the timing of the flow. This is clearly reflected in Figure 57b as this parameter shows no sensitivity to the overall water balance signature measure. %BiasFMS signature measure is related with vertical soil moisture redistribution, it can be seen from Figure 57c that saturated hydraulic conductivity of loam is highly sensitive to this measure as expected. %BiasFLV signature measure is related with long term baseflow and it is expected that baseflow time constant should be sensitive to this measure. It can be seen that time constant of slow baseflow reservoir is highly sensitive to the %BiasFLV (Fig. 57g) and high values of this parameter is more favorable. %BiasFHV signature measure is related with vertical soil distribution also, and it is expected to be sensitive to the interflow time constant. As expected, Figure 57e shows that the time constant of interflow is highly sensitive to the %BiasFHV signature measure. Finally defree day coefficient as stated earlier should be sensitive to the time related signature measure of CORR (Fig. 57i).

Due to space availability not all the scatter plots are shown here since there is 36 parameter and 6 signature measure. Sensitivity analysis for every parameter can be seen from Table 16. The numbers in this table is obtained by

- first by fitting a line to the median, function of that signature measure is calculated
- Second, by subtracting this function value at maximum and minimum parameter values sensitivity of that specific parameter for signature measure is obtained
- Finally, all these sensitivity values are normalized by standard deviation values so that comparison of different parameters can be done.

Table 16 is conditional color formatted table, where parameter is most sensitive to the signature measure is colored red and where not sensitive colored green.

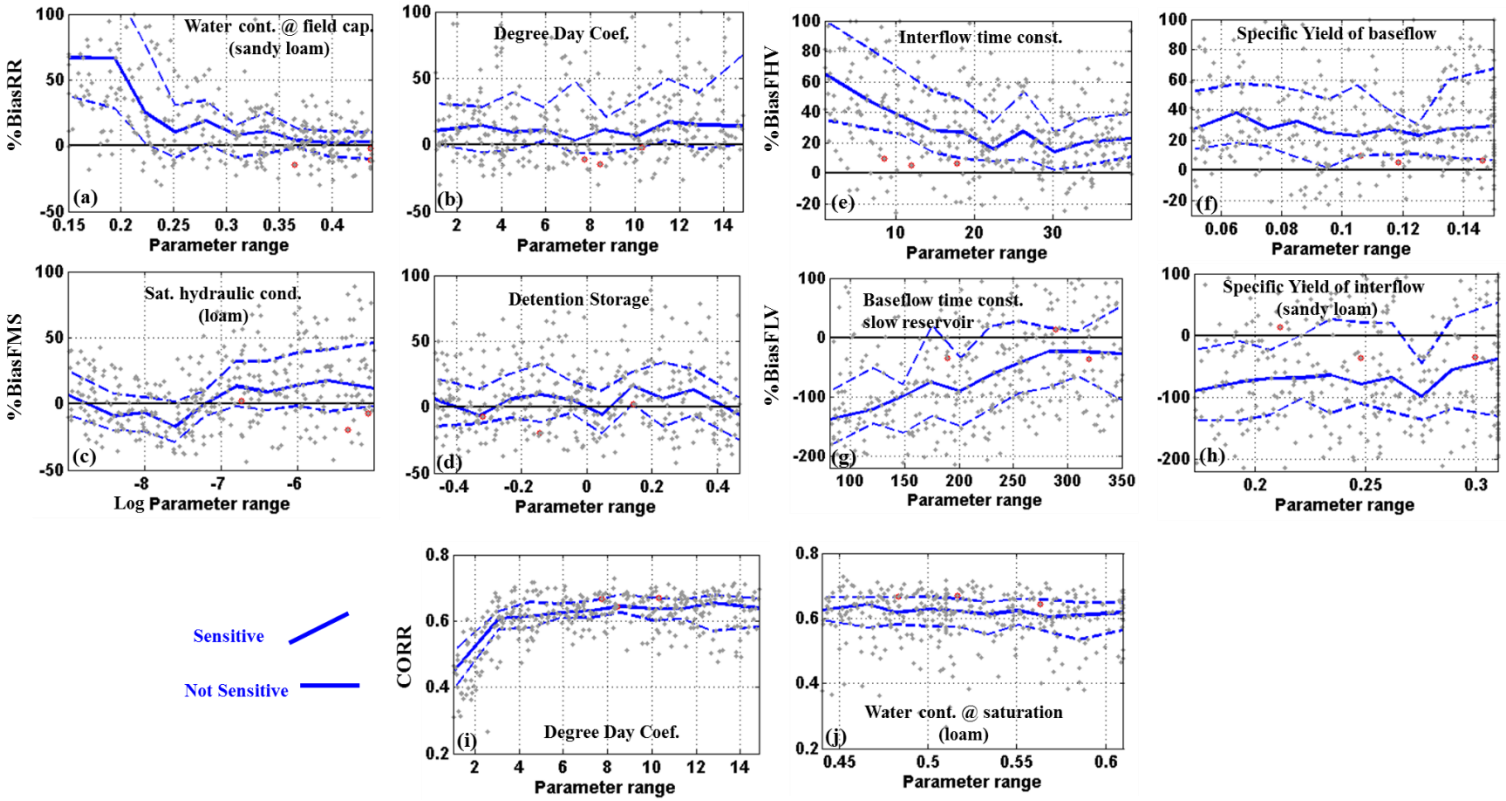

Figure 57 Sensitivity analysis using 360 randomly sampled model parameter sets. Parameters that are sensitive (a, c, e, g, and i) and not sensitive (b, d, f, h, and j) to signature measures %BiasRR, %BiasFMS, %BiasFLV and CORR.

Table 16 Summary of the sensitivity analysis result for initial 360 random parameter sets.

	Volume	Partition	High Flow	Low Flow	Timing	Sensitive	
	PBIAS	FMS	FHV	FLV	CORR		
Ddc	0.19	1.42	0.39	0.81	4.68	snow	
Mo	0.16	0.73	0.37	0.47	0.89	Over land	
DS	0.02	0.11	2.04	0.76	1.22		
Mc	0.02	0.49	0.35	0.49	0.05	Channel	
ETsd	0.13	0.02	0.66	0.33	0.65	Unsaturated Flow	
WtSL	0.59	0.49	0.39	0.53	0.77		
WtSSL	0.24	0.57	0.11	0.45	0.18		
WtFL	3.63	1.73	2.08	2.46	0.66		
WtFSL	3.19	1.69	2.12	2.01	0.49		
WtWL	1.64	0.99	1.17	1.87	0.72		
WtWSL	1.55	0.74	1.02	1.62	0.69		
Shc_L	0.76	1.76	0.12	0.70	1.93		
Shc_SL	1.75	2.81	0.68	0.24	0.07		
Gwd	0.45	0.01	0.39	0.04	0.20	Saturated Flow	gw
SYintL	0.08	0.51	0.04	0.03	0.39		Interflow
SYintSL	0.11	0.98	0.64	0.44	0.75		
DiniInL	0.18	0.52	0.64	0.45	0.62		
DiniInSL	0.18	0.52	0.64	0.45	0.62		
DbotInL	0.10	0.29	0.77	0.12	0.12		
DbotInSL	0.10	0.29	0.77	0.12	0.12		
TinL	1.13	0.27	2.80	0.05	0.54		
TinSL	0.22	0.65	2.63	0.73	0.33		
TpercL	0.56	0.33	1.06	0.28	0.14		
TpercSL	0.24	0.19	0.59	0.31	0.89		
FracMA	0.12	1.48	0.85	1.02	0.77		Baseflow
FracPA	0.12	1.48	0.85	1.02	0.77		
SYbaseMA	0.01	0.79	0.24	1.45	0.10		
SYbasePA	0.28	0.43	0.29	1.48	0.22		
Tbase1MA	0.40	0.03	0.92	0.28	0.23		
Tbase1PA	0.40	0.03	0.92	0.28	0.23		
Tbase2MA	0.20	1.66	0.24	2.00	0.43		
Tbase2PA	0.20	1.66	0.24	2.00	0.43		
DiniBtMA	0.25	0.17	0.51	0.10	0.03		
DiniBtPA	0.25	0.17	0.51	0.10	0.03		
DbotBtMA	0.27	0.05	0.49	0.33	0.04		
DbotBtPA	0.27	0.05	0.49	0.33	0.04		

After this initial sensitivity analysis, a step-wise model parameter constraining approach was utilized that starts from the slow hydrologic processes and continue towards faster hydrologic processes. First goal in the parameter constraining was to improve %BiasFLV which is sensitive by baseflow parameters. Hence model parameters controlling the baseflow were constrained to ranges that provide favorable %BiasFLV values. For example, baseflow time constant for slow reservoir (Fig. 57g) was constrained to the range [250 350] days that provide favorable %BiasFLV values (close to zero). Table 17 lists the constrained upper and lower boundaries of the baseflow parameters. Using these constrained parameter ranges for parameters controlling baseflow and initial ranges for the rest of the parameters another 150 random parameter sets was generated.

Table 17 Baseflow parameter range after constrain

Parameters		**Initial Value**	**Lower Bound**	**Upper Bound**
Fraction of percolation (poor aquifer)	Frac	0.5	0	0.5
Specific Yield of baseflow 1&2 (medium aquifer)	Sybase	0.25	0.3	0.4
Specific Yield of baseflow 1&2 (poor aquifer)	Sybase	0.1	0.12	0.15
Time constant for baseflow 1 (medium aquifer)	Tbase1	20 (day)	50	80
Time constant for baseflow 1 (poor aquifer)	Tbase1	20 (day)	50	80
Time constant for baseflow 2 (medium aquifer)	Tbase2	85 (day)	250	350
Time constant for baseflow 2 (poor aquifer)	Tbase2	85 (day)	250	350
Subtract constant to calculate Initial Depth for baseflow 1&2 (medium aquifer)	DiniBt	1(subtraction)	0	5
Subtract constant to calculate Initial Depth for baseflow 1&2 (poor aquifer)	DiniBt	1	0	5
Bottom & Threshold Depth for baseflow 1&2 (medium aquifer)	DbotBt	50	10	40
Bottom & Threshold Depth for baseflow 1&2 (poor aquifer)	DbotBt	50	10	40

After the first round of constraining, it can be seen from Figure 58(c, f, i) that %BiasFLV median value improved significantly. This new parameter sets sensitivity analysis can be seen from Table 18. It is clear that since we constrain the baseflow parameters, sensitivity values of other parameters are more pronounced. Next step in the constraining approach focused on the interflow parameters that are sensitive to the %BiasFMS and %BiasFHV which are representing vertical soil distribution. Percolation time constant is the

parameter that represents the time it takes for the water to seep down to the baseflow, therefore this parameter is sensitive to the %BiasFLV even though it is an interflow parameter set (Fig 58c). Constraining the interflow parameters using these signature measures resulted in a new ranges for these parameters sets (Table 19). Further by using these new constrained parameter set boundaries 150 random parameter sets were generated and model was run for each of these parameter sets.

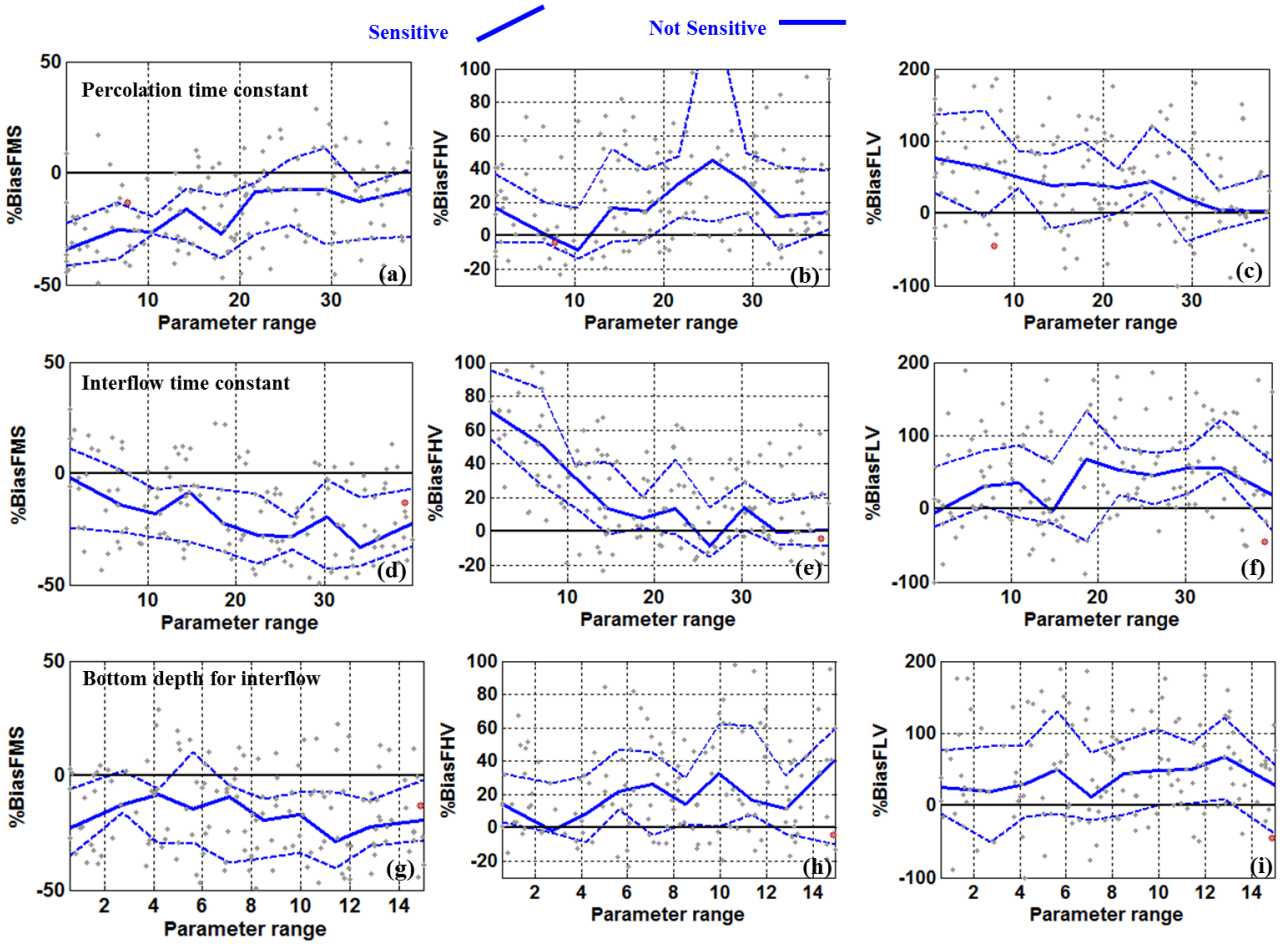

Figure 58 Sensitivity analysis of the parameters after baseflow constraining (150 model run). Interflow parameters percolation time constant (a, b, and c), and j) interflow time constant (d, e, and f) and bottom depth for interflow (g, h, and i) sensitivity for %BiasFMS, %BiasFHV and %BiasFLV.

Table 18 Sensitivity analysis after baseflow constraining (150 model run)

	Volume	Partition	High Flow	Low Flow	Timing	Sensitive	
	PBIAS	FMS	FHV	FLV	CORR		
Ddc	0.33	0.45	1.45	0.17	4.08	snow	
Mo	0.13	0.63	0.43	0.12	0.23	Over land	
DS	0.96	0.45	1.45	0.80	0.58		
Mc	0.17	0.54	0.06	0.36	1.17	Channel	
ETsd	0.28	0.43	1.05	0.63	0.14	Unsaturated Flow	
WtSL	0.14	0.81	0.33	0.43	0.20		
WtSSL	0.17	0.07	0.47	0.53	0.33		
WtFL	3.87	2.04	1.79	2.67	0.83		
WtFSL	3.22	1.43	1.53	2.24	0.01		
WtWL	1.25	0.45	0.24	0.51	0.94		
WtWSL	1.00	0.49	0.39	0.72	0.90		
Shc_L	0.12	1.02	1.07	0.56	0.88		
Shc_SL	1.50	1.82	1.13	0.11	0.13		
Gwd	0.95	0.68	1.07	1.52	0.70	Saturated Flow	gw
SYintL	0.14	1.09	0.50	1.24	0.47		Interflow
SYintSL	0.37	0.88	0.37	0.60	0.73		
DiniInL	0.63	0.20	0.61	0.35	0.67		
DiniInSL	0.63	0.20	0.61	0.35	0.67		
DbotInL	0.75	0.59	0.89	0.57	0.68		
DbotInSL	0.75	0.59	0.89	0.57	0.68		
TinL	0.60	1.78	2.64	1.18	1.80		
TinSL	0.41	1.47	2.60	0.77	0.73		
TpercL	0.82	1.79	1.13	1.16	0.43		
TpercSL	0.18	1.83	0.77	1.46	1.11		
FracMA	0.04	0.72	0.40	0.20	0.74		Baseflow
FracPA	0.04	0.72	0.40	0.20	0.74		
SYbaseMA	0.17	0.17	0.82	1.52	0.44		
SYbasePA	0.26	0.13	0.97	0.45	0.27		
Tbase1MA	0.30	0.96	0.13	0.89	0.36		
Tbase1PA	0.30	0.96	0.13	0.89	0.36		
Tbase2MA	0.11	1.45	0.17	1.41	0.41		
Tbase2PA	0.11	1.45	0.17	1.41	0.41		
DiniBtMA	0.11	0.11	0.15	0.94	1.25		
DiniBtPA	0.11	0.11	0.15	0.94	1.25		
DbotBtMA	0.18	0.11	0.40	0.19	0.22		
DbotBtPA	0.18	0.11	0.40	0.19	0.22		

Table 19 Interflow parameter range after constraining.

Parameters		Initial Value	Lower Bound	Upper Bound
Specific Yield of interflow (loam)	SYint	0.2	0.15	0.21
Specific Yield of interflow (sandy loam)	SYint	0.27	0.2	0.29
Initial Depth for interflow (loam)	Dinintl	1	0	5
Initial Depth for interflow (sandy loam)	Dinintl	1(subtraction)	0	5
Bottom & Threshold Depth for interflow (loam)	DbotIn	5 (m)	0.5	15
Bottom & Threshold Depth for interflow (sandy loam)	DbotIn	5	0.5	15
Interflow time constant (loam)	Tint	3 (day)	20	40
Interflow time constant (sandy loam)	Tint	2	20	40
Percolation time constant (loam)	Tperc	4 (day)	15	40
Percolation time constant (sandy loam)	Tperc	3	15	40

After this second step in constraining, %BiasFHV values improved significantly (see Fig. 59 b, e, and h). Further parameter constraining could be performed utilizing soil hydraulic properties, although at this point further improvement steps were not taken due to run time limitations.

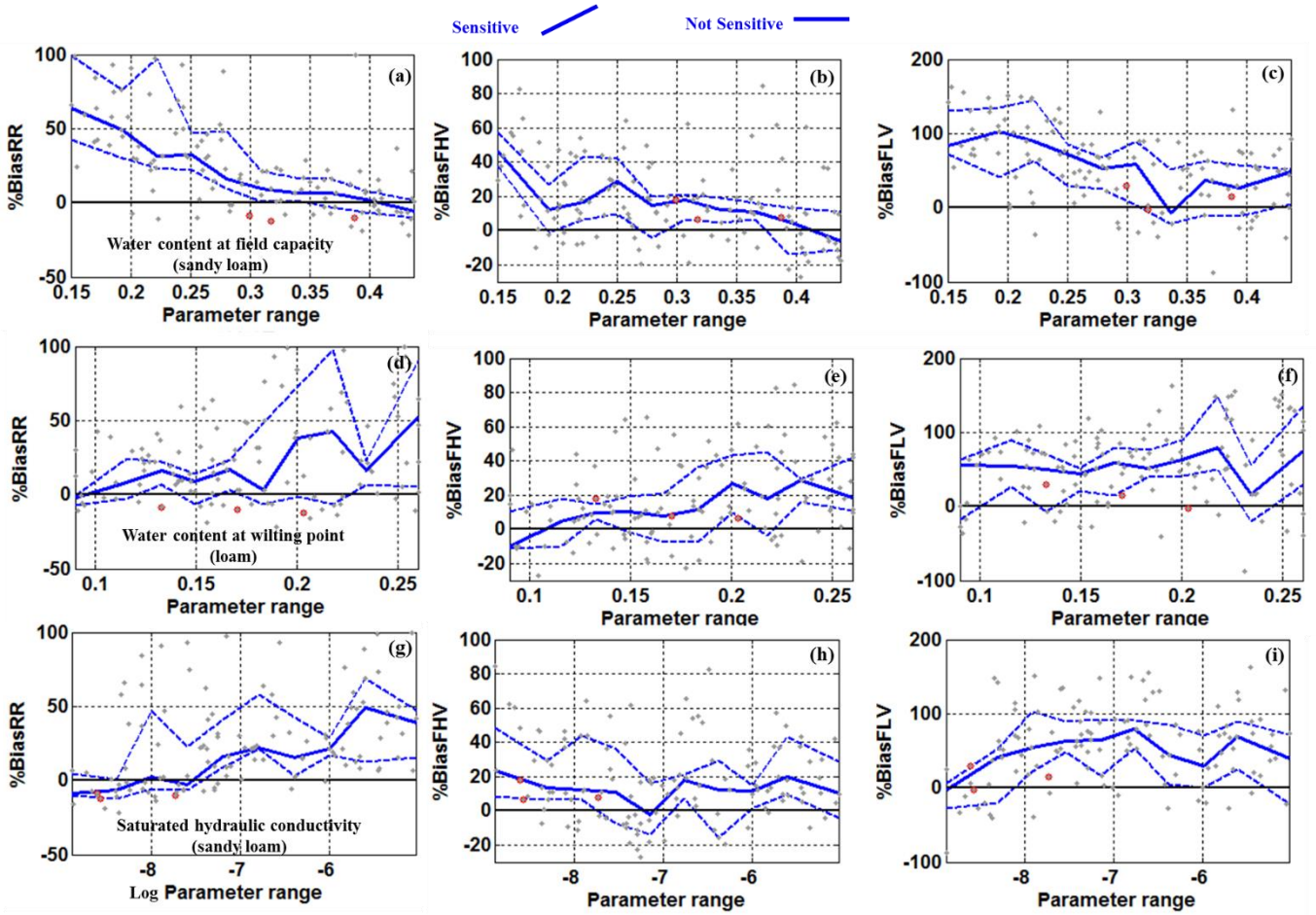

Figure 59 Sensitivity analysis of the parameters after baseflow & interflow constraining (150 & 150 model run). Soil hydraulic parameters water content at field capacity (a, b, and c), and j) water content at wilting point (d, e, and f) and saturated hydraulic conductivity (g, h, and i) sensitivity for %BiasFMS, %BiasFHV and %BiasFLV.

Final step of the constraining approach is to constrain the signature measures with the 150 random samples generated at the last step and obtain a calibrated parameter set from final model runs. To do this, %BiasRR, %BiasFMS and %BiasFHV are constrained to be within +/- 20% and %BiasFLV to be within +/- 15% as can be seen from Figure 60. The shaded gray area in this figure represents the constrained region. There was only a single feasible parameter set within this constrained region and this parameter set is given in Table 20. It is clear from the Figure 60 that there is a significant improvement from the initial parameter set considering the signature measure values.

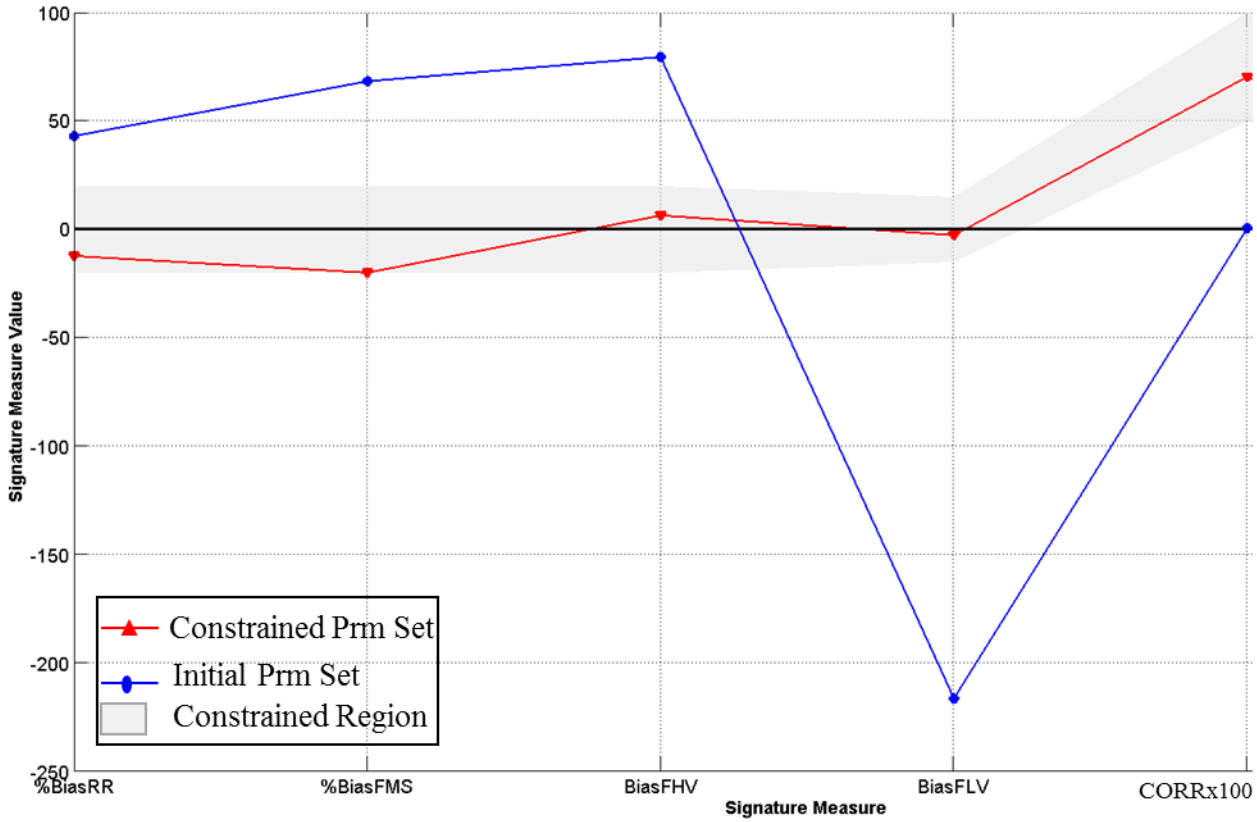

Figure 60 Signature measure values for optimum and initial parameter sets.

Table 20 Feasible parameter set in the constrained space.

Parameter	Value
Ddc	9.06
Mo	Spatially distributed
DS	Spatially distributed
ETsd	Spatially distributed
Mc	19.86
Gwd	-18.89
WtSL	0.45
WtSSL	0.44
WtFL	0.33
WtFSL	0.31
WtWL	0.203
WtWSL	0.198
Shc_L	$10^{-5.86}$
Shc_SL	$10^{-8.57}$
SYintL	0.21
SYintSL	0.29
DinintlL	4.68
DinintlSL	4.68
DbotInL	7.95
DbotInSL	7.95
TintL	26.01
TintSL	20.0
TpercL	40.0
TpercSL	35.42
FracMa	0.34
FracPa	0.34
SybaseMa	0.35
SybasePa	0.142
Tbase1Ma	77.54
Tbase1Pa	77.54
Tbase2Ma	295.872
Tbase2Pa	295.872
DiniBtMa	24.42
DiniBtPa	24.42
DbotBtMa	27.60
DbotBtPa	27.60

Simulated hydrograph for the constrained parameter set can be seen in Figure 61 for calibration period and evaluation period. Since flow data in between 2008/11/18-2009/03/31 deemed to be erroneous, this period is excluded from the analysis. It can be seen from this figure that, with this constrained parameter set, MIKE SHE-MIKE 11 is

able to simulate a number of important flow events during evaluation and calibration periods.

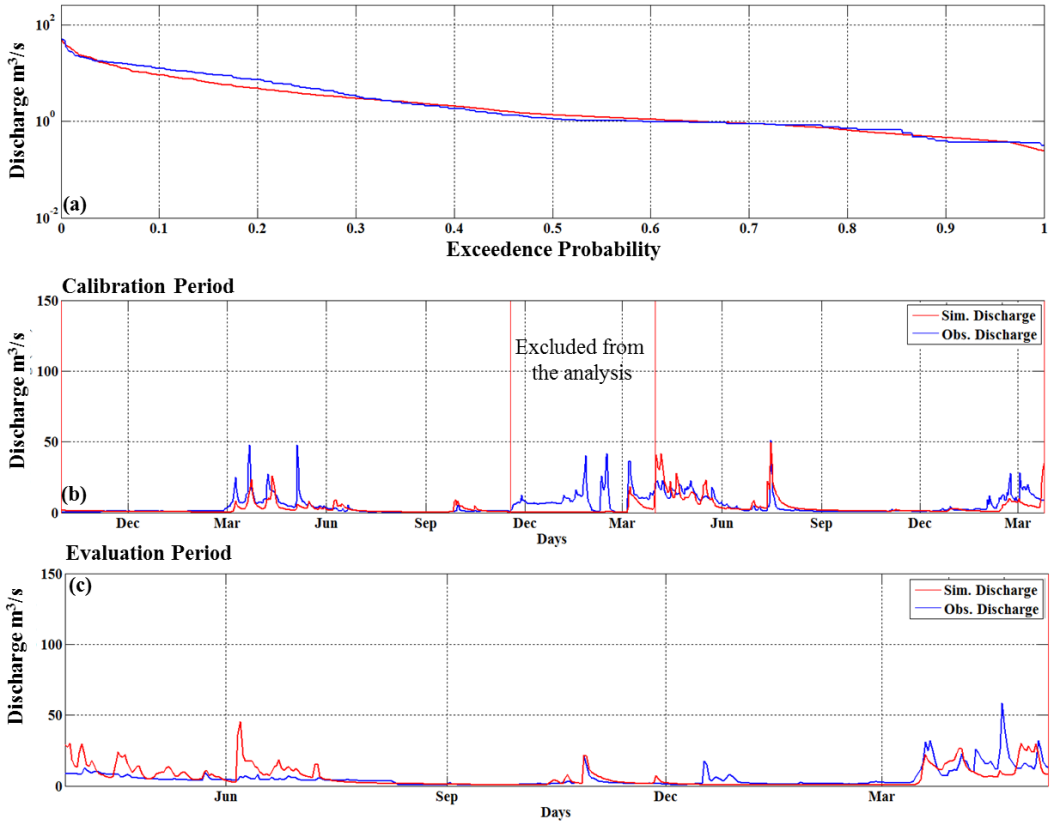

Figure 61 (a) FDC and hydrographs (b) for calibration period (c) for evaluation period using the constrained set.

5.7.2. Comparison of Model Performance Driven by SBP and Bias Adjusted SBP products

As mentioned earlier, SBP products performances can further be evaluated by hydrologic model since stream flow observations have the potential to provide an independent check on the degree of errors in the precipitation datasets that are important for hydrologic applications. Determined constrained parameter set is used to run the model by SBP products and bias adjusted SBP products using BAPS algorithm. First of all TMPA-7A SBP product is run by the constrained parameter set (Figure 62). As a result the TMPA-

7A SBP product was able to detect the timing of peak flows however significant overestimation of flows is evident (Fig. 62a) especially during the evaluation period. It should be noted that this product has its own bias adjustment procedure hence not adjusted further with BAPS algorithm, therefore it can be said that its performance is impressive, in terms of detecting the timing of flows.

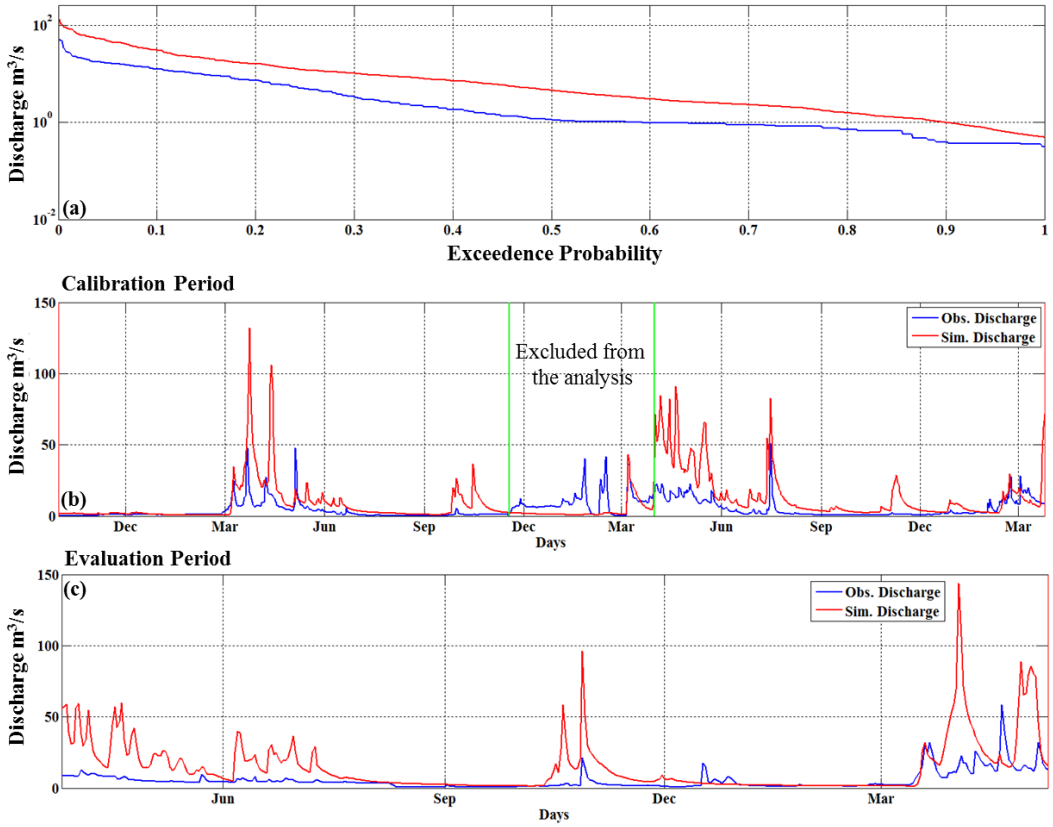

Figure 62 Simulated and observed flow FDC (a) and hydrograph (b) for calibration period (c) hydrograph for evaluation period for constrained parameter set run by TMPA-7A.

Secondly hydrologic model is driven by the TMPA-7RT product (Figure 63). Upon comparison with Figure 62, it is clear that TMPA-7A is superior to this product in terms of precipitation magnitude whereas the timing of flows is also somewhat well simulated using the TMPA-7RT product. It is evident from these results that the utility of the TMPA products in hydrologic simulation studies will improve further using bias adjustment.

While evaluating this product against the RGP, products overestimation over Region 2 was emphasized (Chapter 3). This overestimation is simulated in hydrologic model as significant overestimation in all events and this situation is evident in FDC (Fig. 63a). Performance of the product especially deteriorates during the evaluation time period, which is drier.

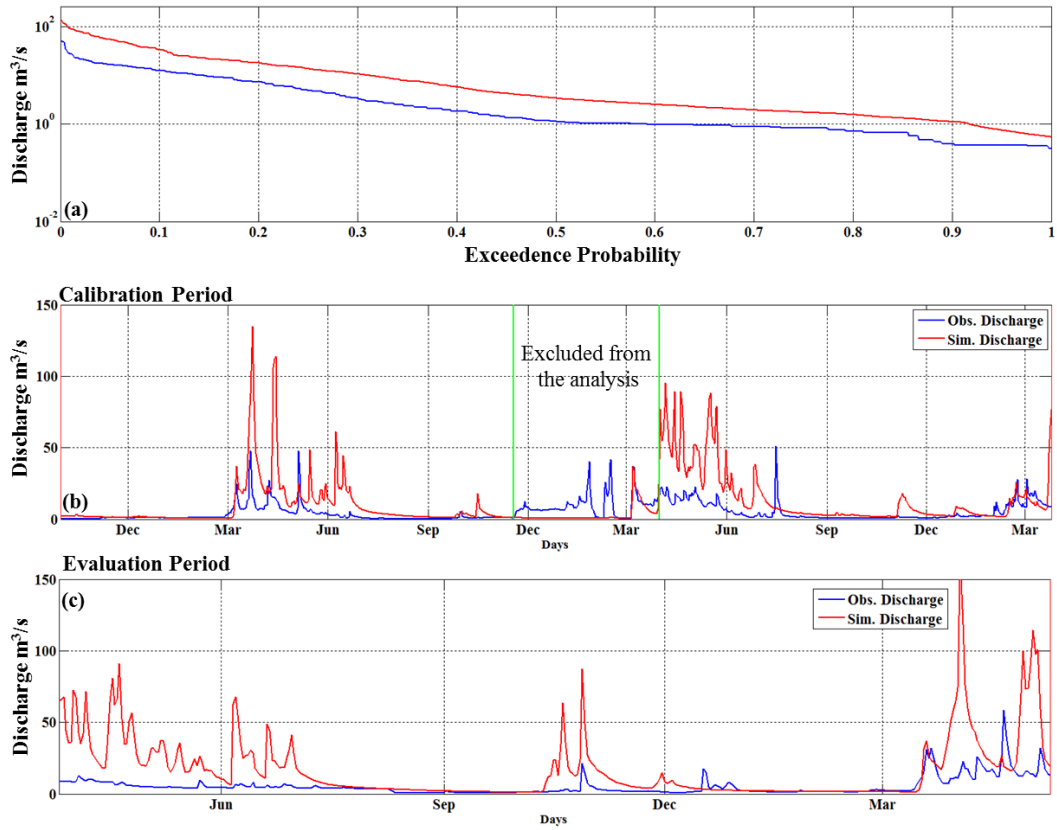

Figure 63 Simulated and observed flow FDC (a) and hydrograph (b) for calibration period (c) hydrograph for evaluation period for constrained parameter set run by TMPA-7RT.

Note that evaluation of the CMORPH by RGP the product determined significant underestimation in Region 2 (Chapter 3). This problem is more significant in the hydrologic model results driven by the CMORPH product (Figure 64). CMORPH driven model was unable to generate any flow during the calibration period, while there is only single simulated flow event in evaluation period which is not evident in the observed

flow. Simply it can be said that this product without a bias adjustment cannot be used in hydrologic modeling studies in this region.

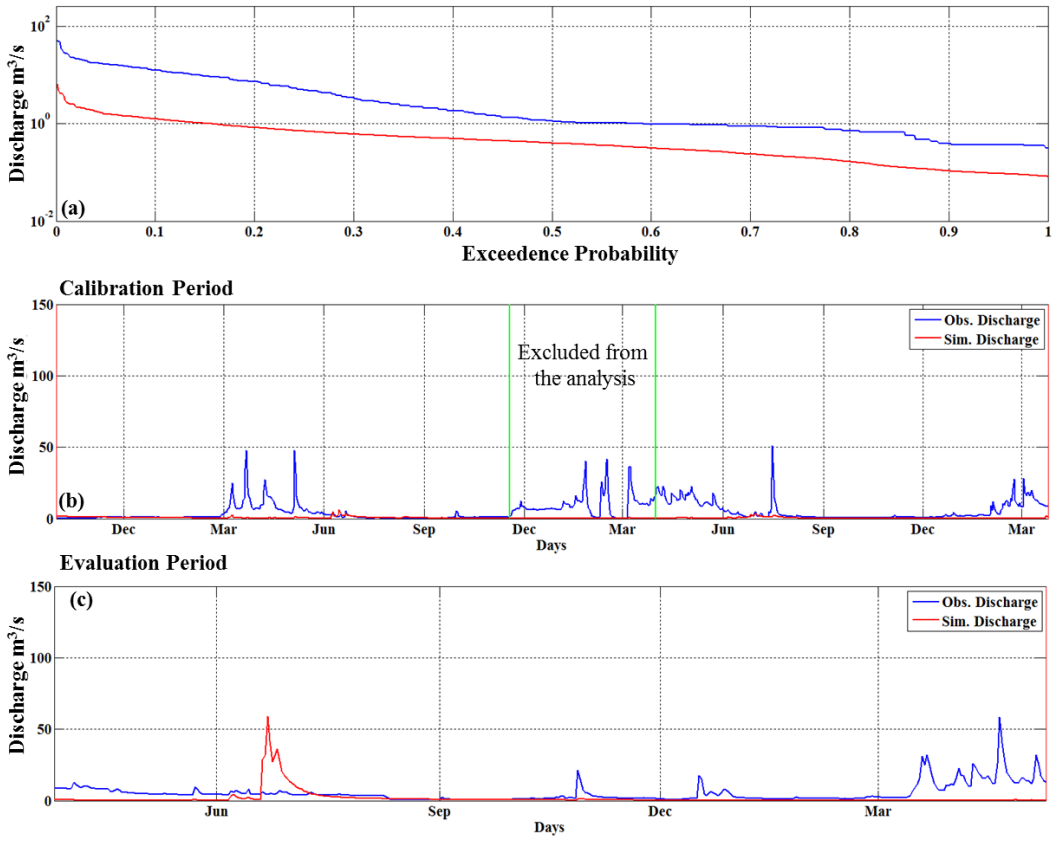

Figure 64 Simulated and observed flow FDC (a) and hydrograph (b) for calibration period (c) hydrograph for evaluation period for constrained parameter set run by CMORPH.

As mentioned earlier, bias adjustment algorithms provided better results while comparing SBP products with the RGP product (Chapter 5). The same results are also obtained when the hydrologic model is driven by the bias adjusted SBP products. Significant overestimation of stream flow by TMPA-7RT driven model is corrected to a significant extent when BAPS algorithm is used to adjust this product (Fig. 65). Analysis of this figure indicates that significant overestimation for both high flow and low flow

magnitudes are corrected accordingly (Fig. 65a). However there still exits a slight underestimation for high flow and this situation is also evident in evaluation period.

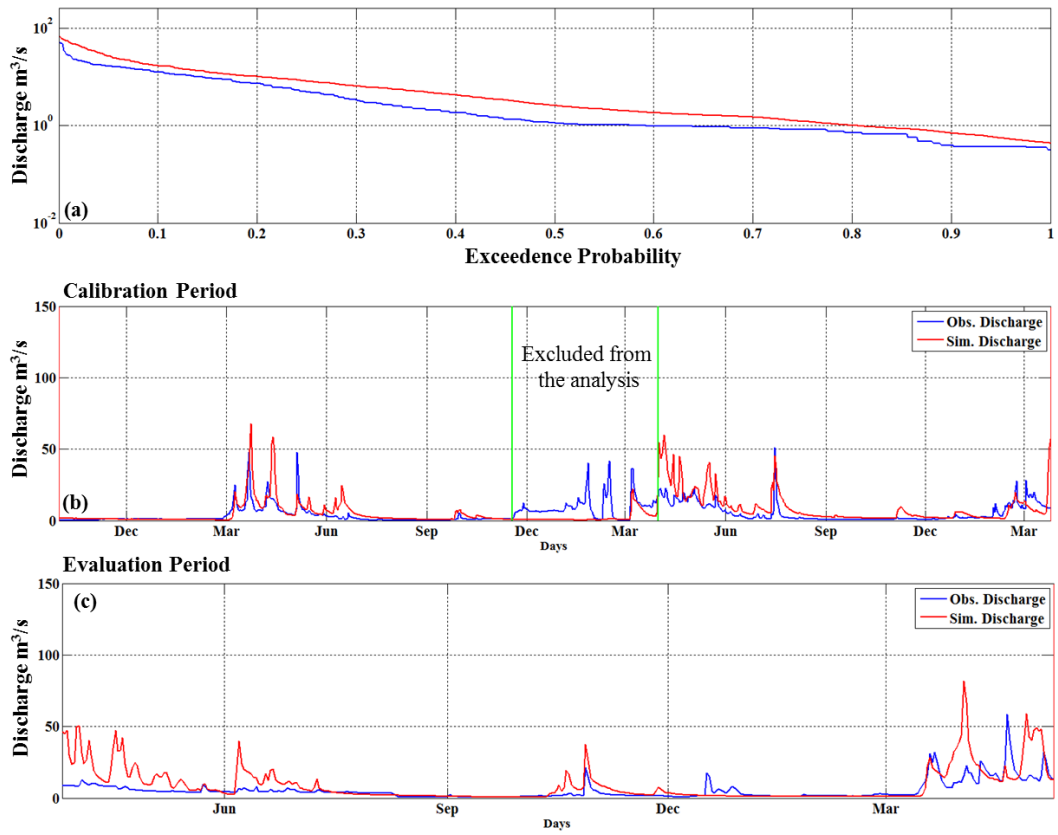

Figure 65 Simulated and observed flow FDC (a) and hydrograph (b) for calibration period (c) hydrograph for evaluation period for constrained parameter set run by TMPA7RT BAPS.

On the other hand BAPS adjusted CMORPH driven model performance for high flow is much better than the BAPS adjusted TMPA-7RT results (Fig. 66). This might be due to the fact that TMPA-7RT was significantly overestimating precipitation over Region 2 with spatially heterogeneous estimates while CMORPH showed significant but uniform underestimation when compared to RGP dataset. However there seems to be a mismatch in the simulated low flows when BAPS corrected CMORPH is used to derive the model. It can be seen that the BAPS adjusted CMOPRH driven model slightly overestimates low flows.

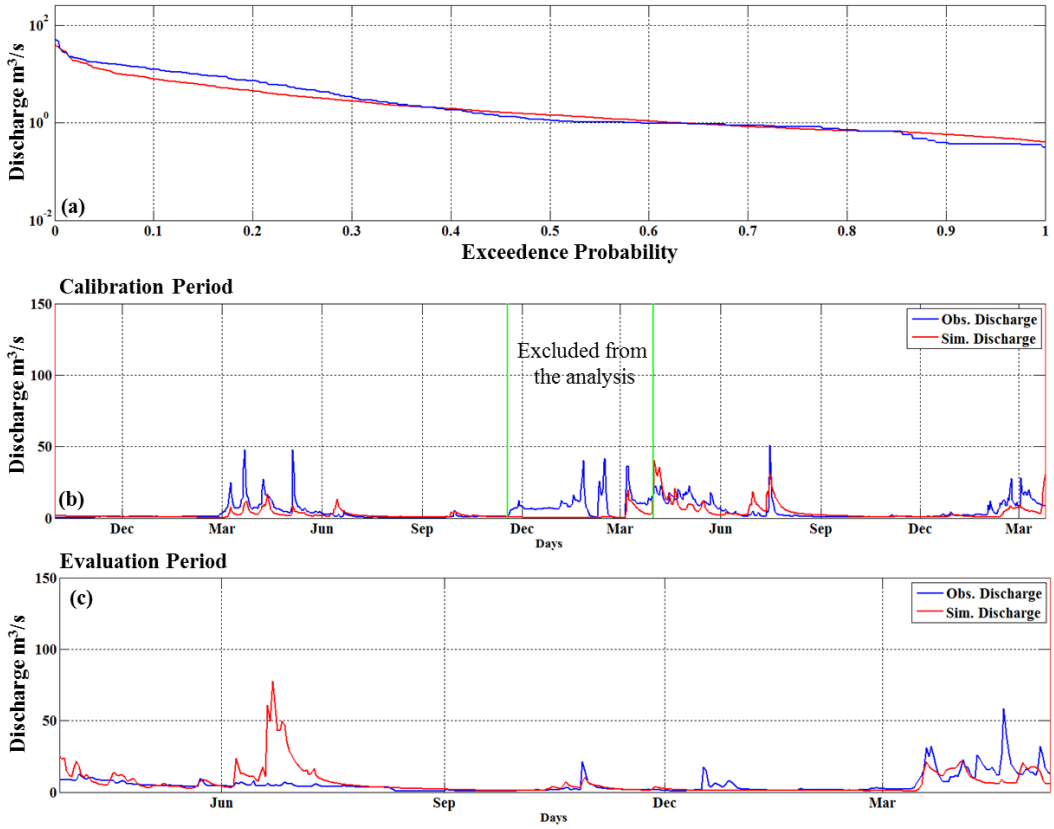

Figure 66 Simulated and observed flow FDC (a) and hydrograph (b) for calibration period (c) hydrograph for evaluation period for optimum parameter set run by CMORPH BAPS.

Table 21 shows the summary statistics during calibration and evaluation periods.

Table 21 Signature measure results for optimum parameter set calibration and evaluation period

		%BiasRR	%BiasFMS	%BiasFHV	%BiasFLV	CORR
RGP	calibration period	-12.25	-19.96	6.44	-2.65	0.70
	evaluation period	-19.08	17.41	-17.81	-42.86	0.67
TMPA-v7	calibration period	169.70	-7.61	193.21	91.74	0.68
	evaluation period	131.86	17.03	178.93	223.02	0.55
TMPA-RT	calibration period	183.93	6.51	228.52	99.96	0.64
	evaluation period	151.28	24.47	220.00	194.09	0.54
CMORPH	calibration period	-86.18	-40.48	-89.26	-180.18	-0.05
	evaluation period	-91.36	-39.27	-96.00	-431.02	-0.29
TMPA BAPS	calibration period	62.94	-8.45	79.21	52.44	0.72
	evaluation period	39.96	25.40	63.95	59.54	0.62
CMORPH BAPS	calibration period	-21.23	-19.25	-10.30	26.09	0.63
	evaluation period	-26.31	-9.45	-40.40	90.58	0.68

CHAPTER 6

CONCLUSIONS & RECOMMENDATIONS

6.1. Satellite-based Precipitation Products

- All evaluated SBP products underestimated precipitation along the coast (windward region) at various levels compared to rain gauge dataset. Underestimation of RGP precipitation by SBP products on the windward side is generally characteristic for both warm and cold seasons, however more pronounced for the cold season. Underestimation by SBP products on the windward side is possibly due to warm orographic precipitation that cannot be detected by any passive (MW or IR) sensor. TMPA-7RT and CMORPH products suffered from precipitation detection problem over water-land mixed cells along the shore and TMPA-7A algorithm was able to correct for this problem.

- Along the drier (leeward) side of the orography, SBP products were generally characterized by overestimation of precipitation. CMORPH, being the only exception, provided slight underestimation compared to rain gauge dataset while producing the best performance at the annual scale on the leeward side of the orography. Overestimation by TMPA and MPE products on the leeward (drier) side could be attributed to a number of limitations by MW and IR sensors. Overestimation by MW sensors is likely due to surface snow/ice contamination in cold season. Overestimation by IR sensors is possibly due to overestimation of both area and magnitude of summer convective precipitation, which usually occupies only a small fraction of cold cloud area detected by the sensor. Further,

IR-based techniques may overestimate due to misidentification of some cold clouds, such as cirrus, that may not generate any rainfall.

- Investigation of the spatial distribution of the precipitation estimates over the study area showed that evaluated SBP products failed to represent the sharp precipitation gradient normal to the orography (rain-shadow affect) revealed by the RGP dataset.

- The uniform nature of underestimation by CMORPH product can be attributed to the significant underestimation by the MW dataset used in the algorithm and spatially heterogeneous nature of TMPA-7RT product can be explained by the differences in precipitation rates produced by IR and MW datasets used in this algorithm.

- RGP dataset showed a distinct difference in heavy precipitation frequency in windward region (more frequent) compared to leeward region, which is more significant in cold season. However the tested SBP products failed to discriminate this behavior while most significantly underestimating heavy precipitation frequency in cold season over windward region.

6.2. Bias Adjustment

- Proposed bias adjustment algorithm is based on physiographic similarity of the rain gauges over topographically complex topography characterized by orographic precipitation is better suited to complex regions and generally provided better results compared to the benchmark 'Inverse Distance Weighted' method.

- In Region 1 significant underestimation is improved by both algorithms. Further, BAPS algorithm consistently provided better performance compared to IDW method in cold season. However in warm season IDW method provide slightly improved statistics. Precipitation detection is significantly improved for light

precipitation for both bias adjustment algorithms to some extent in Region 1 and slight overestimation in cold season.

- In Region 2 IDW product overestimated the precipitation even worse than the SBP products while BAPS algorithm provided slight underestimation. For cold season IDW was not able to correct %BIAS. Precipitation detection performance of BAPS is better compared to IDW for Region 2.

- In overall BAPS performance is better especially in cold season. Bias adjustment procedure seems to perform better during cold season and in Region 1, due respectively to less convective precipitation occurrence and higher density of rain gauges. For all SBP products, the BAPS algorithm performance in Region 1 is much better than the Region 2.

- BAPS algorithm was not able to improve CORR statistics which shows similarity with the study of Boushaki et al. (2009) who reported that their algorithm was successful in improving RMSE and BIAS statistics however their CORR statistic did not show significant improvement as did the other statistics they have used and might be due to heterogeneity of the precipitation estimation of SBP products.

- Investigation of the spatial distribution of the precipitation estimates over the study area showed that bias adjustment using BAPS algorithm is successfully represent the sharp precipitation gradient normal to the orography (rain-shadow affect) while IDW algorithm was able to represent this behavior to some extent, with underestimation of heavy precipitation in Region 1 and overestimation in Region 2.

- Seasonal dependency of the SBP products before the bias adjustment is improved significantly after the correction.

- Related significant improvements in POD and FAR, it can be concluded that proposed BAPS correction algorithm can introduce rain in areas where the SBP does not detect rainfall and algorithm can assign no rainfall where SBP falsely detects rainfall.

- SBP estimations are directly related with the topographically complex terrain especially estimation of orographic precipitation and bias adjustment for these regions is not effective if weights of bias adjustment calculated based on proximity. Bias adjustment weights calculated with physiographic similarity concept works more effectively for complex terrain.

6.3. Hydrologic Modeling

- Sensitivity analysis is conducted by randomly generated parameter sets. Initially 360 random parameter sets were generated and for every parameter set model was run and signature measures were calculated from the simulated and observed streamflow values. As a result of the sensitivity analysis, it was found that the parameters controlling baseflow are sensitive to the low flow measure, %BiasFLV, those controlling interflow are sensitive to high flows, %BiasFHV, the degree day coefficient parameter is sensitive to the timing, CORR, and the soil hydraulic parameters to %BiasRR due to ET control. These sensitivities are also conceptually realistic.

- After sensitivity analysis, a step-wise model parameter constraining approach was utilized that starts from the slow hydrologic processes and continue towards faster hydrologic processes. First goal was to improve %BiasFLV which is sensitive to parameters controlling baseflow. Hence model parameters controlling the baseflow were constrained to ranges that provide favorable %BiasFLV values and further 150 random parameter set were generated in this constrained space. After this constraint %BiasFLV significantly improved. Next %BiasFHV which are representing vertical soil distribution are constrained to improve %BiasFHV. Constraining the interflow parameters using these signature measures resulted in new ranges for these parameter sets (150 random parameter set generated). After this step it is observed that %BiasFHV values improved significantly also. Finally signature measure values of randomly sampled parameter sets at the last step were further constrained and a final calibrated parameter set was obtained that satisfied

all constrains. Result of this feasible parameter set showed that MIKE SHE-MIKE11 is able to simulate a number of important flow events during evaluation and calibration period.

- There was only one feasible parameter set within constrained region and this parameter set is further used to drive hydrologic model by SBP and bias adjusted SBP products. TMPA-v7 outperforms TMPA-7RT and CMORPH in terms of flow simulation performance. Product was able to capture the timing of the significant events well, however with overestimation in the flow magnitude. If satellite only SBP products are compared with each other, it can be concluded that CMORPH is not able to generate any flow in both calibration and evaluation period, which is a serious drawback for this product in terms of hydrologic modeling studies in the study area.

- Performance of proposed bias adjustment algorithm BAPS proves that it is able to correct significantly missed precipitations and falsely detected precipitations. Significant overestimation by TMPA-7RT and underestimation by CMORPH is corrected accordingly. Overestimation by TMPA-7RT for both high and low flow magnitudes were also corrected accordingly. However there still exists a slight underestimation for high flows. While CMORPH driven model performance for high flows is much better than the BAPS adjusted TMPA-7RT results. This might be due to the fact that TMPA-7RT was significantly overestimating precipitation over Region 2 with spatially heterogeneous estimates while CMORPH showed significant but uniform underestimation when compared to RGP dataset.

6.4. Future Work and Recommendations

Evaluation studies performed in different hydroclimatic regions in Turkey and elsewhere will further shed light on the utility of these products for use in hydrologic studies in ungauged and/or poorly gauged regions with complex topography around the globe.

In a future study, the proposed bias adjustment algorithm could be compared with atechnique that also incorporates elevation in the interpolation of error (such as kriging). Further multiplication error model (Tian et al., 2013) can be compared to see if there is improvement in the error correction relative to the additive error model.

The diagnostic evaluation methodology utilized in this study could be compared with a classical single objective calibration methodology to investigate the improvements (or lack of) in the model performance. For example dynamically dimensioned search algorithm (DDS) proposed by Tolson and Shoemaker (2007) is well suited to distributed hydrological models with extensive run times.

MIKE SHE-MIKE 11 hydrologic model is calibrated by using RGP products and this calibrated parameter set is used with SBP product runs. In a future study the model could be calibrated by individual SBP products and the performances of these calibrated model parameters could be compared.

Hydrogeological component of the model could be improved, if further data such as well logs, groundwater elevations etc. become available.

REFERENCES

Abbott, M.B., J. C. Bathurst, J. A. Cunge, P. E. O'Connell, and J. Rasmussen: 1986. An introduction to the European Hydrological System-Systeme Hydrologique Europeen, "SHE", 1. History and philosophy of a physically-based, distributed modeling system. J. Hydrol. 87, 45-59

Adam, J. C., E. A. Clark, D. P. Lettenmaier, and E. F. Wood, 2006: Correction of global precipitation products for orographic effects. Journal of Climate. 19, 15-38.

AghaKouchak, A., A. Mehran, H. Norouzi, and A. Behrangi, 2012: Systematic and random error components in satellite precipitation data sets. Geophysical Research Letter. 39, L09406.

Aonashi, K., J. Awaka, M. Hirose, T. Kozu, T. Kubota, G.Liu, S. Shige, S. Kida, S. Seto, N. Takahashi, and Y. N. Takayabu, 2009: GSMaP passive microwave precipitation retrieval algorithm: Algorithm description and validation. J. Meteor. Soc. Japan, 87A, 119–136.

Arkin, P. A., 1979. The relationship between fractional coverage of high cloud and rainfall accumulations during GATE over the B-scale array. Monthly Weather Review. 106, 1153-1171.

Arkin, P. A., and B. N. Meisner, 1987: The relationship between large-scale convective rainfall and cold over the western hemisphere during 1982-1984. Monthly Weather Review. 115, 51-74.

Arnold, J.G., P.M. Allen, R. Muttiah, and G. Bernhardt. 1995: Automated base flow separation and recession analysis techniques. Ground Water 33(6): 1010-1018.

Basistha, A., D. S. Arya, and N. K. Goel, 2007: Spatial distribution of rainfall in Indian Himalayas – A case study of Uttarakhand Region. Water Resour Manage. Doi 10.1007/s11269-007-9228-2.

Bellon, A., S. Lovejoy, and G. L. Austin, 1980: Combining satellite and radar data for the short-range forecasting of precipitation. Monthly Weather Review. 108, 1554-1556.

Boushaki, F. I., Hsu, K.-L., Sorooshian, S., Park, G.-H., Mahani, S., & Shi, W. (2009). Bias Adjustment of Satellite Precipitation Estimation Using Ground-Based Measurement: A Case Study Evaluation over the Southwestern United States. Journal of Hydrometeorology, 10(5), 1231–1242.

Caruso, C., and F. Quarta, 1998: Interpolation methods comparison. Comput. Math. Appl. 35(12), 109-126.

Cheema, M. J. M., and W., G., M., Bastiaanssen, 2012. Local calibration of remotely sensed rainfall from the TRMM satellite for different periods and spatial scales in the Indus basin. International Journal of Remote Sensing, 33(8), 2603–2627. doi:10.1080/01431161.2011.617397

Chow, V.T., Handbook of Applied Hydrology, 7-25, McGraw-Hill, Book Company, New York, 1964.

Creutin, J. D., and C. Obled, 1982: Objective analysis and mapping techniques for rainfall fields: and objective comparison. Water Resources Research. 18(2), 251-256.

Daly, C., W. P. Gibson, G. H. Taylor, G. L. Johnson, and P. Pasteris, 2002: A knowledge-based approach to the statistical mapping of climate. Climate Res., 22, 99–113.

Daly, C., 2006: Guidelines for assessing the suitability of spatial climate data sets. Int. J. Climatol, 26, 707–721.

Daly, C., M. Halbleib, J. I. Smith, W. P. Gibson, M. K. Doggett, G. H. Taylor, J. Curtis, and P. P. Pasteris, 2008: Physiographically sensitive mapping of climatological temperature and precipitation across the conterminous united states. Int. J. Climatol., 28, 2031-2064.

DHI, 2012: MIKE SHE- MIKE 11 user manual.

Dinku, T., P. Ceccato, E. Grover-Kopec, M. Lemma, S. J. Connor, and C. F. Ropelewski, 2007: Validation of satellite rainfall products over East Africa's complex topography. Int. J. Remote Sens., 28, 1503–1526.

Dinku, T., S. Chidzambwa, P. Ceccato, S. J. Connor, and C. F. Ropelewski, 2008: Validation of high-resolution satellite rainfall products over complex terrain. Int. J. Remote Sens., 29, 4097-4110.

Dinku, T., S. J. Connor, and P. Ceccato, 2010: Comparison of CMORPH and TRMM-3B42 over Mountainous Regions of Africa and South America. Satellite Rainfall Applications for Surface Hydrology, M. Gebremichael, and F. Hossain, Eds., Springer, 193–204.

Diodata, N., and M. Ceccarelli, 2005: Interpolation processes using multivariate geostatistics for mapping of climatological precipitation mean in Sannio Mountains (southern Italy). Earth Surf. Process. Landforms. 30, 259-268.

Downer, C. W., F. L. Ogden, W. D. Martin, and R. S. Harmon, 2002: Theory, Development, and Applicability of the Surface Water Hydrologic Model CASC2D. Hydrological Processes, 16, pp 255-275.

Duan, Q., S. Sorooshian, and V. Gupta, 1992: Effective and efficient global optimization for conceptual rainfall-runoff models. Water Resour. Res., 28, 1015-1031.

DSİ, 1968: Hydrogeological Investigation Report for Kastamonu, Araç Plain. General Directorate of State Hydraulics Works, Ankara.

Earth Tech., and DHI. (2007). Kissimmee Basin Modeling and Operations Study KBMOS, AFET Model Documentation/Calibration Report, West Palm Beach, FL.

Ebert, E. E., J. E. Janowiak, and C. Kidd, 2007: Comparison of Near-Real-Time Precipitation Estimates from Satellite Observations and Numerical Models. Bull. Amer. Meteor. Soc., 88, 47–64.

Freeze, R. A., and R. L. Harlan, 1969: Blueprint for a physically-based digitally-simulated hydrologic response model. Journal of Hydrology, 9, 237-258.

Gebregiorgis, A. S., and F. Hossain, 2013: Understanding the Dependence of Satellite Rainfall Uncertainty on Topography and Climate for Hydrologic Model Simulation. IEEE Trans. Geosci. Remote Sens., 51, 704–718.

Graham D. N., and M. B. Butts, 2005: Flexible integrated watershed modeling with MIKE SHE. In watershed models, eds. V. P. Singh & D. K. Frevert. CRC Press. 245-272

Grayson, R. and G. Blöschl 2000: Spatial Patterns in Catchment Hydrology: Observations and Modelling. Cambridge University Press, 200, pp763.

Groisman, P. Y., and D. R. Legates, 1994: The accuracy of United States precipitation data. Bull. Amer. Meteor. Soc., 75, 215–227.

Gul, G. O., D. Rosbjerg, A. Gul, M. Ondracek, and K. Dikgola, 2010: Assessing climate change impact on river flows and environmental flow requirements at catchment scale. Ecohydrology, 3, 28-40.

Gupta, H. V., S. Sorooshian, and P. O. Yapo, 1998: Toward improved calibration of hydrological models: Multiple and non-commensurable measures of information. Water Resources Research, 34(4), 751-763.

Gupta, H. V., T. Weagner, and Y. Liu, 2008: Reconciling theory with observations: Elements of a diagnostic approach to model evaluation. Hydrol. Process., doi:10.1002/hyp.6989.

Göncüoğlu M. C., 2010: Introduction to Geology of Turkey: Geodynamic evolution of the Pre-Alpine and Alpine Terrains. MTA Monograph Series, 66. ISBN 978-605-4075-74.

Goovaerts P., 1999: Using elevation to aid the geostatistical mapping of rainfall erosivity. Catena. 34(3-4), 227-242.

Goovaerts P., 2000: Geostatistical approaches for incorporating elevation into the spatial interpolation of rainfall. Journal of Hydrology, 228(1-2), 113-129.

Haan, C.T., Hydrological Modelling of Small Watersheds, 211, Published by American Society of Agricultural Engineers, USA, 1982.

Havnø, K., M.N. Madsen, and J. Dørge, 1995: MIKE 11 - A generalized river modelling package, in Computer Models of Watershed Hydrology, Singh, V.P., Ed., Water Resources Publications, Colorado, USA, p809-846.

Hayakawa, K, K. Uchijima, and M. Fujita, 1995: A Study on Subcatchment Scale for a Distributed Runoff Model. Environment Internation, Vol. 21, No. 3., pp. 491-496.

Heinemann, T. 2003: The EUMETSAT Multi Sensor Precipitation Estimate (MPE): Concept and validation. [Available online at http://www.eumetsat.int/groups/ops/documents/document/mpe_conceptvalidation_uc2003.pdf].

Hirpa, F., M. Gebremichael, and T. Hopson, 2010: Evaluation of High-Resolution Satellite Precipitation Products over Very Complex Terrain in Ethiopia. J. Appl. Meteor. Climatol., 49, 1044–1051.

Hengl, T., G. B. M. Geuvelink, and A. Stein, 2003: Comparison of kriging with external drift and regression kriging. Enschede, The Netherlands: ITC.

Hong, Y., D. Gochis, J. Cheng, K. Hsu, and S. Sorooshian, 2007: Evaluation of PERSIANN-CCS Rainfall Measurement Using the NAME Event Rain Gauge Network. J. Hydrometeor., 8, 469–482.

Hossain, F., and E. N. Anagnostou, 2006: A two dimensional satellite rainfall error model. IEEE Trans. Geosci. Remote Sens., 44, 1511–1522.

Hossain, F. and G. J. Huffman, 2008: Investigating error metrics for satellite rainfall data at hydrologically relevant scales. Journal of Hydrometeorology, 9, 563-575.

Huffman, G. J., R. F. Adler, D. T. Bolvin, G. Gu, E. J. Nelkin, K. P. Bowman, Y. Hong, and E. F. Stocker, 2007: The TRMM Multi-satellite Precipitation Analysis (TMPA): Quasi-global, multiyear, combined-sensor precipitation estimates at fine scales. J. Hydrometeor., 8, 38-55.

Huffman, G. J., R. F. Adler, D. T. Bolvin, and E. J. Nelkin, 2010: The TRMM Multi-satellite Precipitation Analysis (TMPA). Satellite Rainfall Applications for Surface Hydrology, M. Gebremichael, and F. Hossain, Eds., Springer, 3–22.

Huffman, G. J., 2013: README for Accessing Experimental Real-Time TRMM Multi-Satellite Precipitation Analysis (TMPA-RT) Data Sets [Available online at ftp://meso-a.gsfc.nasa.gov/pub/trmmdocs/rt/3B4XRT_README.pdf].

Hutchinson, P., 1968: An analysis of the effect of topography on rainfall in the Taieri Catchment area, Otago. Earth Sci. J., 2, 51-68.

Hutchinson, M.F., J.A. Stein, J.L. Stein, and T. Xu, 2009: Locally adaptive gridding of noisy high resolution topographic data. In Anderssen, R.S., R.D. Braddock and L.T.H. Newham (eds) 18th World IMACS Congress. Modelling and Simulation Society of Australia and New Zealand and International Association for Mathematics and Computers in Simulation, July 2009, pp. 2493–2499.

Hutchinson, M.F., T. Xu, and J.A. Stein, 2011: Recent Progress in the ANUDEM Elevation Gridding Procedure. In: Geomorphometry 2011, edited by T. Hengel, I.S. Evans, J.P. Wilson and M. Gould, pp. 19–22. Redlands, California, USA.

IFNET ACTION REPORT, 2006, Good practices for substantial human loss reduction from floods. International Flood Network. Available online at: http://www.internationalfloodnetwork.org/index.html.

Joyce, J. R., E. J. Janowiak, P. A. Arkin, and P. Xie, 2004: CMORPH: A method that produces global precipitation estimates from passive microwave and infrared data at high spatial and temporal resolution. J. Hydrometeor., 5, 487–503.

Khan A. K., G. Akhter and Z. Ahmad: 2011: GIS as project manager in geophysical applications software. Journal of geographic information system. 3, 166-172.

Kidd, C., 2001: Satellite rainfall climatology: A review. Int. J. Climatol., 21, 1041–1066.

Kidd, C., and V. Levizzani, 2011: Status of satellite precipitation retrievals. Hydrol. Earth Syst. Sci., 15, 1109–1116.

Kidd, C., P. Bauer, J. Turk, G. J. Huffman, R. Joyce, K. L. Hsu, and D. Braithwaite, 2012: Intercomparison of High-Resolution Precipitation Products over Northwest Europe. J. Hydrometeor., 13, 67–83.

Kollet, S. J., and R. M. Maxwell, 2006: Integrated surface–groundwater flow modeling: A free-surface overland flow boundary condition in a parallel groundwater flow model. Advances in Water Resources, 29, 945-958.

Kummerow, C. D., and L. Giglio, 1994a: A passive microwave technique for estimating rainfall and vertical structure information from space. Part 1: algorithm description. Journal of Applied Meteorology. 33, 3-18.

Kummerow, C. D., and L. Giglio, 1994b: A passive microwave technique for estimating rainfall and vertical structure information from space. Part 2: applications to SSM/I data. Journal of Applied Meteorology. 33, 19-34.

Kummerow, C., Y. Hong, W. S. Olson, S. Yang, R. F. Adler, J. McCollum, R. Ferraro, G. Petty, D. B. Shina, and T. T. Wilheit, 2001: The evolution of the Goddard Profiling algorithm (GPROF) for rainfall estimation from passive microwave sensors. J. Appl. Meteorol. 40(11), 1801-1820.

Lehner, B., K. Verdin, and A. Jarvis, 2006: Hydrosheds technical documentation,USGS. [Available online at http://hydrosheds.cr.usgs.gov/webappcontent/HydroSHEDS_TechDoc_v10.pdf].

Levizzani, V., R. Amorati, and F. Meneguzzo, 2002: A review of satellite-based rainfall estimation methods. European Commission Project MUSIC Report (EVK1-CT-2000-00058)

Lovejoy, S., and G. L. Austin, 1979: The delineation of rain areas from visible and IR satellite data from GATE and mid-latitudes. Atmosphere-Ocean. 17, 77-92.

Lull, H.W., Ecological and silvicultural aspects, Handbook of applied hydrology, ed., Ven Te Chow, 6.1-6.30, McGraw-Hill, New York, 1964.

Ly, S., C. Charles, and A. Degre, 2013: Different methods for spatial interpolation of rainfall data for operational hydrology and hydrological modeling at watershed scale. A review. Biotechnol. Agron. Soc. Environ. 17(2), 392-406.

Masih, I., S. Maskey, S. Uhlenbrook, and V. Smakhtin, 2011: Assessing the impact of areal precipitation input on stream flow simulations using the SWAT model. Journal of American Water Resources Assoc. 47(1), 179-195.

Panday S, and Huyakorn PS. 2004. A fully-coupled spatially distributed model for evaluating surface/subsurface flow. Advances in Water Resources 27: 361–382.

Petty, G., and W. F. Krajewski, 1996: Satellite estimation of precipitation over land. Hydrol. Sci. J., 41, 433–451.

Refsgaard, J. C., and J. Knudsen 1996: Operational Validation and Intercomparison of Different Types of Hydrological Models. Water Resources Research, Volume 32, No. 7, pp. 2189-2202.

Refsgaard, J. C., 1997: Parameterization, calibration and validation of distributed hydrologic models. Journal of Hydrology, 198, 69-97.

Richardson, J.L. and M.J. Vepraskas, 2000: Wetland soils: genesis, hydrology, landscapes and classification. lewis publishers, boca raton, FL. (ISBN : 1566704847).

Ruelland, D., S. Ardoin-Bardin, G. Billen, and E. Servat, 2008: Sensitivity of a lumped and semi-distributed hydrological model to several methods of rainfall interpolation on a large basin in West Africa. Journal of Hydrology. 361(1-2), 96-117.

Sahoo, G. B., C. Ray and E. H. D. Carlo, 2006: Calibration and Validation of a Physically Distributed Hydrological Model, MIKE SHE, to Predict Streamflow at High Frequency in a Flashy Mountainous Hawaii Stream. Journal of Hydrology, 327, 94-109.

Sapiano, M. R. P., and P. Arkin, 2009: An Intercomparison and Validation of High-Resolution Satellite Precipitation Estimates with 3-Hourly Gauge Data. J. Hydrometeor., 10, 149–166.

Scofield, R. A., and R. J. Kuligowski, 2003: Status and outlook of operational satellite precipitation algorithms for extreme precipitation events. Wea. Forecasting, 18, 1037–1051.

Segond, M. L., H. S. Wheater, and C. Onof, 2007: The significance of spatial rainfall representation for flood runoff estimation: a numerical evaluation based on the Lee catchment, UK. Journal of Hydrology, 347(1-2), 116-131.

Shah, S. M. S., P. R. O'Connell, and J. R. M. Hosking, 1996. Modelling the effects of spatial variability in rainfall on catchment response. 2. Experiments with distributed and lumped models. Journal of Hydrology. 175(1-4), 89-111.

Shuttleworth W.J., 1992: Evaporation in Handbook of Hydrology ed. D.R.Maidment, McGraw-Hill, p4.1-4.51.

Singh, C. R., J. R. Thompson, J. R. French, D. G. Kingston, and A. W. Mackay, 2010: Modelling the impact of prescribed global warming on runoff from headwater catchments of Irrawaddy River and their implications for the water level regime of Loktak Lake, northeast India. Hydrol. Eart Syst. Sci., 14, 1745-1765.

Smith, M. B., D. Seo, V. I. Koren, S. M. Reed, Z. Zhang, Q. Duan, F. Moreda, and S. Cong, 2004: The Distributed Model Intercomparison Project (DMIP): Motivation and Experiment Design. J. Hydrology, 298, pp. 4-26.

Sorooshian, S., K. Hsu, X. Gao, H. V. Gupta, B. Imam, and D. Braithwaite, 2000: Evaluation of PERSIANN system satellite-based estimates of tropical rainfall. Bull. Amer. Meteor. Soc., 81, 2035–2046.

Soytekin, A. 2010: Evaluating the use of satellite-based precipitation estimates for discharge estimation in ungauged basins, M.S. Thesis, METU, Civil Eng. Dept., September, Ankara.

Stampoulis, D., and E. N. Anagnostou, 2012: Evaluation of global satellite rainfall products over continental Europe. J. Hydrometeor., 13, 588-603.

Strangeways, I., 2011. Precipitation: Theory, Measurement and Distribution. Cambridge University Press, 290 p.

Su, F., Y. Hong, and D. P. Lettenmaier, 2008: Evaluation of TRMM Multisatellite Precipitation Analysis (TMPA) and Its Utility in Hydrologic Prediction in the La Plata Basin. J. Hydrometeor., 9, 622–640.

Sultana, Z., and P. Coulibaly, 2011: Distributed modelling of future changes in hydrological processes of Spencer Creek watershed. Hydrological Processes, 25, 1254-1270.

TEFER, 2002: Turkey Emergency Flood and Earthquake Recovery (TEFER) - Flood forecasting and model development. Government of Republic Turkey, Ministry of Energy and Natural Resources, General Directorate of State Hydraulics Works and Investigation and Planning Department, Ankara.

Thiemig, V., R. Rojas, M. Zambrano-Bigiarini, A. D. Roo, 2013: Hydrological evaluation of satellite-based rainfall estimates over the Volta and Baro-Akobo Basin, J. Hydrol., 499, 324–338.

Therrien, R., R.G. McLaren, E.A. Sudicky, and S.M. Panday. 2007. HydroGeoSphere: A three-dimensional numerical model describing fully-integrated subsurface and surface fl ow and solute transport: User manual. Groundwater Simul. Group, Univ. of Waterloo, Waterloo, ON, Canada.

Thompson J. R., H. Gavin, and A. Refsgaard, 2009: Modelling the hydrological impacts of climate change on UK lowland wet grassland. Wetlands Ecol Manage. 17, 503-523.

Thompson, J. R., A. J. Green, D. G. Kingston and S. N. Gosling, 2013: Assessment of Uncertainty in River Flow Projections for the Mekong River Using Multiple GCMs and Hydrological Models. Journal of Hydrology, 486, 1-30.

Tian, Y., C. D. Peters-Lidard, B. J. Chaudhury, and M. Garcia, 2007: Multitemporal analysis of TRMM-based satellite precipitation products for land data assimilation applications. J. Hydrometeor., 8, 1165–1183.

Tian, Y., C. D. Peters-Lidard, and J. B. Eylander, 2010: Real-time bias reduction for satellite-based precipitation estimates. Journal of Hydrometeorology, 11, 1275-1285.

Tian Y., G. J. Huffman, R. F. Adler, L. Tiang, M. Sapiano, V. Maggioni, and H. Wu, 2013: Modeling errors in daily precipitation measurements: additive or multiplicative?. Geophysical research letters, 40, 2060-2065.

Tolson, B. A., and C. A. Shoemaker, 2007: Dynamically dimensioned search algorithm for computationally efficient watershed model calibration. Water Resources research. 43, W01413.

Tombul, M., Akyürek, Z., and A. Ü. Sorman, 2004: Determination of soil hydraulic properties using pedotransfer functions in a semi-arid basin, Turkey. *Hydrol. Earth Syst. Sci*, **8**, 1200–1209.

Turan, B. 2002: Obtaining Inundation Maps by GIS and Hydrologic - Hydraulic Model Integration, M.S. Thesis, METU, Civil Eng. Dept., July, Ankara.

Uğuz, M. F., and Sevin, M., 2011: Geologic Map of Kastamonu - F 31 Sheet Report No: 145. *General Directorate of Mineral Research and Exploration (MTA).*

Wagener, T., and H. V. Gupta, 2005: Model identification for hydrological forecasting under uncertainty, Stoch. Environ. Res. Risk Assess., 19(6), 378-387.

Wagener, T., M. Sivapalan, P. Torch and R. Woods, 2007: Catchment classification and hydrologic similarity. Geography Compass 1(4), 901-931.

Wang, N. Y., C. Liu, R. Ferraro, D. Wolff, E. Zipser, and C. Kummerow, 2009: TRMM 2A12 land precipitation product-Status and future plans. J. Meteorol. Soc. Jpn. Ser. II. 87A, 237-253.

Westerberg, I., A. Walther, J. L. Guerrero, Z. Coello, S. Halldin, C. Y. Xu, D. Chen, and L. C. Lundin, 2009: Precipitation data in a mountainous catchment in Honduras: quality assessment and spatiotemporal characteristics. Theor. Appl. Climatol., 101, 381–396.

Wijesekara, G. N., A. Gupta, C. Valeo, J. G. Hasbani, Y. Qiao, P. Delaney and D. J. Marceau, 2012: Assessing the impact of future land-use changes on hydrological processes in the Elbow River watershed in southern Alberta, Canada. Journal of Hydrology, 412-413, 220-232.

Vila, D. A., De Goncalves, L. G. G., Toll, D. L., & Rozante, J. R. (2009). Statistical Evaluation of Combined Daily Gauge Observations and Rainfall Satellite Estimates over Continental South America. Journal of Hydrometeorology, 10(2), 533–543. doi:10.1175/2008JHM1048.1

Vuglinski, V. S., 1972: Methods for the study of laws for the distribution of precipitation in medium-high mountains (illustrated by the Vitim River basin). Distribution of Precipitation in Mountainous Areas, WMO Pub. 326(2), World Meteorological Organization, Geneva, 212-221.

Xie, P., M. Chen, S. Yang, A. Yatagai, T. Hayasaka, Y. Fukushima, and C. Liu, 2007: A Gauge-Based Analysis of Daily Precipitation over East Asia. J. Hydrometeor., 8, 607–626.

Yan, J.J. and K.R. Smith, 1994: Simulation of Integrated Surface Water and Ground Water Systems - Model Formulation. Water Resources Bulletin, v30 (5), p1-12

Yanmaz, M., Usul, N., 1999: "Assessment of Flood Induced Problems of Urbanized Areas in Turkey", Urban Settlements and Natural Disasters 23-31.

Yücel, I., and A. Onen, 2014: Evaluating a mesoscale atmosphere model and a satellite-based algorithm in estimating extreme rainfall events in northwestern Turkey. Nat. Hazards Earth Syst. Sci. 14, 611-624.

Yücel, I., R. J. Kuligowski, and D. J. Gochis, 2011: Evaluating the hydro-estimator satellite rainfall algorithm over a mountainous region. International Journal of Remote Sensing. 32, 22, 7315-7342.

Yilmaz, K. K., T. S. Hogue, K. L. Hsu, S. Sorooshian, H. V. Gupta, and T. Wagener, 2005: Intercomparison of Rain Gauge , Radar , and Satellite-Based Precipitation Estimates with Emphasis on Hydrologic Forecasting. J. Hydrometeor., 6, 497–517.

Yilmaz, K. K., H. V. Gupta, and T. Wagener, 2008: A process-based diagnostic approach to model evaluation: Application to the NWS distributed hydrologic model. Water Resources Research. 44, doi:10.1029/2007WR006716.

Zhao, H., R. T. Zhang and J. Laing, 2012: Application of MIKE SHE/MIKE 11Model to Structural BMPs in s191 Basin, Florida. Journal of environmental Informatics

Zinke, P.J., Forest interception studies in the United States, International Symposium on Forest Hydrology, eds., W.E. Sopper & H.W. Hull, 137-161, Pergamon Press, Oxford, 1967.